Modeling Rotating Cavitation Instabilities in Rocket Engine Turbopumps

an MSc thesis in Aerospace Engineering

Adam Gabor Vermes

Delft University of Technology

TU Delft Delft University of Technology

Challenge the future

Modeling Rotating Cavitation Instabilities in Rocket Engine Turbopumps

an MSc thesis in Aerospace Engineering

by

Adam Gabor Vermes

in partial fulfilment of the requirements for the degree of

Master of Science
in Aerospace Engineering

at the Delft University of Technology

Supervisor: Dr. Ir. Claudio Lettieri

Committee: Dr. Ir. Arvind Gangoli Rao (chair)
Dr. Ir. Claudio Lettieri
Dr. Ir. Angelo Cervone

Thesis registration number: 157#17#MT#FPP

Abstract

With heavy duty propulsion systems under development for upcoming Mars missions, such as the *Space Launch System* and the *Interplanetary Spaceship*, the stability of high-performance liquid-propellant rocket engines is of renewed interest. High-power-density rocket turbopumps forward pressurized fuel to the combustor at high rates. Turbopumps operate at extreme design conditions, where propellants may cavitate, and cause instabilities. Of particular interest is Rotating Cavitation, which is characterized by a non-axisymmetric cavity distribution that rotates super-synchronously with the pump impeller. Rotating Cavitation can cause severe structural vibration and fatigue fracture, which have, and may again lead to loss of the mission.

Rotating Cavitation is traditionally suppressed through casing treatment. To comply with the high market pressure dictated by the private space sector, it needs to be suppressed through impeller design, before expensive production and testing initiates. Despite significant research, no general impeller design guidelines exist to avoid the onset of Rotating Cavitation. State-of-art predictive methods are either prohibitively time-consuming, or yield limited prognostic capacity. Predicting Rotating Cavitation requires time-accurate 3D numerical assessment, and an explicit understanding of the physics that drive its mechanism. It has recently been hypothesized, that Rotating Cavitation is caused by strong coupling of cavity dynamics between blade passages, which is governed by blockage. This hypothesis facilitates the blockage-based assessment of Rotating Cavitation, which is presented in this thesis.

The goal of this project is to devise a new numerical capability to predict Rotating Cavitation during the design phase of turbopumps. This is achieved by reducing the computational cost of calculations. Mesh dimensions and the complexity of governing equations can be reduced by accounting for viscous- and cavity-blockage with models derived from first principles. Reduced-order blockage models are incorporated into inviscid, one-phase numerical simulations. The method is validated through comparison with high-fidelity simulations and experimental data from literature. The total-to-total pressure characteristics of a 2D cascade is captured within 0.26% error, and the flow displacement due to cavity formation on a hydrofoil within 5% error. Rotating Cavitation is captured in a 2D cascade, at an order of magnitude less computational cost than what high fidelity methods require. The thesis proves the hypothesis, that Rotating Cavitation is a purely blockage-driven phenomenon.

Keywords: turbopump, flow instability, rotating cavitation, blockage model, body force method

Acknowledgements

I would first like to thank first my daily supervisor, Dr. Claudio Lettieri for the opportunity of being involved in *Rocket Science*. His continuous support and guidance have greatly contributed to the quality of the report and improved my thesis experience. I hope to have condensed some of his contagious enthusiasm towards challenging the state-of-art.

I am grateful for the understanding, thoughts and comments of Ms. Hanna Eva Bayer, who helped with the timely delivery of the report, and who never fails to make me feel capable of anything. I would also like to acknowledge my entire family for providing the upmost stability over the course of my studies. I would like to recognize my parents for providing emotional, financial and medical support, my wonderfully talented brothers Brúnó and Zénó for keeping me to the ground at all times, and my caring Grandma, whose sense of humor is a beacon of light in the darkest places.

Finally, I would like to thank my housemates Samy and Tom and Joeri for sharing the historic town of Delft with me, and my research fellows Alberto, Dominic, Laurence, Paul, Piotr, Pranav and Reynard for providing all the healthy distractions from work.

Table of Contents

List of Figures

List of Tables

Nomenclature

Symbols

A	control surface [m^2]
B	Greitzer B parameter[-]
D	diameter [m]
F	empirical factor to account for interphase mass transfer rate per unit volume [-]
f	frequency [s^{-1}]
$\mathbf{f}$	external force field [kg m^{-2} s^{-2}]
g	gravitational acceleration [m s^{-1}]
h	impeller blade spacing [degree]
h_T	total specific enthalpy [m^2 s^{-2}]
k	turbulent kinetic energy [m^2 s^{-2}]
K	cavitation compliance [-]
L	characteristic length [m]
l	tip vortex cavity length [degree], distance measured along stream path [m]
M	mass gain factor [-]
m	number of unstable cavitation cells [-]
$\dot{m}$	interphase mass transfer rate per unit volume [-]
$\mathbf{n}$	normal vector [-]
N	specific speed [-]
p	pressure [kg m^{-1} s^{-2}]
Q	volumetric mass flow [m^3 s^{-1}]
R	radius [m]
Re	Reynolds number [-]
$\mathbf{s}$	arbitrary source term (scalar or vector)
S	suction specific speed [-]
$\mathbf{S_C}$	continuity source [kg m^{-3} s^{-1}]
$\mathbf{S_E}$	energy source [kg m^{-1} s^{-3}]
$\mathbf{S_M}$	momentum source [kg m^{-2} s^{-2}]
St	Strouhal number [-]
T	Time [s]
$\mathbf{u}$	velocity vector [m s^{-1}]
U	velocity in the X direction [m s^{-1}], system characteristic velocity [m s^{-1}]
V	velocity in the Y or θ direction [m s^{-1}], control volume [m^2]
W	velocity in the Z direction [m s^{-1}],
Z_n	blade count [-]

Greek Symbols

α	absolute frame flow angle [degree]
β	relative frame flow angle [degree]
γ	surface tension [kg s^{-2}]
ε	turbulent dissipation factor [m^2 s^{-2}]
λ	second coefficient of dynamic viscosity [kg m^{-1} s^{-1}]
μ	dynamic viscosity [kg m^{-1} s^{-1}]
∇	Nabla (del) operator
ν	kinematic viscosity [m^2 s^{-1}]
ρ	density [kg*m^{-3}]
σ	cavitation number [-]
$\boldsymbol{\sigma}$	fluid stress tensor [kg m^{-1} s^{-2}]
$\boldsymbol{\tau}$	viscous stress tensor [kg m^{-1} s^{-2}]
Φ	flow coefficient [-]
$\boldsymbol{\phi}$	arbitrary intensive flow property
φ	volume fraction [% 100^{-1}]
ψ	head [m], or pressure-rise coefficient with 'p' subscript [-]
ω	internal thermal energy [m^^{2} s^{-2}]
Ω	rotational velocity [rad^{-1}]

Subscripts

1	parameter denoting upstream condition
2	parameter denoting downstream condition
A	subscript for 'available' NPSH (Net Positive Suction Head): $NPSH_A$
bn	direction binormal to wall surface, defined by: **t** x **n**
cond	parameter describing condensation process (vapor→liquid)
cr	critical parameter value
e	parameter taken at boundary layer edge
i	parameter denoting inlet condition
l	parameter describing quality of liquid flow phase
n	direction normal to streamlines, or wall surface
nuc	parameter describing quality of nucleation site
o	parameter denoting outlet condition
P	pressure (used to differentiate pressure-rise coefficient from head rise)
p	direction parallel to streamlines
R	subscript for 'required' NPSH (Net Positive Suction Head): $NPSH_R$
s	steady-state parameter, or static pressure coefficient
t	direction tangential to wall surface, parallel to projection of free-stream
tip	parameter describing quality valid at the impeller tip

v	parameter describing quality of vapor flow phase
vap	parameter describing vaporization process (liquid→vapor)
x	parameter in the axial direction
∞	parameter denoting far field condition, infinitely far from observation

Acronyms

ABC	Alternate Blade Cavitation
CFD	Computational Fluid Dynamics
CS	Cavitation Surge
DNS	Direct Numerical Simulation
IGV	Inlet Guide Vane
LES	Large Eddy Simulation
LHS	Left Hand Side
LOX	Liquid Oxygen
LPFP	Low-Pressure Fuel Pump
LPLOP	Low-Pressure Liquid Oxigen Pump
MIT	Massachusetts Institute of Technology
NPSH	Net Positive Suction Head
N-S	Navier-Stokes
PVR	Propagation Velocity Ratio
RANS	Reynolds Averaged Navier-Stokes
RC	Rotating Cavitation
RHS	Right Hand Side
R-P	Rayleigh-Plesset
SSME	Space Shuttle Main Engine
URANS	Unsteady Reynolds-Averaged Navier-Stokes

1

Introduction

1.1. Background

Recent advancements of the private space sector (such as the Falcon 9 landings) drive innovation in liquid-propellant rocket engine design, and push the envelope of rocket performance and stability. Consequently, market pressure to deliver reliable launch vehicles at reduced engine development cost grows rapidly, which leads to increased industrial interest in reduced order design tools.

Modern liquid propellant space launch systems require high-performance turbopumps to provide pressurized propellants to the combustor at high flow-rates. System requirements of low mass and volume translate into high power-density pumps. High rotational speeds of the impeller yield operating conditions where pressure drops below vapor pressure and the fuel vaporizes. In order to mitigate cavitation in highly loaded pumps, liquid propellant systems typically feature an inducer positioned ahead of the turbopump, whose function is to sufficiently increase the pump inlet pressure to avoid cavitation. Inducers are in turn exposed to considerable cavitation even at design condition. Cavitating inducers are susceptible to dynamic flow instability because the mass (and therefore energy) storing capacity of compressible vapor bubbles amplify disturbances when mass and pressure fluctuations are in phase. Flow instability in turbopumps might cause structural vibrations, failure of launch vehicle elements, and potentially the loss of the mission.

Unforeseen violent structural vibrations of NASA launch systems in the 60ies (Titan II, Saturn V, Apollo 13, Thor/Agena, Delta, Gemini and the Titan-5) necessitated research on cavitation-induced instabilities [1]. In fact, 59% of all failed rocket launches are due to propulsion system failure, mostly caused by instabilities in the turbopump or combustor. One of such instabilities is *Rotating Cavitation* (RC), characterized by an uneven distribution of blade cavities at the inducer inlet that travels faster than the pump impeller. Alternating loads exerted by non-axisymmetric blade loading are transferred to the pump casing, which causes high order vibration and eventually the fatigue fracture of launch vehicle elements. RC was observed in the *liquid oxygen* (LOX) and liquid hydrogen inducers of the Japanese LE-7 rocket engine [2], the LOX turbopump of the NASA FASTRAC (or MC-1) rocket engine [3], the *Low-Pressure Oxidizer Pump* (LPOP) of the *Space Shuttle Main Engine* (SSME) [4], and during the development of the Ariane 5 Vulcain engine [5]. In each case, cavitation instabilities were discovered late in the design process. In the case of the LE-7 engine, unanticipated RC led to the loss of the H-II flight 8 mission and its payload [6].

1.2. Limitations of Current Practice

Casing treatment methods and simple modifications of the inducer blades have long been employed to enhance liquid rocket system stability in hindsight, typically at the significant expense of performance. To find an optimal trade-off between performance and stability, inclusion of RC assessment in the inducer design process is key. RC is an unsteady, non-axisymmetric, three-dimensional and inherently non-linear cavitation instability, which requires numerical assessment. Unfortunately, high-fidelity simulations with acceptable RC prognostic capacity are prohibitively expensive. On the other hand, computationally affordable reduced order methods yield limited capacity to assess RC, due to the insufficient modeling of key fluid behavior. Despite significant research, no affordable RC assessment capacity has yet been devised, and so RC is typically identified after expensive manufacturing and testing has begun.

The capability of predicting the onset of RC from first principles would increase propulsion system reliability and decrease engine development costs, which is of great benefit for turbopump manufacturers.

1.3. Scope

This research project proposes and validates models derived from first principles to improve RC predictive capacity of current numerical solvers and ease further research in the area. These models focus on capturing blockage (due to viscous effects and cavitation in individual blade passages), which is hypothesized to drive RC. Blockage models are validated against 2D canonical geometries. Challenges of scaling the viscous models to 3D are also explored.

The literature review presented in Chapter 2 provides answers for the following two questions:

- What is the impact of RC on rocket engine turbopumps?
  - What is the theoretical framework of cavitation and the stability of turbopumps?
  - What non-dimensional parameters characterize the behavior of cavitating turbopumps?
  - How is RC different from other fluid instabilities observed in rocket turbopump inducers?
  - What physical mechanism leads to RC, and which parameters influence its behavior?

- Which RC mitigation practices may drive the design of future RC-free turbopump inducers?
  - What are the best practices to mitigate RC and to what extent are they successful?
  - Which successful RC mitigation practices deteriorate pump performance the least?
  - How do RC mitigation practices comply with low weight, size, and complexity requirements?

The thesis provides answers for the following research question:

- Could RC be captured at reduced computational cost?
  - What methods have successfully been employed to analyze cavitating fluid instabilities?
  - What are the limitations of state-of-art reduced order methods?
  - How could a reduced order model be combined with high-fidelity analysis to assess RC for a fraction of the computational cost of full-scale CFD simulations?
  - By what margin are the cavity displacement and viscous pressure characteristics of canonical 2D test cases captured by the proposed models? (Validation)
  - Does the proposed method capture RC in a canonical 2D cascade?
  - Is it possible to scale the model to 3D, and what are the expected challenges?

1.4. Major Contributions of Thesis

- Combined viscous models capture the total-to-total pressure characteristics of 2D cascades with 0.23% error in steady simulations. Neither the viscous *Kinetic Energy Dissipation Model,* nor the *Inviscid Stream Displacement Model* yield acceptable results on their own.
- The *Cavity Blockage Model* captures cavity displacement thickness and collapse point around 2D hydrofoils with 10% and 5% errors respectively, in steady 1-phase simulations.
- The *Cavity Blockage Model* captures RC in transient 2D cascade simulations. The rate of cavity growth and decay needs to be modeled to assess RC *Propagation Velocity Ratio* (PVR).

- Capturing RC with blockage models implemented in single-phase inviscid numerical simulations proves the hypothesis, that RC is a purely blockage-driven fluid instability.
- The devised method reduces the computational overhead associated with non-axisymmetric three-dimensional unsteady 2-phase simulations by an order of magnitude.

1.5. Thesis Outline

The literature review is presented in Chapter 2. Section 2.1 provides an overview of cavitation (2.1.1), and introduces the physical mechanism and key parameters (2.1.2) associated with cavitating turbopumps. Section 2.1.3 explores pump stability, arriving at the conclusion that the energy-storing capacity required for dynamic instability onset might be provided by cavity bubbles. Unlike stall-like instabilities, this can very well happen at design condition, which brings the discussion to cavitation effects on turbopump stability in Section 2.1.4. Section 2.2 presents the state-of-art description of RC and aims to unravel the physical mechanism that drives its onset and propagation. Section 2.2.1 introduces the dynamic transfer functions of cavitating turbopumps and connects the onset of RC to tip vortex cavity growth. Finally, Section 2.2.2 discusses best practices to suppress RC, which can drive the design of future RC-free inducers.

The gap in knowledge is identified in Chapter 3. Limitations of state-of-art RC analysis methods are presented in Section 3.1. The discussion includes simplified linear stability analysis techniques, body force methods, and Computational Fluid Dynamics (CFD) approaches of varying complexity: RANS, URANS, LES and DNS. The need for a new numerical capacity with blockage models derived from first principles is highlighted in Section 3.2. Finally, research objectives are listed in Section 3.3, and the technical roadmap for model validation is given in Section 3.4.

Chapter 4 provides the mathematical framework for the thesis. Section 4.1 describes the numerical solver's governing equations, to facilitate discussion on model assumptions. Derivations of the *Viscous Blockage Models* are given separately for the *Kinetic Energy Dissipation Model* and the *Inviscid Stream Displacement Model* in Sections 4.2.1 and 4.2.2. Finally, the *Cavity Blockage Model* (an extension to the *Inviscid Stream Displacement Model*) is derived in Section 4.3.

Validation results are discussed in Chapter 5. The *Viscous Blockage Models* are validated on the NASA rotor 67 2D mid-span cascade in Section 5.1. The steady response of the *Cavity Blockage Model* is validated on the NACA 0015 hydrofoil 2D profile in Section 5.2. Transient model capacity to capture RC in the 2D flat-plate cascade of Iga et al. is assessed in Section 5.3. Challenges with scaling viscous models to 3D are documented in Section 5.4, using an experimental inducer geometry of the Pratt & Whitney Aircraft Company (Rockwell inducer).

2

Literature Review

High performance turbopumps in liquid propellant rocket engines operate under heavily cavitating conditions, which makes them susceptible to develop unstable behavior. Cavitation instabilities, such as *Rotating Cavitation* (RC), may appear under design conditions, where unsteady behavior is unexpected for the most part. RC is characterized by a non-axisymmetric distribution of blade cavities at the inducer inlet, which rotates faster than the pump impeller. Uneven blade loading due to travelling cavities is transferred to the pump casing in the form of oscillating stresses, which can cause fatigue fracture and disintegration of launch vehicle elements. To prevent severe degradation of performance, structural vibration and loss of the mission, suppression of RC is imperative to modern rocket design.

Traditional industrial practices trade off performance for stability by modifying the inducer and casing after expensive manufacturing and testing has taken place. To find the optimal trade-off and comply with the growing market pressure set by the private space sector, RC needs to be suppressed in the design phase. There are no generally accepted design guidelines as to how RC should be suppressed. Thus, a new RC assessment capacity needs to be devised and incorporated into the automated design optimization of rocket inducers.

This literature review explores the physics and key parameters that drive RC, and evaluates limitations of state-of-art RC predictive methods. The review also identifies best practices to guide the design of future RC-free inducers.

2.1. Review of Cavitation-Induced Fluid Instabilities

2.1.1. The Cavitation Phenomenon in General

Cavitation in fluid systems occurs when fluid pressure drops below the vapor pressure, and vapor bubbles start to form. Unexplained blade erosion in high-speed marine propellers necessitated pioneering research on bubbly flow. Reynolds linked erosion damage to entrained air bubbles in the wake in 1873 [7], which is now known as ventilation. Parsons [8] was first to recognize the possibility of pressure-driven fluid vaporization in 1906, which initiated a century of scientific experimentation with cavitation. In 1917, Rayleigh [9] derived the first mathematical model of bubble dynamics, which described the growth of spherical cavity bubbles (R_B) as function of the external fluid pressure (p_∞). The Rayleigh equation (Eq. 1) can be derived from mass balance and the Navier-Stokes equations of momentum conservation across the bubble boundary [10]. The model assumes constant density liquid (ρ_l), and constant internal bubble pressure ($p(R_B)$), which is equal to the saturated vapor pressure (p_v).

$$R_B \frac{d^2 R_B}{dt^2} + \frac{3}{2}\left(\frac{dR_B}{dt}\right)^2 = \frac{p(R_B) - p_\infty}{\rho_l} \qquad \text{Eq. 1}$$

Since Rayleigh, the formation and collapse of cavity bubbles have become a field of intensive research, driven by the need to investigate the head drop (or cavitation breakdown) of pumps, which is a sudden deterioration of performance due to extensive cavitation. In 1953, Guinard et al. [11] observed large cavity volumes at stable operating conditions of pumps, and – for the first time – cavitation in vortex filaments, which is known today as tip vortex cavitation. Acosta confirmed both findings experimentally in 1958 [12], and recognized that proper description of cavitating turbopumps was not possible without radical simplification of the problem at the time. His follow-up work on cascades and simple geometry hydrofoils characterize basic cavitation research of the 60ies and 70ies. Acosta et al. reviewed the pioneering work on cavitating turbopumps in 1959 [13], describing the steps cavities typically progress through: from inception to partial- and sheet cavitation and finally to cavitation breakdown.

Modern cavitation research aims to identify the pump design parameters and fluid properties that influence the cavitating performance of pumps, and delay the occurrence of head drop. In 1962, Stripling et al. [14] explored the possibility of predicting head drop in cascades by relating cavity length to fluid flow angle (α) and free-stream pressure (p_∞). To control experiments, the authors used a conventional dimensionless parameter called *cavitation number* (σ or Kc), which indicates the likelihood of cavitation inception in fluids, and makes its first appearance in the experimental works of Knapp et al. [15] as early as 1948. In 1969, Ruggeri et al. [16] presented a method of generalizing experimental results to assess performance characteristics of turbopumps with widely diverse physical properties.

In 1977, Plesset [17] reviewed contemporary state-of-art knowledge on cavity growth, collapse, and non-spherical bubble dynamics. Referring to his previous work from 1949 [18], Plesset provided an extension to Eq. 1, which accounted for effects of viscosity (ν_l) and surface tension (γ) on cavity growth. The resulting equation, widely referred to as the *Rayleigh-Plesset equation* (R-P), is given in eq. 3. The R-P is derived from equilibrium of the normal forces acting on the bubble lamina (eq. 2), due to pressure (LHS:1 & RHS:1), surface tension (RHS:2) and viscosity (RHS:3). The equilibrium of normal forces is expressed in eq. 2, which yields eq. 3 when substituted into Eq. 1. The R-P is an ordinary differential equation, which governs bubble dynamics in most modern two-phase Computational Fluid Dynamics (CFD) solvers. Vapor pressure inside the bubble (p_v) and pressure of the surrounding liquid (p_∞) may now be functions of time.

$$p(R_B) = p_v - \frac{2\gamma}{R_B} - \frac{4\nu_l}{\rho_l R_B}\frac{dR_B}{dt} \qquad \text{Eq. 2}$$

$$R_B\frac{d^2R_B}{dt^2} + \frac{3}{2}\left(\frac{dR_B}{dt}\right)^2 + \frac{2\gamma}{\rho_l R_B} + \frac{4\nu_l}{R_B}\frac{dR_B}{dt} = \frac{p_v(t) - p_\infty(t)}{\rho_l} \qquad \text{Eq. 3}$$

In 1995, Brennen [19] reviewed the literature on basic cavitation research, and discussed bubble-dynamics on a micro level, with glimpses into large-scale cavity structures. Brennen stated that flow contaminants (small particles and microbubbles) are far more relevant for the formation of cavity bubbles than surface nuclei (surface roughness and wall contaminants). With this, he essentially differentiated cavitation from boiling, from the perspective of nucleation sites. Brennen also listed the necessary flow parameters to be controlled or measured in systematic experiments on small-scale cavitation inception: fluid temperature, stream turbulence, surface roughness, cavitation- and Reynolds numbers, and the amount, and nature of free-stream nuclei.

Further review work of Brennen [20] concerned the fundamentals of multiphase flows focusing on cavitation inception, erosion, noise and luminescence. He explained that doughnut-like shape-distortion of spherical bubbles against a solid surface led to micro jet formation upon bubble collapse. Peak temperatures and pressures up to 6700 K and 848 bar sustained for a fraction of a microsecond chip away material from the blade, mechanically eroding its surface. Blade erosion and propeller noise are the traditional drivers for cavitation research, due to reliability and stealth issues of marine applications. In contrast, cavitation in turbopumps is a domain of distinguished research interest because of the vibration and structural damage caused by unstable pump behavior.

2.1.2. Performance of Cavitating Turbopumps

The performance and unsteady behavior of cavitating turbopumps can be fully characterized with a handful of non-dimensional parameters that ensure general validity of results between similar cases. Pump performance is assessed through the *head coefficient* (ψ), a function of flow rate. Flow rate is controlled by the *flow coefficient* (ϕ) under non-cavitating conditions. The *specific speed* (N) is the basic preliminary design parameter of turbopumps. Arguably the most critical parameter to the onset of RC is the *cavitation number* (σ), which is also expressed as the *suction specific speed* (S), or in traditional dimensional form as the *Net Positive Suction Head* ($NPSH$). The *Reynolds* (Re) and *Strouhal* (St) *numbers* ensure dynamic similarity between cases, by preserving the ratios of inertial and viscous forces, and time-scales of steady and oscillatory phenomena within the fluid. An extensive overview of the derivation of non-dimensional parameters is given by Dixon [21].

The *pressure rise coefficient* (ψ) is the most important performance parameter of turbopumps. Given in Eq. 4, ψ is a ratio of pressure- and inertial forces within the fluid, and is not different from the Euler number (Eu), or the reciprocal Ruark number (Ru), applied between the inlet ($_1$) and outlet ($_2$) of the pump. The coefficient's name originates from the traditional measure of liquid pressure (p), the hydraulic head ($H = p/\rho g$).

$$\psi = 2\,Eu = 2\frac{1}{Ru} = \frac{p_2 - p_1}{\frac{1}{2}\rho U^2} \qquad \text{Eq. 4}$$

The *flow coefficient* (ϕ) is a measure of the non-dimensional flow rate, and hydrodynamic forces generated on the blades critically depend on it [22]. The *flow coefficient* (Eq. 5) corresponds to the ratio of characteristic axial (c_x) and circumferential velocities (V_{tip}). Alternatively, ϕ is given by the volumetric fluid flow (Q) normalized by the upstream cross-section (A) and blade tip velocity (V_{tip}).

$$\phi = \frac{c_x}{V_{tip}} = \frac{Q}{AV_{tip}} \qquad \text{Eq. 5}$$

The *specific speed* (N) correlates volumetric flow rate (Q), head rise (ψ) and shaft speed (Ω) in one basic, size-independent performance parameter. The *specific speed* (Eq. 6) characterizes the desired performance of a pump in its initial design phase, when pump dimensions are yet undetermined.

$$N = \frac{\Omega Q^{\frac{1}{2}}}{(H)^{\frac{3}{4}}} \qquad \text{Eq. 6}$$

The *Net Positive Suction Head* ($NPSH$) is a historical parameter that measures how close the fluid is to cavitation inception on the scale of the *hydraulic head* (H). The $NPSH$ (Eq. 7) is expressed using total pressure (p_T) at the pump inlet ($_i$), and so it takes velocity into account, which is not relevant to cavitation [23]. $NPSH_A$ indicates the available ($_A$) pressure margin above cavitation onset. Conversely, $NPSH_R$ gives the *hydraulic head* required ($_R$) at any point, to keep fluid from cavitating.

$$NPSH_A = \left(\frac{p_i}{\rho g} + \frac{{U_i}^2}{\rho g}\right) - \frac{p_v}{\rho g} \quad \text{Eq. 7}$$

A non-dimensional form of net positive suction head is the *net suction specific speed* (S) of pumps given in Eq. 8. This parameter indicates the critical condition at which head-rise degradation due to extensive cavitation reaches a critical percentage [23].

$$S = \frac{\Omega Q^{\frac{1}{2}}}{(NPSH)^{\frac{3}{4}}} \quad \text{Eq. 8}$$

The *cavitation number* (σ) characterizes the susceptibility of the fluid to undergo cavitation. The *cavitation number* indicates the difference between the static pressure (p) and saturated vapor pressure (p_v), also called tension, over the dynamic pressure. The dynamic pressure is expressed in terms of the fluid velocity (U) and density (ρ) in Eq. 9. Originally, *Thoma's cavitation number* (σ_{TH}) denoted the $NPSH$ over the *head* ($p/\rho g$) of the pump. Since $NPSH$ is defined using total pressure (p_T), σ_{TH} varies greatly with impeller size [13], and therefore σ is an arguably better alternative.

$$\sigma = \frac{p - p_v}{\frac{1}{2}\rho U^2} \quad \text{Eq. 9}$$

The *Reynolds number* (Re) indicates the relative importance of viscous effects against inertia effects, where low Re flows are dominated by viscous forces. Derived from the scaling of the momentum equation, the *Reynolds number* (Eq. 10) is an important determinant of dynamic similitude between different machines, fluids and experimental setups.

$$Re = \frac{\rho U L}{\mu} = \frac{U L}{\nu} \quad \text{Eq. 10}$$

The *Strouhal number* (St), or reduced frequency, relates two time-scales: the time required for flow particles to pass through the machine (L/U), and the characteristic time-scale of an instability ($1/f$). The parameter given in Eq. 11 indicates whether a flow-instability problem requires quasi-steady, or transient modeling. Low St values correspond to either high speed fluid or low frequency oscillation, which translates into quasi-steady, low Re flow. Conversely, high values indicate highly unsteady behavior typical for high Re turbulent flow.

$$St = \frac{fL}{U} \quad \text{Eq. 11}$$

Finally, the *Greitzer B parameter* [24] indicates a fluid system's susceptibility to develop surge, based on the wheel speed at mean diameter (V_{mean}), and the total effective length of the system (L_C).

$$B = \frac{fV_{mean}}{2L_C} \quad \text{Eq. 12}$$

2.1.3. Stability of Turbopumps

Fluid pumping systems consist of a pump and some sort of system resistance, against which the fluid is moved. The resistance can be adjusted by adding a throttle to the system. The steady-state operating point is where the pressure rise on the pump equals the pressure drop due to system resistance, and there is equal flow through the pump and throttle [24]. Betchov et al. [25] defined system stability as "the quality of being immune to small disturbances". In 1981 Greitzer concluded [24], that a turbopump is considered stable if it returns to its stable operating condition after any disturbance in pressure rise or flow stream. This is shown in Figure 1, which plots pressure rise across the pump (curve) against pressure drop on the throttle (lines). Steady state operating points (A, B, C & D) correspond to different throttle settings. As a rule-of-thumb, the throttle characteristics need to be steeper than the pump pressure-rise curve, in order to maintain static stability (point A to B). Otherwise, the flow rate disturbances across the pump get amplified on the throttle, and the system diverges from its steady operating point (point B to E). Even if statically stable, fluid systems can experience dynamically unstable behavior when operating on positively sloped parts of the pump pressure rise characteristics. This is shown on the RHS of Figure 1, at point D, and its causes are explored next.

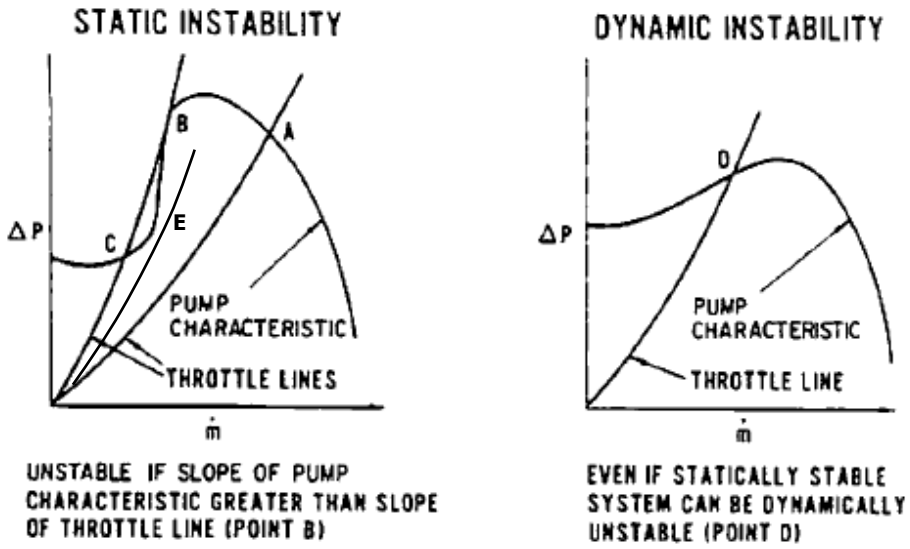

Figure 1 – Static and dynamic instability criteria in fluid pumping systems [24]

The physical mechanism responsible for system-level dynamic instability is illustrated in Figure 2. In simple words: if the pump (the only energy source to an adiabatic system) supplies excess mechanical energy to an otherwise dissipative system, severe pressure and mass-flow oscillations will appear with growing amplitudes. This is called surge. The realization of surplus oscillatory energy is possible when the components of mechanical energy disturbance (oscillating mass flow ($\dot{m}$) and pressure difference (Δp)) are in phase, and their product sums positive over time. The components of surplus mechanical energy are illustrated on the RHS of Figure 2, with a traditional dissipative (dynamically stable) system given on the LHS for contrast.

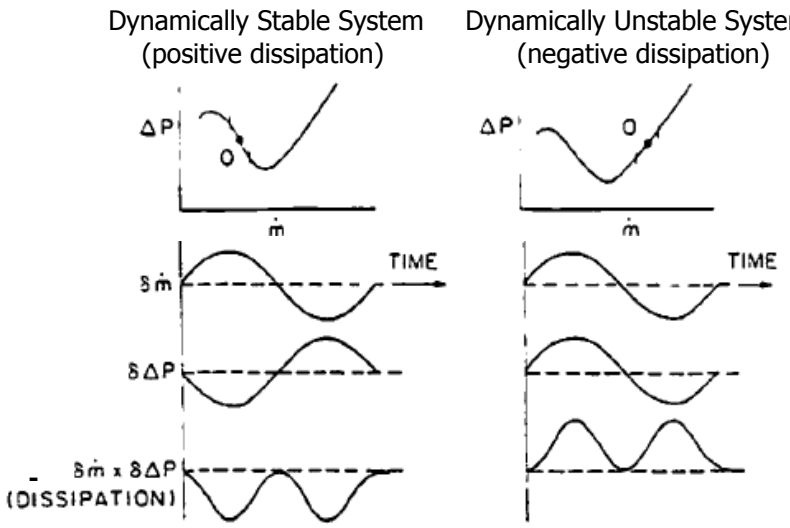

Figure 2 – Negative damping of in-phase ṁ and Δp oscillations cause dynamic instability [24]

Surge-type instabilities can be modeled as results of negative damping in a classic mass-spring-damper system representation. The spring coefficient can be derived from the compliance of large plenums of fluid and compressible gases, which is found in a fuel tank for instance. Compliance can also be added to the system through the energy-storing capacity of compressible vapor bubbles. When considerable amount of gas-phase medium is present in the pump, traditional stability considerations no longer grant immunity from unstable behavior. Cavitation-induced instabilities may appear even at dynamically stable operating points and cause considerable damage to launch vehicles.

2.1.4. Cavitation Effects on Turbopump Stability

The effect of cavitation on the stability of fluid pumping systems became the subject of distinguished scientific attention when NASA connected extreme structural vibration (POGO) to cavitating turbopumps in 1970 [1]. Space launch systems might develop violent fluctuations of pressure and mass-flow across the entire hydraulic system, which originate from the mass (and inherently energy) storing capacity of cavity bubbles dispersed in a fluid. This capacity is characterized by the *Cavitation Compliance* (K), a parameter that relates changes in cavity volume (V_C) to the cavitation number (σ) [26]:

$$K = \frac{\partial V_C}{\partial \sigma} \qquad \text{Eq. 13}$$

Wade et al. first observed the parameter K in the 60ies, during the experimental assessment of partial cavity transition into full-scale cavities over hydrofoils [27] and cascades [28]. Brennen et al. worked out a linearized theory to account for *Cavitation Compliance* in cascades in 1970 [29] and 1973 [30], which provided the basic reference for research on cavitation instabilities over the next three decades. In 1976, Brennen et al. discovered that a neglected term in the 1973 [30] formulation of the transfer matrix of cavitating pumps was responsible for large discrepancies between

calculated and measured compliances. Based on that term, the authors derived the *Mass Flow Gain Factor* (M) in 1976 [31], which is a dynamic transfer function that tracks cavity volume variation (Vc) due to flow rate fluctuations (ϕ), described in Eq. 14. *Cavitation Compliance* (K) and *Mass Flow Gain Factor* (M) together characterize the dynamic behavior of cavity bubbles.

$$\mathrm{M} = \frac{\partial \mathrm{V_C}}{\partial \phi} \qquad \text{Eq. 14}$$

In 1971, NASA [32] reviewed the possibility of mitigating unintended oscillatory pressure loading (which was observed during the normal operation of many space launch systems), by adding an axial inlet portion to cavitating centrifugal turbopumps, called an inducer. A typical four-bladed inducer is displayed in Figure 3, which was designed at MIT based on the Space-Shuttle Main Engine (SSME) Low-Pressure Liquid Oxygen Pump (LPLOP). Sutton et al. [33] explained the function of inducers as to increase the fluid pressure ahead of the pump sufficiently enough (typically by 2-10% of the total required head rise along the pump) to avoid substantial cavitation on the pump impeller. Benefits of inducers are twofold. First, inducers mitigate flow-induced vibration and cavitation erosion on the pump impeller, by which they support more compact pump designs. Second, by increasing the Available Net Positive Suction Head ($\mathrm{NPSH_A}$) of rocket fuel pumps, inducers allow for less pressurized fuel tanks, which translates into considerable weight reduction. In return, inducers experience moderate cavitation even in the vicinity of their design point, which can develop into severe instabilities.

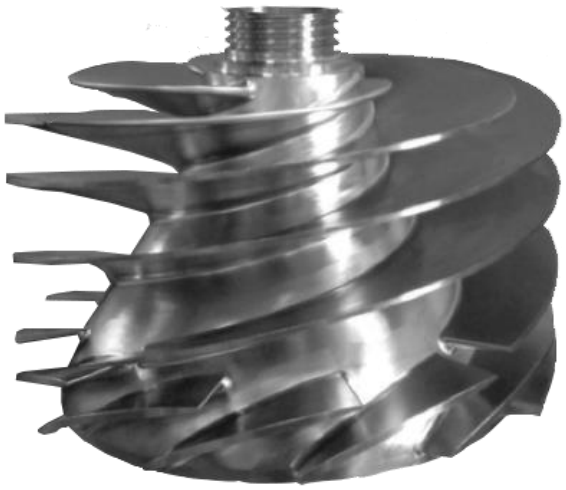

Figure 3 – Geometry of the 4-bladed MIT test inducer is based on the SSME LPOP inducer [34]

Several cavitation-induced fluid instability modes are shown in Figure 4, mapped on the static pressure coefficient (ψ_S) - cavitation number (σ) plane of the LE-7 inducer, which Tsujimoto et al. [34] generated experimentally in 1997. When describing cavitation instabilities, one must notice their similarities to stall-induced instabilities. For instance, an axisymmetric cavitation instability, which causes large-scale oscillations of pressure and flow rate, was named *Cavitation Surge* (CS) [35], highlighting its analogy to traditional *Axisymmetric Stall* (AS), or compressor surge [24]. This instability mode was found to be responsible for POGO, and the domain on which it was observed is indicated in blue in Figure 4.

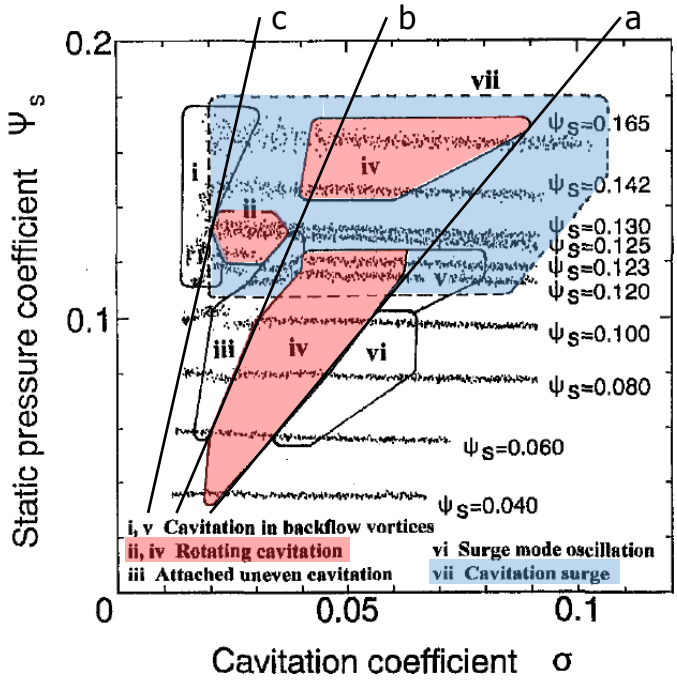

Figure 4 – Cavitation map (LE7 inducer) indicates relation between RC inception & $\sigma/2\alpha$ [34]

Another cavitation induced fluid instability is RC, which is indicated in red in Figure 4. Unlike CS, RC is a local phenomenon, which is characterized by a non-axisymmetric distribution of blade cavities that rotates super-synchronously around the inducer inlet [36]. This instability occurs under moderately cavitating conditions just above head drop, often at the pump design point. RC is in some degree analogous to *Rotating Stall* (RS), which is a non-axisymmetric flow driven by the viscous blockage of stalled passages, and rotates at 45-60% of the compressor speed. Both RS and RC are triggered by flow rate disturbance due to increased blockage in a neighboring blade passage. Blockage is caused by flow separation due to increasing inlet flow angle in case of RS, and by growing cavities due to positive *Mass Flow Gain Factor* (M) [37] in case of RC. The flow physics that govern the mechanism of RC is further discussed in Section 2.2.

2.2. Rotating Cavitation

2.2.1. Onset and Propagation Mechanism of Rotating Cavitation

Rotating Cavitation (RC) was first identified experimentally in 1977, when Kamijo et al. [36] described it as a fluid instability mode of unequal cavity volumes travelling around the impeller inlet, slightly above head breakdown. Following Kamijo, most of the scientific research concerning RC has been conducted by the Japanese research community. Basic RC research is heavily intertwined with the development of a reduced order RC assessment capacity, which is summarized next.

At first, Tsujimoto et al. [37] assessed RC using an actuator disk approach, based on [38]. At that time, both *Cavitation Compliance* (K, Eq. 13) and *Mass Flow Gain Factor* (M, Eq. 14) were well-established dynamic transfer functions, which accounted for cavity growth due to change in σ and ϕ. Tsujimoto et al. demonstrated the mathematical link between instability modes and their propagation frequencies based on K and M, which the authors estimated from Brennen et al. [39]. Although *Propagation Velocity Ratio* (PVR) of forward-rotating RC modes matched experimental results of Kamijo et al. [36] and those of the LE-7 LOX pump inducer [2], comprehensive assessment of model applicability was not possible at the time, because of the absence of further test data. Moreover, backward rotating modes of RC have never been found in experiments. Watanabe et al. [40] provided the parameter values for K and M for a wide range of cascade geometries in 1998.

In 1996, Otsuka et al. [41] examined K and M in inducers, using a closed cavity mathematical model, which showed perfect analogy with the results of Wade, obtained from conformal mapping in 1967 [42]. The approach of Otsuka et al. supported unequal cavity lengths on different blades, and eliminated the previous assumption of low frequency cavity oscillations by Furuya [43]. Otsuka et al. found numerical proof of the various cavity instability modes being characterized by the combined effects of cavitation number (σ) and flow angle (α), which the authors expressed in the parameter $\sigma/2\alpha$. Constant parameter values of $\sigma/2\alpha$ can be visualized with straight lines crossing the origin of the graph in Figure 4. In Figure 4, RC develops at a wide range of operating conditions between lines 'a' and 'b', and again between 'b' and 'c', indicating clear connection between critical $\sigma/2\alpha$ parameter values and the onset of RC. Watanabe et al. [44] further clarified the nature of this connection, by analyzing RC in cascades without the empirical parameters M and K. Watanabe et al. observed a strong relation between the parameter $\sigma/2\alpha$ and the length of tip vortex cavities, which are slender volumes of vaporized fluid formed in the low-pressure vortex cores of the tip leakage flow. In 1998, Horiguchi et al. [45] analytically confirmed, that tip vortex cavity length (and so $\sigma/2\alpha$) is a powerful indicator of the breakdown of *Alternate Blade Cavitation* (ABC) into RC. The theoretical framework of assessing ABC, RC and CS by relaxing the cavity closure constraint in the model of Otsuka is discussed next.

In 2000, Horiguchi et al. [46] documented the basic methodology for the linear stability analysis of cavitating flat plate cascades based on the work of Otsuka et al., aiming for analytically reproducing every mode of cavitation instability observed in inducers. The authors achieved this by relaxing the cavity-closure and phase-difference constraints on individual blades, and analyzing the cavity closure constraint residuals to identify different cavity modes. Horiguchi et al. detected cavitation patterns with steady components of two types: *equal length cavities* (ELC) and ABC. Imposing unsteadiness on the identified steady cavity types, three main modes of cavitation instability emerged: CS, RC, and unsteady ABC. In agreement with experiments, ABC developed first with decreasing values of $\sigma/2\alpha$. Unstable cavitation phenomena started when the average length of tip vortex cavities (l_s) covered approximately 65% of the blade pitch (h), at which point ABC appeared. This is clearly visible in Figure 5, which plots the normalized steady cavity length of both ELC and ABC against various $\sigma/2\alpha$ parameter values. Following the characteristics of ELC towards decreasing $\sigma/2\alpha$, two different additional stable cavity lengths appear at a critical $\sigma/2\alpha$, which indicates the onset of ABC.

To model various modes of RC on a wide scale of *Strouhal numbers* (St), Horiguchi et al. relaxed the phase difference constraint. The authors showed analytically that PVR is proportional to the $\sigma/2\alpha$ at which RC develops, and inversely proportional to inter-blade phase difference ($2\pi m/ZN$), where ZN is the blade count, and m indicates the number of unstable cavity cells around the annulus.

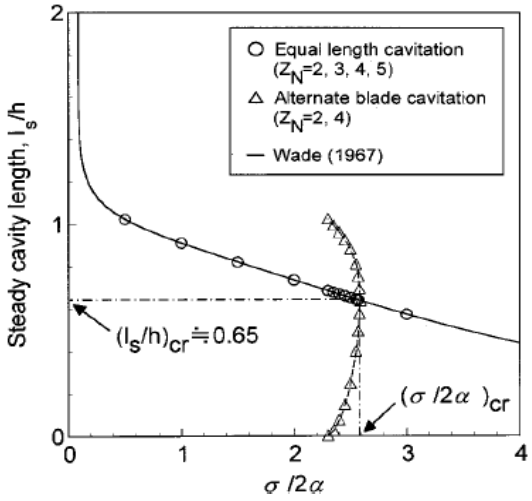

Figure 5 – *Alternate Blade Cavitation* develops from equal length blade cavities at l/h=0.65 [46]

In the new millennium emphasis is put on formulating the appropriate answer to exactly what physical mechanism drives RC and its onset, for which proper assessment of the flow field is needed. In 2007, Hosangadi et al. [47] successfully employed an unsteady three-dimensional numerical method to simulate RC within an inducer, and described an interaction pattern between detached blade cavities. Following the work of Hosangadi et al., Tani et al. established the *Travelling Cavity Interference Theory* in 2012, which is visualized in Figure 6 [48]. The figure displays the growth and decay of individual blade cavities in a three bladed inducer, over one period of RC. On each blade, the large cavity volume starts to decay when the cavity on the previous blade reaches maximum extent, which results in a forward-rotating pattern of unequal blade cavities. The strong coupling of cavity dynamics is governed by interaction between neighboring cavities, which is discussed next.

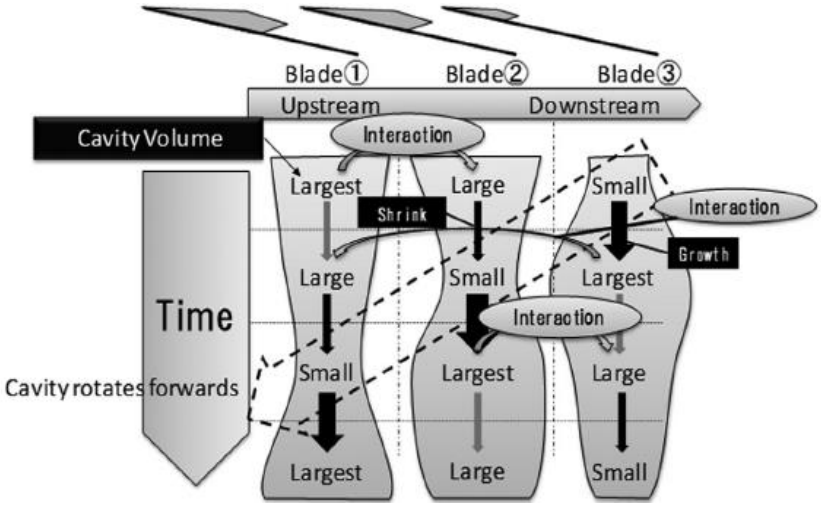

Figure 6 – RC is governed by blade cavity interaction & travels forward at pump inlet [48]

In 1999, Watanabe et al. [44] observed, that RC is first triggered by interaction between the tip vortex cavity of one blade and the local flow at the leading edge of the next blade. Kimura et al. [49] explained this interaction by comparing the tip vortex cavity collapse point to a fluid volume sink of negative velocity divergence, which reduces flow angle at the next leading edge, and triggers unstable behavior. In 2009, Kang et al. [50] conducted an exhaustive numerical study on the velocity disturbance flow of collapsing tip vortex cavities in 3D inducers. The trigger mechanism is depicted schematically in the top of Figure 8, in the blade-to-blade view of a four-bladed inducer cascade.

In 2016, Lettieri et al. [51] explained the breakdown mechanism of ABC into RC in a four-bladed inducer designed at MIT, based on the SSME LPLOP inducer (Figure 3). Experimental results of the normalized cavitating head (just above head drop) against σ are shown in Figure 7, indicating regions of ABC, RC and CS. The authors found that RC developed again at low σ, where it has already been triggered by tip vortex cavities, and has reverted back into ABC. It was hypothesized, that the interaction between neighboring blade passages that leads to RC may be triggered by unequal blockage. Blockage (a combination of viscous losses and cavitation displacement) alters the flow angle along the full length of the next leading edge in 3D inducers, which is shown schematically in the bottom of Figure 8.

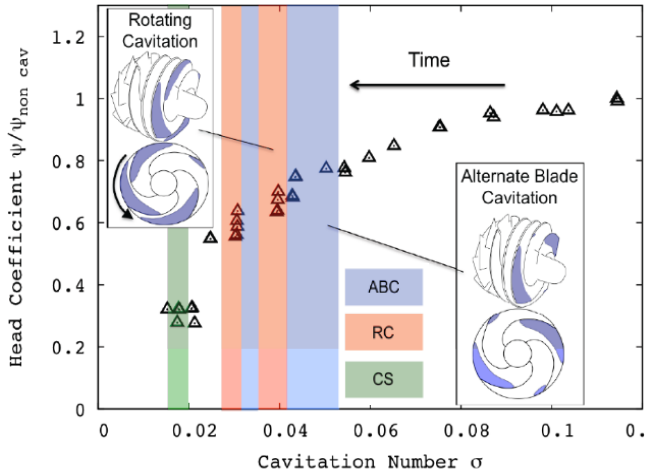

Figure 7 – The second appearance of RC in the MIT inducer is governed by blockage [51]

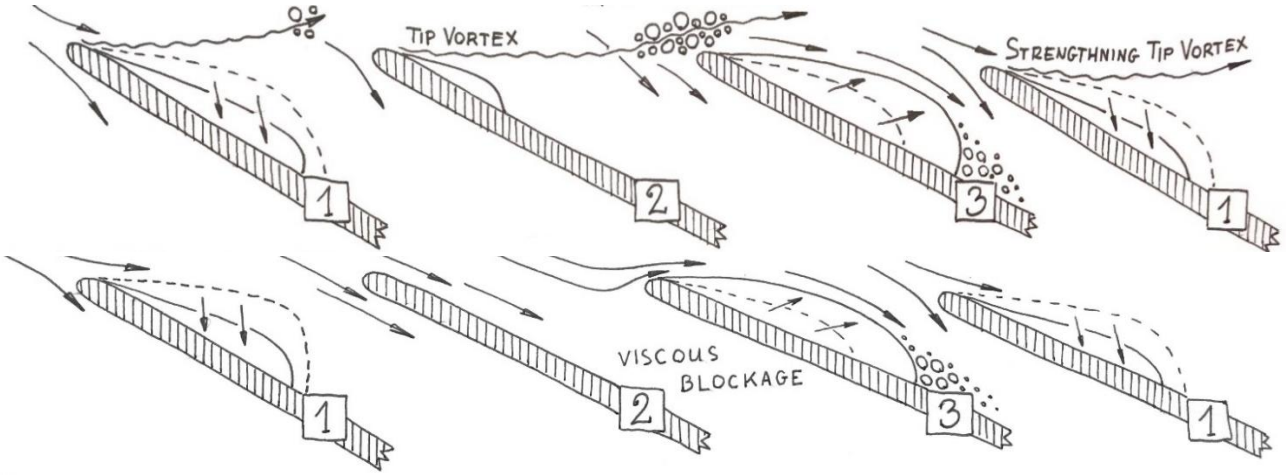

Figure 8 – RC propagation mechanisms driven by tip vortices (top) and blockage (bottom) [51]

In conclusion, there is a scientific consensus that RC is first triggered by tip vortex cavity interference. Mitigating this interference has been the primary focus of RC suppression research. Most RC suppression techniques take advantage of backflow, which is a reverse flow fueled by a pressure-driven leakage between the pump casing and blade tips, as indicated in grey in Figure 9. Although essentially a loss, intense backflow blows the tip vortex cavities upstream into the inducer inlet duct and away from the leading edges, by which it delays RC. This was demonstrated experimentally in the works of Hashimoto et al. in 1996 [52] and Torre et al. in 2011 [53], and it is the key for industrial RC suppression techniques. Instabilities in the shear layer between the main flow and backflow might grow into vortices [54], which Yokota et al. [55] confirmed experimentally in 2004. These backflow vortices are indicated in black curls in Figure 9. Backflow vortices extend far upstream of the impeller, occupying up to 75% of the inlet cross section and distorting velocity profiles of the main flow, by which they deteriorate pump performance. The number of vortex filaments decreases at reduced ϕ, as they are pushed towards the duct axis by the growing backflow volume [56]. Moreover at low σ, cavities appear in the low pressure cores of backflow vortices (regions 'i' and 'v' in Figure 4), which might coexist with RC [56]. The intermittent cavity interference caused by backflow vortices introduces disturbance into the tip leakage vortices, by which it plays a minor role in delaying RC [57]. In 2007, Yamanishi et al. [58] demonstrated all of the above characteristics of backflow vortices in high fidelity LES simulations. Finally, Yamamoto et al. [59] reviewed the scientific work on backflow in 2009. Backflow tends to destabilize the hydraulic system at flow-rate oscillation frequencies lower than 10% of the inducer rotational frequency [60].

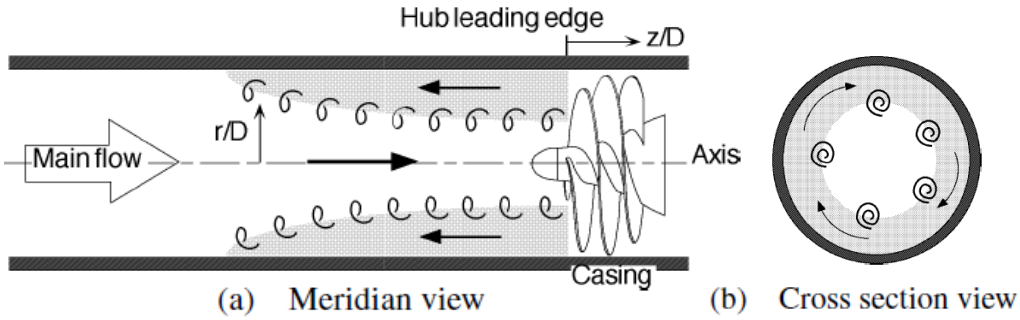

Figure 9 – Vortices appear at the rolled-up shear layer between backflow and main flow [55]

2.2.2. Rotating Cavitation Suppression Techniques

Many design techniques have been used to suppress the onset of cavitation instabilities in rocket engine turbopumps, which can be categorized based on their approach to the problem. One is a collective of trial-and-error based approaches, which aim to avoid further catastrophes by means of casing treatments, the other involves basic research and complete redesign of the inducer geometry. The latter is considered superior for its preventive nature and relative simplicity of the resulting design, but it requires immense computational capacities and a thorough understanding of RC. In 2009, Kang et al. [57] investigated the effect of some basic inducer design modifications to avoid RC: blade sweepback to promote backflow, blade metal angle drop to weaken tip vortices, and outlet angle increase to extend tip vortices into the blade channel. A review by Lettieri et al. [51] pronounced sweepback, tip gap, leading edge blade metal angle and rotational velocity to be critical design parameters to RC suppression. Of those, decreasing the rotational velocity is a trivial solution to the problem (reduced flow angle translates into increased σ), and will not be further discussed. To find a comprehensive list of design parameters and suggest a direction to drive the design of RC-free inducers, a review of historical and cutting-edge RC suppression techniques follows. Visual reference for all discussed design considerations is given in Figure 10.

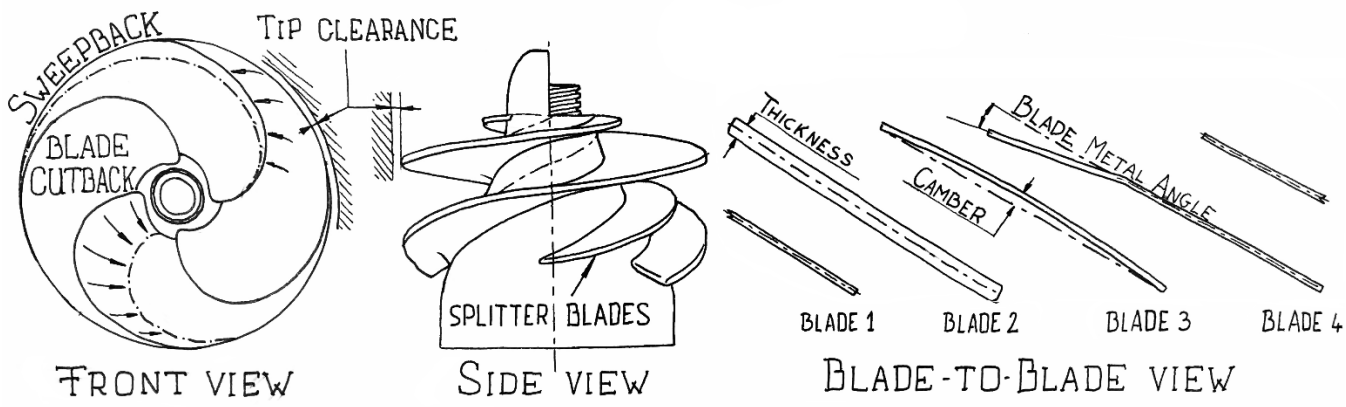

Figure 10 – Various design modifications of rocket inducers might suppress RC

- **TIP CLEARANCE AND SWEEPBACK:** Backflow delays the breakdown of stable cavity patterns into unstable ones, by driving the tip vortex cavities away from the leading edge of neighboring blades [61]. Despite its stabilizing effect on cavitation instabilities [53], backflow is essentially a loss mechanism, and should be minimized from a performance point-of-view. Brennen [23] noticed, that the performance of non-cavitating turbopumps deteriorates rapidly when the tip clearance exceeds 2% of the inducer inlet diameter. To predict pump performance as function of tip clearance, Torre et al. proposed a semi-empirical model in 2009 [62], and later examined the effect of 2.7% and 6.8% tip clearances on cavitation instabilities [53]. Torre used the DAPAMITO3 test inducer, which was designed using a reduced order analytical model by Cervone et al. [63] and d'Agostino et al. [64], and was further tested by Torre et al. [65] [66] [53] and Pasini et al. [67]. Torre et al. [53] concluded, that the wider the tip clearance gets, the stronger the backflow becomes, and the more the cavitation instabilities (including RC) are suppressed – at the inevitable cost of pump

performance. Tip vortex strength is inversely related to tip clearance, ceteris paribus [68]. In summary, increasing tip clearance at the pump inlet reduces the initial blade loading, weakens cavitation in the tip vortices, and diverts the vortex filaments upstream. However, maintaining large tip gap along the rest of the blade chord significantly deteriorates the performance of pumps.

A possible solution to minimizing tip leakage loss further downstream of the pump inlet emerges in the form of a highly swept leading edge, which melds into the traditionally small downstream tip clearance. In 2001, Acosta et al. [69] found that both forward- and back-swept leading edge designs mitigated RC, however, forward-swept designs made no further appearance in literature, due to their poor hydro-elastic and vibrational properties. In 2007, Kang et al. [70] examined inducers with moderate (90°) and high back-sweeps (210°). Kang et al. registered a 10% increase in backflow axial extent for a 210° swept design as compared to a standard 90° case. Backflow grew by an additional 50% when the blade metal angle was also increased by 2°, showing strong effect of blade cutback when combined with high initial blade loading. Unfortunately, highly swept leading edge designs yield 16% deterioration in pump performance, which is four times more than due to blade metal angle modifications.

- **LEADING EDGE BLADE METAL ANGLE:** Kang et al. [70] also examined the effect of reduced blade metal angle at the pump inlet. Results show that blade angle drop mitigates tip vortex cavitation (and so RC) by modifying the blade loading distribution locally at the leading edge. The inherent loss in pressure rise across the pump is counteracted by the contraction of backflow, causing only minor changes to pump performance. Backflow length is reduced by up to 50%. In conclusion, blade metal angle drop has the potential to reduce tip vortex strength and backflow concurrently, uphold pump performance and mitigate RC.

- **CAMBER, THICKNESS AND LEADING EDGE PROFILE:** In 2006, Horiguchi et al. [71] assessed the contribution of suction side pressure gradients to RC. They did so by examining effects of blade camber and thickness in the theoretical setup of Osaka University's singularity model for cavitation instability analysis in cascades. The study registered negligible decrease in steady cavity length due to changes in blade camber and thickness. Regarding the leading edge profile, there is scientific consent on the 1973 findings of Furuya et al. [72]: a pointy leading edge design filed on the suction side is superior to all other designs and is also the easiest to manufacture.

- **ALTERNATE CUTBACK:** One intuitive solution to suppressing RC (and any other cavitation instability that develops from tip vortex cavity interaction) is to increase the blade pitch. When the impeller blade-count and diameter are fixed, increasing blade pitch at the inlet is only possible by cutting back the leading edge of every second blade. This is only possible on inducers with even number of blades. Horiguchi et al. established the theoretical basis for alternate cutback analysis in 2000 [22] [73], and found two types of ABC: one with shorter cavities on shorter blades and longer cavities on the longer blades, one the other way around.

Yoshida et al. have experimentally validated the model in 2001 [74] finding only the first type of the predicted ABC. Although the technique successfully mitigates the breakdown of ABC into RC, it causes considerable drop in pump performance. Moreover, asymmetric blade loads and inherent shaft vibrations might appear due to uneven cavity volumes on cutback blades.

- **SPLITTER BLADES:** Carrying the design of alternate cutback even further, splitter blades (reduced chord-length blades installed downstream between main blades) might suppress RC, by allowing for lower blade-count on the inducer. Splitter blades are widespread used in centrifugal pumps to increase performance and suppress cavitation instabilities [75] [76], but only limited amount of valid research has been conducted on axial inducers. Splitter blades are expected to suppress cavitation instabilities by increasing blade pitch at the leading edge, while providing sufficient guidance in the channels. Performance degradation is expected.

Alternatively to impeller design modifications, the upstream flow field can be influenced via casing treatments. While casing treatment solutions introduce weight and varying levels of complexity, they provide convenient symptomatic treatment without having to modify the impeller design. Casing treatments suppress RC by either changing the flow angle at the tip so that the tip vortex cavity weakens, or redirecting the tip vortex cavity to avoid its interaction with the proceeding blade.

- **J-GROOVES:** A circumferential pattern of axially oriented chases carved into the casing at the inducer inlet plane is shown in Figure 12 (left). Shimiya et al. [77] found that by axially redirecting the tip leakage flow, its kinetic energy is better focused to extend the tip vortex cavity upstream. It is important to note, that short J-groove designs (L/D=0.265) introduced severe CS to the system. When the axial extent of grooves was increased to L/D=0.398, no RC was observed, and CS occurred only at low σ. J-grooves increase flow resistance, but also support a decrease in tip gap, by which their toll on pump performance is minimal.

- **LEADING EDGE CASING POCKETS:** A structural pocket carved into the casing just upstream of the inducer inlet extends the tip vortex cavities radially outwards, so that their interaction with the next blade decreases. This is shown in the bottom right image of Figure 12. Although it is a handy solution to the problem, the casing pocket introduces weight and considerable resistance to the inlet flow, for little gain in RC suppression.

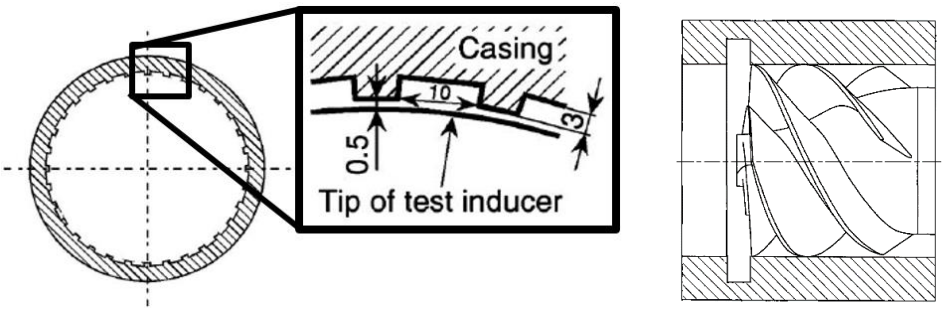

Figure 11 – J-grooves (left) and casing pockets (right) redirect tip vortex cavities [77]

- **JET INJECTION:** It is possible to weaken the tip vortices and mitigate vortex cavitation by either reducing the flow angle, or increasing the fluid pressure at the blade tip. Jet injection achieves both, by introducing pre-whirl in the impeller rotational direction, in the vicinity of the shroud, as shown in Figure 12 (left). Tests show that injecting approximately 10% of the main flow just upstream of the backflow domain suppresses RC. Despite its success to mitigate RC, the weight and complexity of the injectors are prohibitive to rocket turbopump applications [78].

- **INLET GUIDE VANES** Fixed angle IGVs have similar effect to jet injection. Better flow control is possible through an active device (variable angle IGV, Figure 12, right), which are widespread utilized and tested to control pressure rise, efficiency and cavitating performance in centrifugal machines [79]. IGVs introduce weight, complexity, and risk of failure to the system, which makes them unsuitable for rocket turbopump applications.

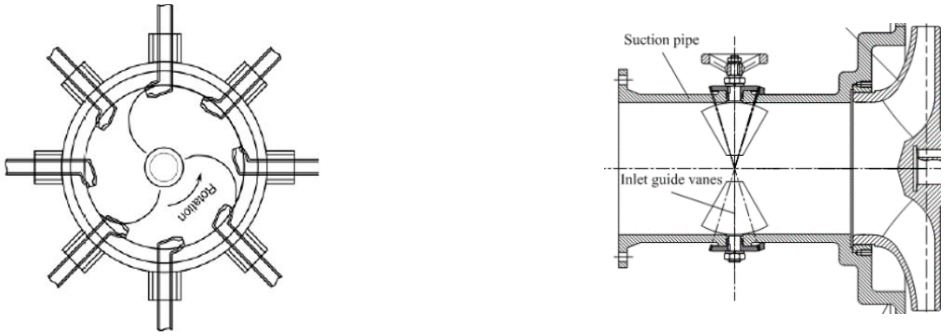

Figure 12 – Jet injection (left) and IGVs (right) reduce flow angle at blade tip [78] [79]

In summary, high leading edge sweep and reduced blade metal angle characterize the most successful impeller designs to suppress RC in inducers. These two parameters may drive the design of future RC-free inducer geometries. The present thesis focuses on devising a tool to help assess RC in the inducer design process, which is discussed next.

3

Modeling of Cavitation Instabilities

Rotating Cavitation (RC) is a dangerous cavitation-induced instability in liquid propellant turbopumps, which can occur at pump design condition and therefore must be suppressed. RC is traditionally discovered during the experimental phase of the pump development, and is suppressed through casing treatment. The modification of the casing usually adds weight and complexity to the system, and deteriorates pump performance. Alternatively, the inducer geometry can be altered to mitigate RC, albeit no generally accepted design guidelines have been established as to how this should be done. To find the optimal RC-free inducer design, numerical assessment of RC in the early development phase of turbopumps is key.

Modeling RC leads to a complex 2-phase instability problem, which requires a time accurate 3D assessment of the entire flow field. This chapter reviews current RC assessment capabilities, identifies the gap in knowledge and defines the research objectives.

The evolution of the state-of-art of RC has been guided by the development of linear stability analysis methods, whose limitations are addressed first. Next, the RC predictive capabilities of two-phase high fidelity numerical solvers are assessed, which are generally limited by computational cost. It is possible to reduce the computational overhead by mapping the force field exerted by the blades directly onto the flow field, using body forces. However, a thorough assessment on the limitations of one-phase body force methods concludes, that the blades need to be included in order to accurately model the local pressure field, which is indicative of cavitation blockage. The inclusion of blades in a body-force simulation brings the discussion to the viscous body force methods, and their extension to two-phase fluids, which characterizes the method devised in the present thesis.

3.1. Flow-Analysis Methods to Assess Cavitation Instabilities

RC is an unsteady, non-linear, non-axisymmetric, viscous, 2-phase phenomenon, which requires high-fidelity numerical assessment. In general, the accurate modeling of each of the properties above reduces the level of empiricism of the simulation, at the expense of computational cost (demand for time, memory and CPU). For single-phase flow assessment techniques, model empiricism is plotted against the demanded computational resources in Figure 13 (adapted from Xu [80]). The two-phase extension adds complexity to each method, but their depicted relations stay valid. On the two ends of the scale are high-fidelity *Computational Fluid Dynamics* (CFD) methods, which provide reliable but time-consuming results, and reduced order models, which prioritize evaluation time over accuracy. Between the two are methods, where features of the impeller or the fluid are either neglected, or approximated with empirical models. The following sections illustrate the strengths and limitations of each approach.

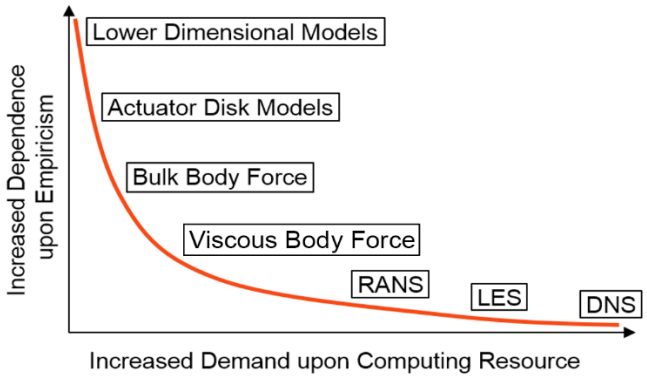

Figure 13 – Overhead of RC assessment methods grows as level of empiricism decreases [80]

3.1.1. Linear Dynamic Analysis Methods

Linearized methods provide a convenient framework for addressing cavitation instabilities in hydraulic systems, based on dynamic transfer functions. The dynamic response of cavity volumes (V_C) to changes in *cavitation number* (σ) and *flow rate* (ϕ) are described in the *Cavitation Compliance* (K, Eq. 13) and *Mass Flow Gain Factor* (M, Eq. 14). Expressing the transfer functions of system components in matrix format has the potential of "clarifying the nature of dynamic performance of cavitating pumps" [24], although it is not particularly suited for detecting local (not system-level) instabilities such as RC. Linearized methods constitute the pioneering work on RC and they have been thoroughly discussed in Section 2.2.1. The present section focuses on the limitations of the linear dynamic analysis of RC.

Linearized methods are limited to two-dimensional, inviscid, irrotational flows with low amplitude oscillations, because of their linearized potential flow assumption. Watanabe et al. [44] significantly reduced the level of empiricism of previous linear models by coupling the singularity method with a closed cavity model, by which unsteady cavitating pump characteristics were assessed without K or M. Watanabe accounted for cavitation with sources distributed along the oscillating cavity length, and represented blades and wakes with bound and free vortices respectively. Although the method

successfully captured RC in a cascade, the range of σ at which it appeared was much larger than in experiments. Horiguchi et al. [46] corrected the discrepancy, and presented a reduced order analysis model aiming to account for all modes of cavitation instabilities, including RC. Although the authors found *Cavitation Surge* (CS), *Alternate Blade Cavitation* (ABC) and RC, no critical comparison with experiments has been conducted to validate the theoretical approach. In 2013 Brennen [81] explained that the unavailability of tests and the lack of a solid theoretical background on the dynamic characteristics of turbopumps eventually limited the method's applicability. Hori et al. emphasized the need for a comprehensive study on the dynamic response of cavitating turbopumps to global oscillations [82]. In summary, linearized analysis methods are capable of detecting RC, but cannot indicate local changes of σ and ϕ, providing limited insight to the mechanism of RC inception.

3.1.2. Computational Fluid Dynamics (CFD)

Numerical Methods provide solutions to flow problems by solving continuity, momentum and energy equations over a discretized flow field. In general, *Numerical Methods* are identified by their approach to solving the *Navier-Stokes* (N-S) equations of momentum conservation. *Direct Numerical Simulations* (DNS) evaluate the N-S equations without compromises to accuracy, resolving the whole range of spatial and temporal scales of turbulence. DNS yield results whose accuracy is only limited by the discretization quality. Small-scale turbulence modeling demands immense computational capacities that exceed the memory and processor speed of most state-of-art computers, and cannot conform to the time limit of design evaluations (<1 hour). *Large Eddy Simulations* (LES) reduce the computational cost of DNS by resolving only the large-scale motions, while accounting for the effect of small-scale turbulence through a subgrid-scale model [83] [84]. The *Reynolds Averaged Navier-Stokes* (RANS) equations provide time-averaged approximate solutions to the N-S problem, further reducing the computational cost. RANS simulations are less accurate than LES or DNS, but they represent an acceptable compromise between cost and performance.

RANS decomposes the N-S into mean and fluctuating components, and approximates the effect of small-scale fluctuations on the mean flow field. During this decomposition, the non-linear term of the fluctuating turbulent velocities can be interpreted as a stress-like contribution to the momentum balance. This term is called the *Reynolds-stress*, and it needs additional modeling. A set of additional transport equations are required to close the governing equations. Depending on the turbulent properties modeled, the *turbulence model* is called k-ε, k-ω, or SST. The k-ε and k-ω models both adopt two differential equations. These equations describe the common turbulent kinetic energy (k), and either the turbulent dissipation (ε, Jones at al. [85]), or the specific rate of dissipation of turbulent kinetic energy (k) into internal thermal energy (ω, Wilcox [86]). Most commonly used is the Shear Stress Transport (SST) turbulence model, which reduces the sensitivity of the k-ε model to the free-stream turbulence intensity, while keeping its accuracy near the wall. Appropriate grid point assignment is critical to capture viscous effect in the boundary layer, which translates into mesh refinements near the walls, and consequently increases computational overhead. The inviscid and incompressible form of the N-S equation is referred to as the Euler equation, which is a quasilinear homogenous representation of the Cauchy equations.

3.1.3. Two-Phase Computational Fluid Dynamics

Numerical methods can be extended to model cavitation, and so capture RC. Liuzzi [87] gave a comprehensive review on cavitation models, which can be characterized into *one-phase*, *two-phase* and *multi-phase* methods. The most simplistic (single-phase) method resolves the liquid phase without mass transfer, assuming that it circumvents the impenetrable cavity domain, which is attached to the blade surface. The cavity boundary can be modeled as a wall, whose extent is either accounted for via simplified analysis, or semi-empirically via previous simulations, which Liuzzi called a "cavity interface tracking method".

Alternatively, when interphase mass transfer is modeled, the flow might be assumed two-phase or multi-phase. Under the two-phase assumption, liquid and vapor phases are treated as a single interpenetrating continuum with no slip between the phases, and a common velocity field. Single-phase vapor transport equations were derived by Kubota et al. in 1992 [88], Schnerr et al. in 2001 [89], and Zwart et al. in 2004 [90], among others. CFX uses the Zwart-Gerber-Belamri model, which is given separately for vaporization ($_{l\to v}$) and condensation ($_{v\to l}$) in Eq. 15 and Eq. 16. These equations are derived from the simplified *Rayleigh-Plesset* (R-P) equation (Eq. 3), by neglecting the second order terms and the surface tension force (γ), and translating change in bubble radius ($\partial R_B/\partial t$) into mass gain ($\dot{m}$) of the vapor phase. The equation requires empirical parameters for nucleation-site radius (R_{nuc}=1[μm]) and volume fraction (r_{nuc}=5e-4), and two empirical factors to account for the different rates of condensation (F_{cond}=0.01) and vaporization (F_{vap}=50). The volume fraction of the vapor phase (φ_v) is tracked by a separate equation.

$$\dot{m}_{l\to v} = F_{vap}\frac{3r_{nuc}(1-\varphi_v)\rho_v}{R_{nuc}}\sqrt{\frac{2}{3}\frac{|p_v(t)-p_\infty(t)|}{\rho_l}}sgn\big(p_v(t)-p_\infty(t)\big) \quad if\ p_\infty(t)<0 \qquad \text{Eq. 15}$$

$$\dot{m}_{v\to l} = F_{cond}\frac{3\varphi_v\rho_v}{R_B}\sqrt{\frac{2}{3}\frac{|p_v(t)-p_\infty(t)|}{\rho_l}}sgn\big(p_v(t)-p_\infty(t)\big) \quad if\ p_\infty(t)\geq 0 \qquad \text{Eq. 16}$$

Finally, multi-phase cavitation models, such as the *Full Cavitation Model* by Singhal et al. [91], simulate N-phase flows and account for the effect of non-condensable gases. Multi-phase modeling is possible in Ansys Fluent, but is not required to capture RC, because its effect on cavity thickness (which is the most RC critical property of cavities) is negligible.

One example of cavitation modeling in CFD is the work of Ji et al. [92], who compared hybrid RANS-LES results on the Delft Twist-11 hydrofoil to experimental results presented by Foeth [93]. LES can capture the cavity shedding dynamics and cavitation-vortex interaction in agreement with experiments, but it is prohibitively expensive to turbopump applications. Furthermore, the different time and length scales of turbulent eddies and the RC instability supports the RANS approximation of the flow field. *Unsteady RANS* (URANS) simulations by Hosangadi et al. [94] [95] [96] captured RC in the SSME LPFP turbopump [95] at discrete points, where RC was expected. The approach is not feasible during design, where a causal link between inducer geometry and the onset of RC must be established through RC assessment at several design points.

3.1.4. Body Force Models

The computational overhead of URANS can be reduced by eliminating the blades, and accounting for their effects (flow turning and viscous losses) through body forces. Peters verified the validity of body force modeling of a compressor fan stage in 2014 [97]. Peters extracted discrete blade forces from single-passage steady RANS calculations, from which he created an equivalent force field in the fan domain to simulate the effect of blades on the flow. The extraction of blade forces from steady-state simulations is illustrated in Figure 14. Peters linked the force- and flow fields through the blade passage model, which comprises component models for parallel and normal forces. The model allows the local flow field to respond to force perturbations in unsteady simulations by prescribing body forces based on the local flow coefficients.

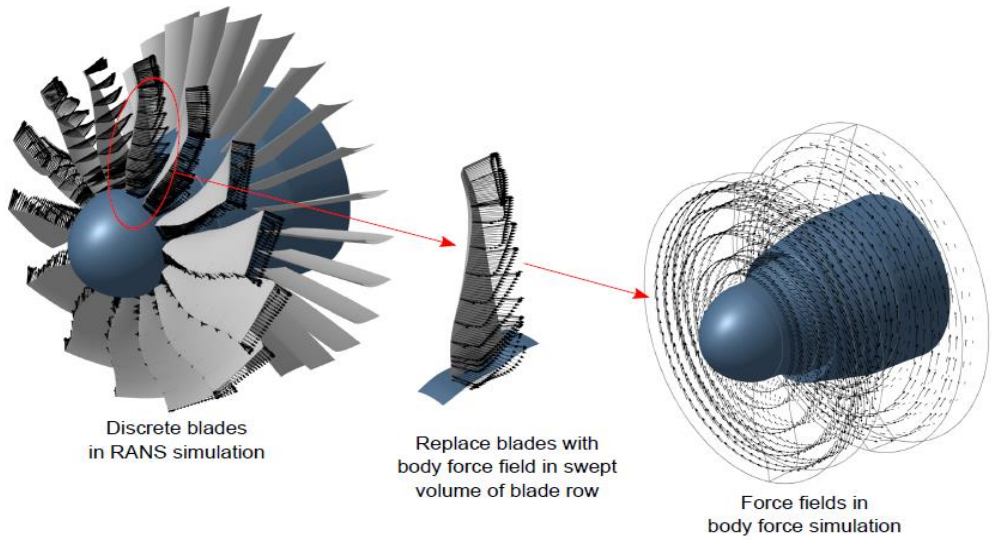

Figure 14 – Blade forces extracted from viscous results to create equivalent body force field [97]

Sorensen [98] extended the above body force model to cavitating turbopumps, with the aim of investigating RC in rocket inducers. The complex secondary flow in turbopumps pose a challenge to body force methods. Sorensen introduced a third force component model in the binormal direction to account for the strong radial flow due to the displacement effect of the backflow. Despite this correction, his one-phase results were limited by pitch angle instability, which kept the cavitation model from being thoroughly tested. Sorensen nevertheless provided an incompressible, isothermal alternative to the Peters derivation of the parallel force, by deriving it directly from the N-S equation. This parallel force model is incorporated to the method devised in the present thesis.

In summary, body force methods are limited to quasi-steady flow with little secondary flow effects. Most importantly, body force methods conceal the local pressure field that drives cavitation. To model the leading-edge pressure drop of the blades, including their geometries in the calculation is essential. The computational cost can still be mitigated by eliminating the near-wall refinement of the computational grid, if viscous blockage is otherwise accounted for. Viscous losses can be mapped onto the inviscid flow field in each individual blade passage, which Xu [80] described as a *Viscous Body Force Method*. The present thesis concerns the development of a *Viscous Body Force Method* with additional models to account for cavity blockage.

3.2. Gap in Knowledge

There is no widely accepted methodology to assess RC in the design phase of rocket inducers. On the one hand, linear analysis methods are limited to small disturbances, neglect three-dimensional effects, and do not account for viscosity. On the other hand, high-fidelity numerical simulations (DNS, LES, U/RANS) are computationally expensive. A reduced order analysis tool is needed to assess RC at reduced computational cost. A simplified model based on first principles derived from the idea of uneven viscous and cavity blockages has the potential of successfully capturing RC, and verifying the physical mechanism associated with it.

3.3. Objectives of Current Research

The present research aims to develop and validate viscous and cavity blockage models to numerically identify the occurrence of RC. The devised computational method mitigates computational cost by reducing mesh dimensions and simplifying the governing equations. The latter is achieved by eliminating the volume fraction equation and the R-P equation [9] [17] of 2-phase mass transfer. Non-axisymmetric behavior is maintained through a link to the local flow field. The devised models include momentum- and continuity sources to account for losses, and streamline displacement due to boundary layer and cavity volume formation.

The proposed simplified analysis method employs the parallel-force model of Sorensen [98] to account for viscous blockage in inviscid simulations. Blade metal blockage is not modeled, since impeller blades are included in the simulations. To account for streamline displacement due to both boundary layer and cavity volume, continuity sources are distributed along the wall, based on the transpiration velocity concept of Lighthill [99]. Models are primarily tested on 2D canonical geometries: the NASA rotor 67 mid-span cascade, the NACA 0015 hydrofoil, and a 2D cascade reported by Iga et al. [100]. The proposed reduced order model is not limited to 2D, and it is expected to capture RC with satisfying accuracy when scaled to 3D. The challenges of scaling the model to 3D are also presented.

3.4. Technical Roadmap

This section aims at describing the simulation setups, model assumptions, and steps of model validation given in Chapter 5. The viscous models (loss & displacement) are first validated on the 2D mid-span cascade of a canonical transonic fan, the NASA rotor 67 (Section 5.1). Next, the viscous models are scaled to 3D, which is demonstrated on the PWA 3-bladed test inducer (Section 5.4). The steady-state cavity model is validated on the NACA-0015 hydrofoil (Section 5.2). Finally, the RC assessment capacity of the transient cavity model is assessed on a 2D cascade (Section 5.3).

Reference simulations for model parameter extraction are executed in Ansys CFX with RANS, an SST turbulence model, and the Zwart formulation of 2-phase mass transfer model (Eq. 15 & Eq. 16). The governing equations are given in Section 4.1. Assuming incompressible, isothermal water, the continuity equation (Eq. 19) reduces to conservation of velocity gradient, the momentum equation (Eq. 22) loses the heat transfer term, and the energy equation (Eq. 23) becomes redundant. The final version of the governing equations is given in Eq. 24. Since Euler calculations are not possible in CFX, inviscid solutions can be imitated by prescribing low viscosity ($\mu \sim 10^{-12}$) and free slip wall condition, with the laminar turbulence model. All axisymmetric cases (Sections 5.1, 5.4, and the one-phase simulations in Section 5.3.1) use the single blade passage approximation with circular periodicity to reduce discretization size. The validation consists of three steps for each model derived: (1) acquiring the geometry, (2) building reference characteristics and (3) assessing model accuracy. Single-phase, steady, axisymmetric, and 2D assumptions are made in the case of the *Viscous Blockage Model* validation. Additional assumptions (A.) are listed in Figure 15 below.

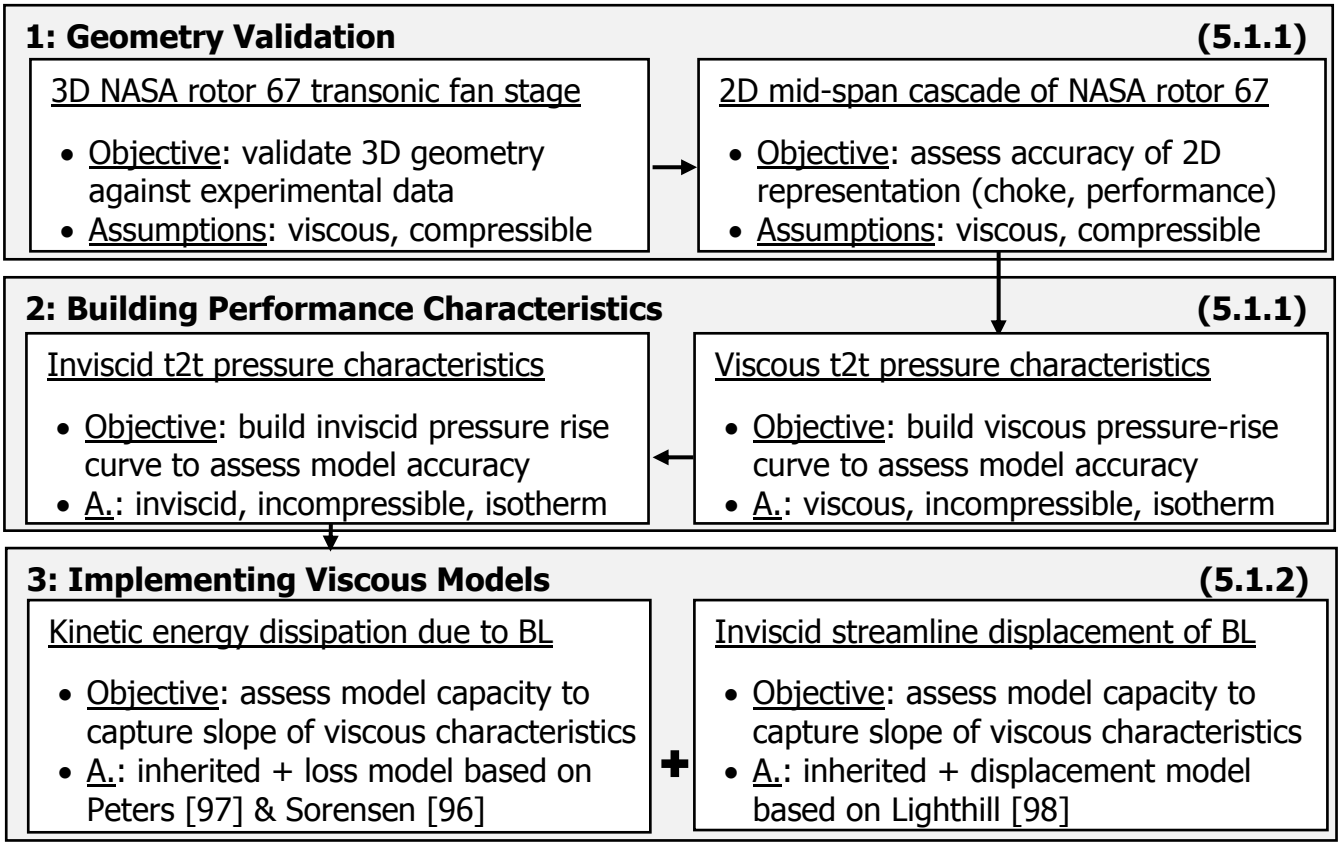

Figure 15 – The *Viscous Blockage Model* is validated on the NASA rotor 67 2D cascade in 3 steps

The validation of the *Cavity Blockage Model* is similar to the validation of the *Inviscid Stream Displacement Model*, derived in Section 4.2.2. First, the steady state cavity displacement model is validated at a variety of cavitation numbers (σ) (Figure 16, 3a), using the 2D NACA-0015 hydrofoil. The RC assessment capacity of the transient model is validated on the 2D flat-plate cascade of Iga et al. [100] (3b). The two-phase flow is assumed to be a mixture of incompressible, isothermal water, and saturated water vapor. Additional assumptions and validation steps are listed in Figure 16.

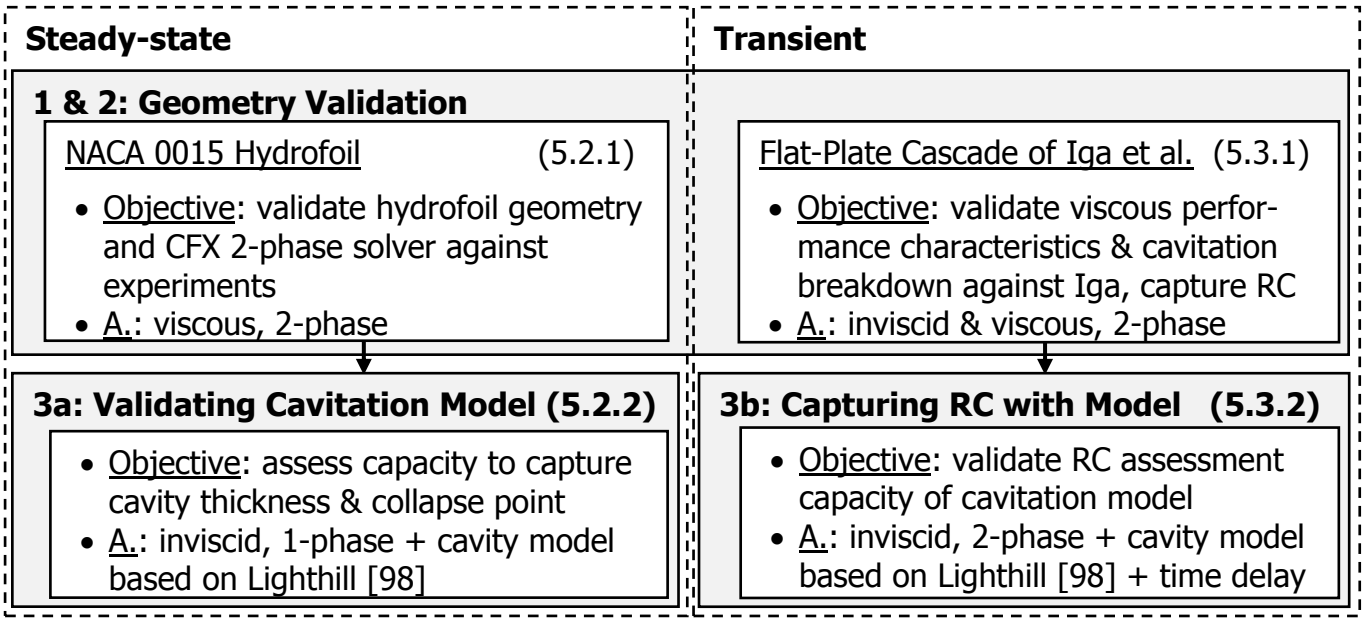

Figure 16 – *Cavity Blockage Model* is validated on the NACA-0015 hydrofoil & a 2D cascade [100]

Finally, the viscous loss and displacement models are scaled to 3D, using the experimental three-bladed rocket inducer of the Pratt & Whitney Aircraft Company (Rockwell inducer). In order to assess viscous losses and boundary layer displacement on the blade, interference effects of secondary flow features must be minimized, which is demonstrated in Section 5.4. For this, three different setups are prepared, following Figure 59: one fully viscous, one where only the blade is assumed viscous and the hub & shroud inviscid, and one the other way around. This is shown in the RHS of Figure 17 ('v': viscous wall setup with *no-slip* wall condition, 'i': inviscid wall setup with *free-slip* condition). Because the proper assessment of secondary mixing losses is critical to indirectly measure blade losses, all three cases are solved with RANS SST, with viscous fluid. The flow is treated inviscid only when assessing the inviscid total-to-total pressure characteristics. The continuum is assumed to be incompressible, isothermal, liquid phase water at 25°C in all cases.

Figure 17 – Challenges of the 3D extension of *Viscous Blockage Model* shown in Rockwell inducer

4

Model Derivation

4.1. Governing Equations of the Numerical Solver

Ansys CFX provides an iterative numerical solution to the mass, momentum and energy conservation equations, by applying the Reynolds Transport Theorem (Eq. 17) to respective flow properties. Eq. 17 describes the balance of intensive flow property ϕ of velocity $\mathbf{u}$ in control volume V, as the ϕ crossing the control surface (A), and ϕ generated within the volume via sources ($\mathbf{s}$).

$$\frac{d}{dt}\int_V \boldsymbol{\phi}\, dV = -\int_A \boldsymbol{\phi}\mathbf{u}\cdot\mathbf{n}\, dA - \int_V \mathbf{s}\, dV \qquad \text{Eq. 17}$$

Applying the Divergence Theorem to the surface integral part (term 1 RHS) in Eq. 17 and the Leibniz rule for differentiation under the integral sign, Eq. 18 emerges. The *left hand side* (LHS), without the source term ($\mathbf{s}$), is commonly known as the property's material derivate, or convective derivate ($D\phi/Dt$), which yields the conservation of ϕ in time and space.

$$\int_V \left(\frac{\partial\phi}{\partial t} + \nabla\cdot(\phi u) + s\right) dV = 0 \qquad \rightarrow \qquad \frac{D\phi}{Dt} = s \qquad \text{Eq. 18}$$

Substituting density (ρ) into ϕ in the above expression for the material derivate, the compressible *continuity equation* takes form in Eq. 19, with continuity source S_C on the *right hand side* (RHS).

$$\frac{\partial \rho}{\partial t} + \nabla \cdot (\rho \mathbf{u}) = \mathbf{S_C} \qquad \text{Eq. 19}$$

Considering momentum ($\rho\mathbf{u}$) as intensive property ($\boldsymbol{\phi}$) in Eq. 18, the *Cauchy momentum equation* emerges in Eq. 20. The source term on the RHS can be divided into pressure-induced acceleration (term 1), momentum loss due to viscous friction (term 2) and the effect of external forces (term 3).

$$\rho \frac{D\mathbf{u}}{Dt} = \nabla \bar{\bar{\sigma}} + \mathbf{S_M} = -\nabla p + \nabla \bar{\bar{\tau}} + \mathbf{S_M} \qquad \text{Eq. 20}$$

Completed with Stokes' expression for the viscous stress tensor (Eq. 21), the *Navier-Stokes* (N-S) equation emerges in Eq. 22. Ansys CFX assumes that the second coefficient of viscosity is $\lambda = -\mu(2/3)$.

$$\bar{\bar{\tau}} = \mu \left[\nabla \mathbf{u} + (\nabla \mathbf{u})^T - \lambda \delta \nabla \mathbf{u}\right] \qquad \text{Eq. 21}$$

$$\frac{\partial (\rho \mathbf{u})}{\partial t} + \nabla \rho \mathbf{u}\mathbf{u} = -\nabla p + \mu \nabla \left[\nabla \mathbf{u} + (\nabla \mathbf{u})^T - \lambda \delta \nabla \mathbf{u}\right] + \mathbf{S_M} \qquad \text{Eq. 22}$$

Finally, the *total energy equation* (Eq. 23) models the energy dissipation due to viscous effects in high-speed cases, such as for a transonic fan stage, where h_T stands for total enthalpy.

$$\frac{\partial (\rho h_T)}{\partial t} + \nabla \rho \mathbf{u} h_T = \frac{\partial p}{\partial t} + \nabla (\lambda \nabla T) + \nabla \mathbf{u} \bar{\bar{\tau}} + \mathbf{u}\mathbf{S_M} + \mathbf{S_E} \qquad \text{Eq. 23}$$

The LHS in Eq. 23 gives the material derivate of the total energy. The RHS is divided into five contributors to energy change: the work of temporal pressure change (term 1), the heat transferred from the boundaries (term 2) and created via viscous friction (term 3), and the energy supplied by external momentum sources (term 4) and volumetric heat sources (term 5). In an incompressible fluid, the effects of viscous heating and momentum sources can be neglected. Assuming that the case is also isothermal (adiabatic boundaries and no volumetric heat sources), terms 2 and 5 can also be discarded. With the above, Eq. 23 decouples from the continuity (Eq. 19) and momentum (Eq. 22) equations, and plays no role in determining flow within blade passages [98]. Assuming the flow to be incompressible and isothermal also simplifies the continuity and momentum equations:

$$\nabla \cdot \mathbf{u} = \mathbf{S_C}$$

$$\frac{\partial (\rho \mathbf{u})}{\partial t} + \nabla \rho \mathbf{u}\mathbf{u} = -\nabla p + \mu \nabla^2 \mathbf{u} + \mathbf{S_M} \qquad \text{Eq. 24}$$

The above set of equations is completed with transport equations of turbulent properties to solve the Reynolds stress, and close the RANS problem. These equations are provided by the SST turbulence model. Finally, in 2-phase simulations, two additional equations are necessary to govern the interphase mass-transfer (Eq. 15 & Eq. 16), and one equation to account for volume fractions.

4.2. Viscous Blockage Models

When accounting for the effect of viscosity on internal flow, one should consider both the momentum loss due to viscous friction, and the flow displacement due to boundary layer growth. The boundary layer is the fluid region adjacent to the wall, where viscous forces are dominant. The boundary layer in a 2D compressor cascade is shown in Figure 18a. A portion of the free stream momentum is dissipated via fluid friction in the boundary layer. This can be regarded as kinetic energy loss, which needs to be accounted for. Viscous flow displacement also needs to be modeled, because of the link between the total energy rise (Δh_T) on the compressor stage and the net turning of the flow. The link is given by the Euler turbine equation, which is derived from the concepts of conservation of angular momentum and energy, given in Eq. 25.

$$h_{T,o} - h_{T,i} = \Omega(R_o U_o - R_i U_i) \qquad \text{Eq. 25}$$

In summary, two different viscous models are required: one to account for the viscous dissipation of kinetic energy, and another to model the stream displacement due to the boundary layer. Kinetic energy loss is modeled with a momentum source term called *parallel force* (f_p), which opposes the local (relative frame) velocity vector (W) of the fluid. This momentum source is applied in a circumferentially uniform manner, and is indicated by the green area in Figure 18b. Boundary layer displacement is modeled via a continuity source term, called *transpiration velocity* (U_n). The mass source at the wall fills the domain normally occupied by the boundary layer, which leads to flow displacement, as indicated in orange in Figure 18b. The figure also displays the different mesh densities required by viscous (Figure 18a) and inviscid (Figure 18b) numerical setups, which determine the computational cost.

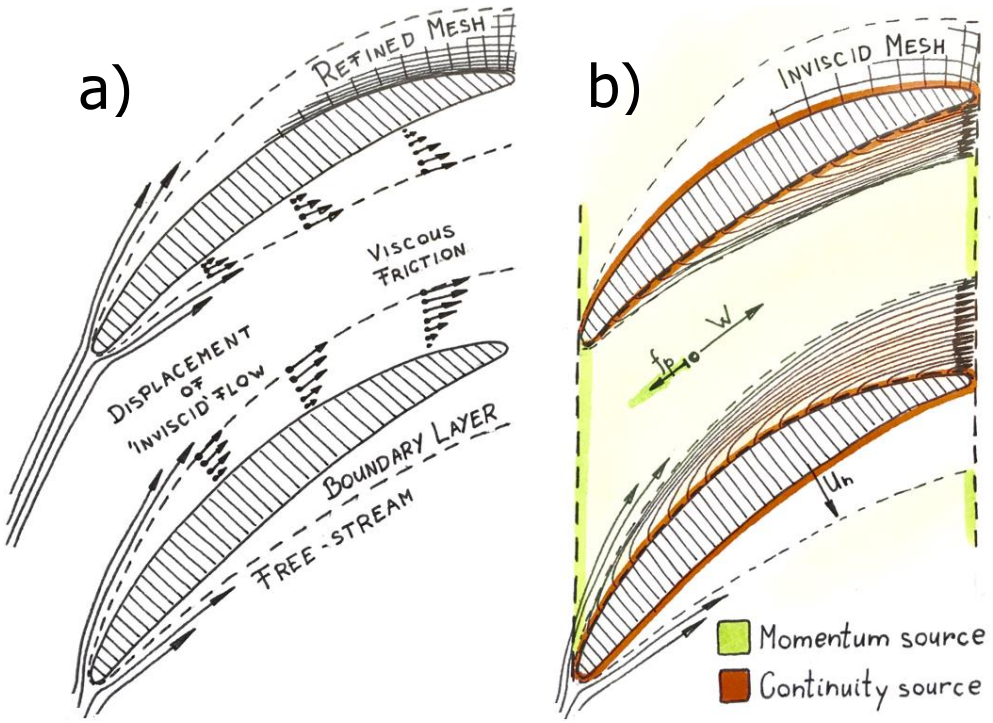

Figure 18 – *Viscous Blockage Model* accounts for viscous friction (momentum sources) and flow displacement (surface sources) to capture viscous flow features in inviscid 2D cascade

4.2.1. Kinetic Energy Dissipation in the Boundary Layer

The kinetic energy loss of the boundary layer is modeled with a momentum source term, called *parallel force* (f_p), whose values can either be extracted from steady state viscous RANS simulations with varying flow coefficients (ϕ), or be accounted for analytically. The parallel force is applied uniformly around the circumference of the blade passage, opposing the local velocity vector, by which it distributes viscous blockage evenly in the pitch-wise direction. The parallel force is a function of the axial (X) and radial locations (R) within the pump, and the local flow rate (ϕ):

$$f_p = f(X, R, \phi) \qquad \text{Eq. 26}$$

In numerical simulations of pseudo-2D flow fields (constant & high radius, one-cell-wide, prismatic), momentum sources must be prescribed in the cylindrical coordinates: x and θ. The link between the cylindrical coordinates and the directions of fluid movement (parallel (p) and normal (n)) is given by the relative-frame flow angle (β). The parallel force components are given in Figure 19, together with visual reference to its circumferentially uniform application. The meridional entropy rise is also given under the cascade, which is discussed next.

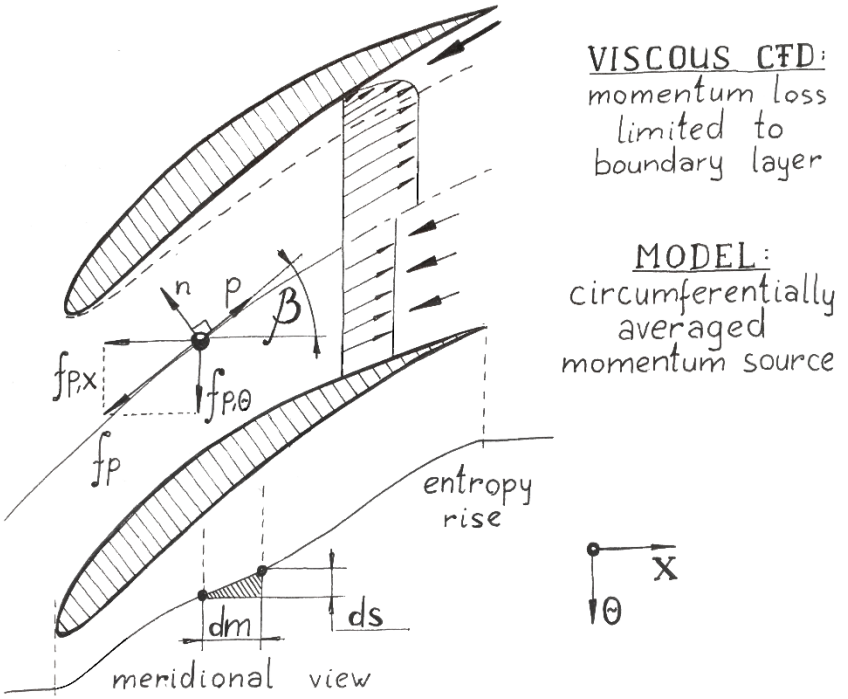

Figure 19 – Energy dissipation modeled with momentum source (f_p) to oppose fluid movement

In his work on the body-force formulation of a transonic compressor fan, Peters [97] derived f_p from the 1st and 2nd laws of thermodynamics, following the work of Marble [101]. In that formulation, f_p is proportional to the pitch-wise averaged entropy generation ($\partial\bar{s}$) in the meridional direction (m), corrected by the pitch-wise averaged relative flow angle ($\bar{\beta}$) and temperature ($\bar{T}$):

$$\bar{f_p} = -\bar{T}\frac{\partial \bar{s}}{\partial m}\cos\bar{\beta} \qquad \text{Eq. 27}$$

Eq. 27 cannot be applied to incompressible, isothermal fluids, which limits its applicability to turbopumps. In constant density fluids with constant specific heat (c_p), the total specific energy rise (dh) is given by Eq. 28. When substituted into the second law of thermodynamics, this yields an expression for entropy rise, which is given in Eq. 29.

$$dh = c_p dT + \frac{dp}{\rho} \quad \text{Eq. 28}$$

$$ds = c_p \frac{dT}{T} \quad \text{Eq. 29}$$

Based on Eq. 29, the model of Peters can no longer be used if the fluid is also assumed isothermal. To overcome this limitation, Sorensen [98] derived the parallel force directly from the steady incompressible momentum equation, which is given along a 1D stream path (l) in Eq. 30.

$$\mathbf{u}\frac{\partial \mathbf{u}}{\partial l} = -\frac{1}{\rho}\frac{\partial p}{\partial l} + \mu\frac{\partial^2 \mathbf{u}}{\partial l^2} \quad \text{Eq. 30}$$

Reorganizing Eq. 30 and rebranding the viscous loss term (RHS, term 2) as f_p, Eq. 31 finally emerges.

$$f_p = \mathbf{u}\frac{\partial \mathbf{u}}{\partial l} + \frac{1}{\rho}\frac{\partial p}{\partial l} \quad \text{Eq. 31}$$

The viscous loss model of the present thesis follows Eq. 31. It is important to assess the capacity of Eq. 31 to capturing viscous losses in simulations where entropy is not defined. For this, the ratio of Eq. 27 and Eq. 31 is plotted on the NASA rotor 67 mid-span profile (Figure 20), which is the same geometry that is used for further viscous model validation. More information on geometry selection is given in Section 5.1.1. The parallel force models of Peters and Sorensen stow satisfactory agreement (over 99%), with discrepancies limited to the laminar sublayer and the edge of the boundary layer. These differences are attributed to the different assumptions of the two cases compared: the Peters derivation of the parallel force was assessed on a low-speed compressible case with heat transfer, while the Sorensen derivation on an incompressible and isothermal case.

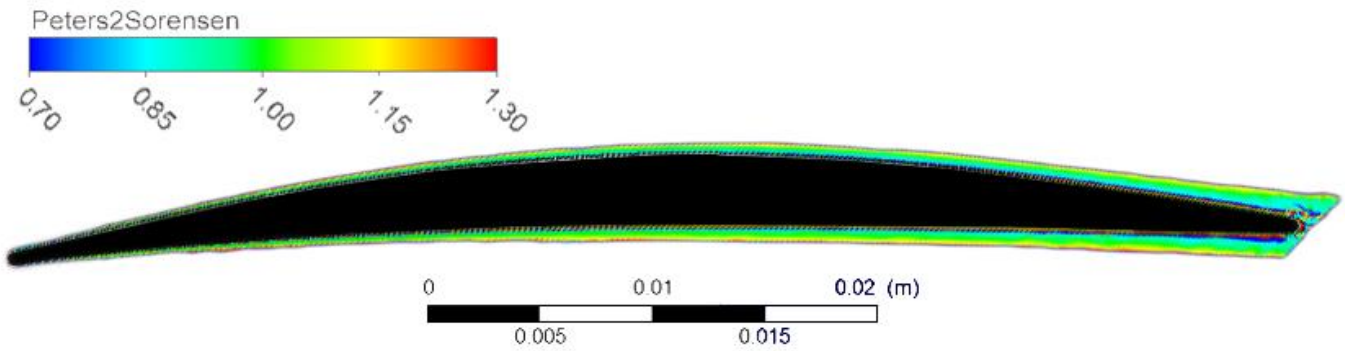

Figure 20 – Parallel force (f_p) models of Peters and Sorensen show satisfactory agreement

4.2.2. Inviscid Stream Displacement due to Boundary Layer

The streamline displacement due to the boundary layer is modeled with continuity sources distributed along the blade surface, which is based on the transpiration velocity concept proposed by Lighthill [99]. Lighthill derived the location-accurate velocity term (U_n), with which new fluid needs to be introduced through the wall, so that it occupies the same displacement domain, as the boundary layer would. The derivation of the stream displacement model is presented below.

Lighthill derived his model by considering the wall-normal velocity component ($u_{n,e}$) at the edge of the boundary layer (δ^*), which is shown in Eq. 32. First, the 2D incompressible continuity equation (conservation of velocity gradients) expresses the boundary layer expansion velocity ($u_{n,e}$) in terms of the tangential velocity. Second, Eq. 32 is extended by the tangential derivate of $u_{t.e}$, which is then subtracted under the integral.

$$u_{n,e} = \int_0^{\delta^*} \frac{\partial u_n}{\partial n} dn \quad \underset{\text{step 1}}{\Longrightarrow} \quad -\int_0^{\delta^*} \frac{\partial u_t}{\partial t} dn \quad \underset{\text{step 2}}{\Longrightarrow} \quad -\frac{du_{t,e}}{dt} n + \frac{\partial}{\partial t}\int_0^{\delta^*} (u_{t.e} - u_t) dn \qquad \text{Eq. 32}$$

This formulation is a sum of what would be present in the irrotational flow around the body (term 1), and a source for additional flow into the displacement domain [99]. Further elaborating on the last term in Eq. 32, one should arrive at Eq. 33, which gives the 2D formulation of what is called the transpiration velocity ($U_{n,2D}$), governing mass flux through the wall.

$$\frac{\partial}{\partial t}\int_0^{\delta^*} (u_{t.e} - u_t) dn \Longrightarrow \frac{\partial}{\partial t}\int_0^{\infty} (u_{t,e} - u_t) dn \Longrightarrow \frac{\partial}{\partial t}\left(u_{t,e}\delta^*\right) = U_{n,2D} \qquad \text{Eq. 33}$$

Figure 21 illustrates the directions n & t, velocities U_t & $U_{t,e}$, and displacement thicknesses δ^* & δ_{bn}.

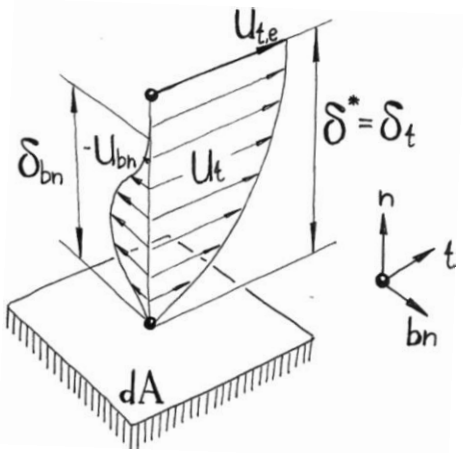

Figure 21 – Edge velocities and displacement thickness of the boundary layer determine the displacement source strengths based on Eq. 33

The displacement thickness (δ^*) in Eq. 33 indicates the normal distance from the wall, at which mass flow rate (or volumetric flow rate in incompressible cases) equals the freestream value (Eq. 34).

$$\delta^* = \int_0^\infty \left(1 - \frac{\rho(n)u_t(n)}{\rho_e u_{t,e}}\right) dn \quad \xrightarrow{\text{incompressible}} \quad \int_0^\infty \left(1 - \frac{u_t(n)}{u_{t,e}}\right) dn \qquad \text{Eq. 34}$$

The transpiration velocity concept is heavily utilized in viscous panel solvers, which provide iterative solutions between the inviscid free-stream and the semi-empirical boundary layer, based on the geometry and flow angle. One of the most popular panel solvers is Xfoil, which was developed by Professor Drela at MIT [102]. Drela referred to $U_{n,2D}$ as the 1D spatial derivate of the *mass defect* of the growing boundary layer. The main difference between the implementation of the transpiration concept in Xfoil and in CFX (which is used in the present thesis) is due to the different nature of the solvers with which the transpiration concept is coupled with. The potential flow solver of Xfoil allows for the direct addition of Eq. 33 to the inviscid surface sources, as shown in Figure 22a.

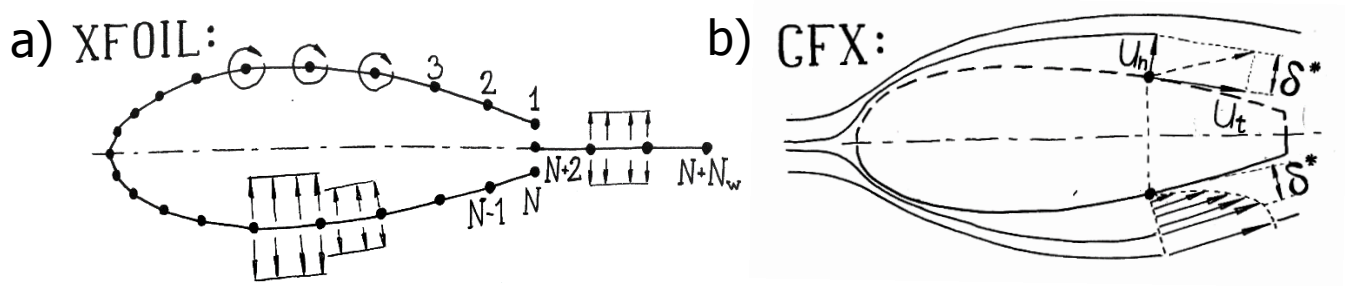

Figure 22 – Transpiration concept can be implemented via wall sources in XFOIL (a), CFX implementation (b) requires tangential component to avoid shear layer instability

However in the current implementation, an unstable shear layer was observed between the source flow and the free-stream, when there was substantial tangential velocity difference between the two. In order to mitigate the excess kinetic energy loss due to mixing, the transpiration flow can be given a tangential velocity component (u_t), which equals the free-stream velocity at the edge of the boundary layer (u_e). This is illustrated in Figure 22b. The CFD implementation of the transpiration velocity concept is limited to isothermal fluids and adiabatic walls, in order to eliminate the modeling of excess heat loss in the displacement domain. Furthermore, the mismatch between the tangential velocities at the edge of the displacement domain and the wall becomes more pronounced around highly curved geometries, or if the displacement domain is thick. The discrepancy in U_t was found challenging to account for during the validation of the one-phase *Cavity Blockage Model*, which limited model accuracy at high σ. Validation results of cavity displacement modeling are further explained in Section 5.2.2.

Momentum balance can be ensured by removing the momentum gain due to wall sources ($S_{M\leftarrow C}$). The relation between continuity and momentum sources is given by Eq. 35, based on the normal (n) and tangential (t) velocities ($\mathbf{u}$) of the mass sources ($\mathbf{S}_C$), given for both the axial (x) and circumferential (θ) directions at every axial location (x). These quantities are provided in Figure 23, which depicts an arbitrary circumferential control volume within the blade passage of a 2D compressor cascade, together with the wall-bound velocity components of the transpiration sources on blades 1 and 2.

$$S_{M\leftarrow C,x}(x) = -\sum_{1}^{2}\left[\mathbf{u_{n,x}}(x)\mathbf{S_C}(x) + \mathbf{u_{t,x}}(x)\mathbf{S_C}(x)\right]$$

$$S_{M\leftarrow C,\theta}(x) = -\sum_{1}^{2}\left[\mathbf{u_{n,\theta}}(x)\mathbf{S_C}(x) + \mathbf{u_{t,\theta}}(x)\mathbf{S_C}(x)\right] \qquad \text{Eq. 35}$$

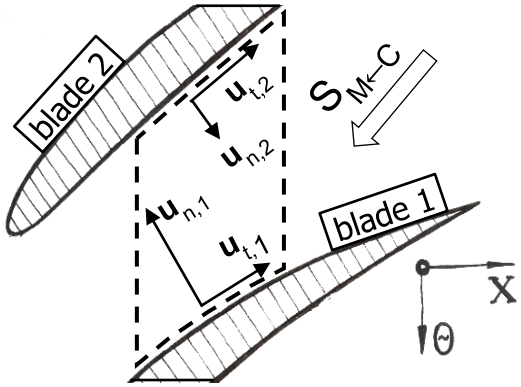

Figure 23 – Corrective source term balances excess momentum introduced by transpiration mass

To ensure mass balance within the system, continuity sinks are implemented in the blade channel. Volume sink strength ($S_V(x)$) is defined as the ratio of the sum of relevant surface sources ($S_S(x)$) over the axial-location-accurate width of the blade channel ($h(x)$). At every x, surface sources of blades 1 and 2 are summed, as shown in Eq. 36.

$$\mathbf{S_V}(x) = -\frac{\sum_{1}^{2}[\mathbf{S_S}(x)]}{h(x)} \qquad \text{Eq. 36}$$

The 3D scaling of the model is given in Eq. 37, for which derivation is provided by Lighthill [99]. In the case of 3D flow, the displacement thickness in the tangential direction (δ_t) equals δ^*. Displacement thickness in the binormal direction (δ_{bn}) is given in Eq. 38.

$$U_{n,3D} = \frac{\partial}{\partial t}(u_{t,e}\delta_t) - \frac{\partial}{\partial bn}(u_{t,e}\delta_{bn}) \qquad \text{Eq. 37}$$

$$\delta_{bn} = \int_{0}^{\infty}\frac{\rho(n)u_{bn}(n)}{\rho_e u_{t,e}}d(bn) \quad \xrightarrow{\text{incompressible}} \quad \int_{0}^{\infty}\frac{u_{bn}(n)}{u_{t,e}}d(bn) \qquad \text{Eq. 38}$$

4.3. Cavitation Blockage Model

When accounting for cavitation blockage, the goal is to capture the streamline-displacement due to an oscillating cavity volume. Since the density of saturated water vapor is five orders of magnitude smaller than that of liquid water at 25°C, the inter-phase mass transfer is negligible. This means,

that the cavity volume can be modeled as a wall, or other non-penetrable displacement domain, which Liuzzi called a "cavity interface tracking method" [87]. In the present thesis, the cavity displacement domain is modeled via the transpiration velocity from Section 4.2.2, where the cavity displacement thickness (δ^*) is defined as the fluid surface of 25% vapor volume fraction. This surface was found to best coincide with cavitation-related changes in the velocity field.

Similarly to the case of the boundary layer, the cavity volume (V_c) is determined by the chord-wise distribution of transpiration velocities, that displace the free-stream. This distribution of sources is determined by the displacement thickness and fluid velocity, which can be extracted from steady 2-phase simulations, or be accounted for analytically. Cavity model parameters at various ϕ and σ populate the dynamic transfer functions K (Eq. 13) and M (Eq. 14), which links the model to theory.

Unlike the boundary layer in Section 4.2.2, blade cavities usually reach their ends within the blade channel, and so the subsequent turning of flow needs to be modeled. This is illustrated around the NACA-0015 hydrofoil profile in Figure 23a. The current implementation extracts the displacement profile directly from the trajectory of the streamline adjacent to the cavity volume, which includes the displacement profile of the recirculating flow. Figure 23b illustrates the streamlines of the transpiration flow, visualizing how it fills the cavity displacement volume, and exits the fluid domain at the back-side of the cavity, also capturing the reattaching flow.

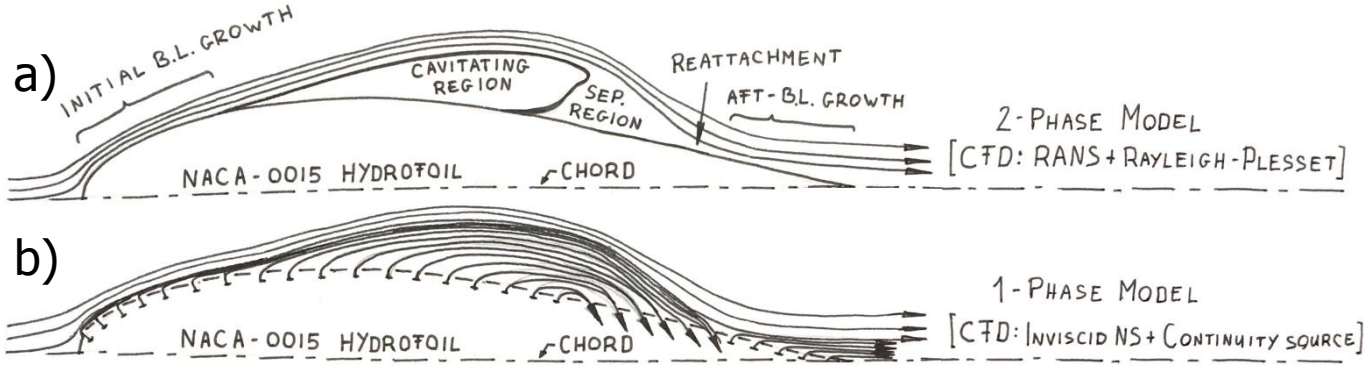

Figure 24 – Cavity displacement is modeled with 1-phase transpiration velocities on 2D hydrofoil

The model validation in Section 5.2 indicates that the transpiration velocity concept captures the cavity displacement within 5% error. This is due to the approximation of the tangential velocity component of the transpiration velocity based on free-stream values, which loses validity as surface curvature grows. Unlike hydrofoils, typical inducer blades are rather flat with a sharp leading edge, and so cascade results are expected to maintain accuracy to lower cavitation numbers. For a proof of concept, a 5% implementation error is acceptable.

Finally, no additional mass or momentum sources are needed to implement the *balanced* cavity displacement model. The word *balanced* refers to a calibrated input source distribution, so that the total mass input and output along the chord are equal. Calibration results for a specific 2D cascade are shown in Figure 46c. This correction provides a passive control over mass balance, which translates into reduced computational cost, but it yields a <1% change in the empirical data and ±0.1% fluctuation in the resulting mass-flows.

5

Results

5.1. Validation of the Viscous Blockage Model

Selecting a well-documented canonical test geometry is crucial for successful validation. Following careful assessment, the NASA rotor 67 was selected over the rotor 37, for its better availability of geometry and measurement data. The low-speed single-stage experimental rig fan of Cambridge University's Whittle Laboratory was also considered, but could not be used for the lack of publicly available profile data.

5.1.1. Test Geometry (NASA rotor 67)

The NASA rotor 67 is an axial-flow transonic compressor fan stage with 22 blades, which was developed at the NASA Lewis research center in 1978, to provide a low-aspect-ratio alternative to the previous experimental fan rigs [103]. The details of the rotor 67 are summarized in Table 1.

Table 1 – NASA rotor 67 main technical parameters

Design Rotational Speed	[RPM]	16043
Tip Diameter	[m]	0.51
Number of Blades	[#]	22
Aspect Ratio	[-]	1.56
Tip/Hub diameter ratio	[-]	2.35
Choking flow coefficient	[-]	0.4
Peak Isentropic Efficiency	[%]	89.6
Total Pressure Ratio at Peak Efficiency	[-]	1.629

The model validation necessitated the development of a canonical 2D cascade geometry, which was generated based on the mid-span profile of the NASA rotor 67. This is illustrated in Figure 25a. NASA reported the blade profiles at 15 separate radial locations [103], of which the 7th is at mid-span. The profile coordinates were approximated with cubic splines, from which the 2D cascade was created in a parametric blade modeler, called BladeGen. To minimize radial flow in the domain, the radius and blade-count were increased tenfold, which reduced the curvature of the domain while maintaining blade pitch. The quasi-2D domain was meshed in TurboGrid, an automated mesh generator for turbomachinery applications, to create a high quality structured mesh. Near-wall mesh refinements ensured the proper mesh for the SST turbulence model by setting the non-dimensional cell thickness ($y+$) to 1 near the wall. The resulting profile geometry was verified against the original NASA geometry and showed >99.9% match, as is reported in Figure 25b.

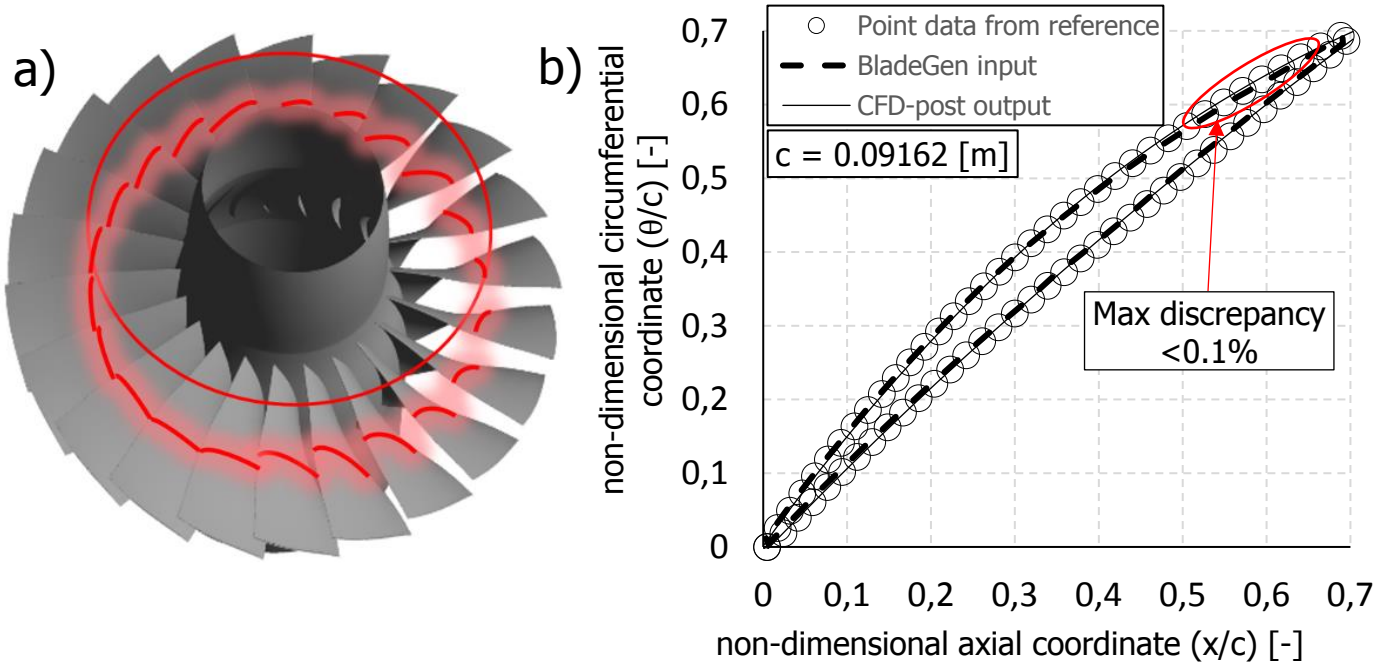

Figure 25 – Profile of the NASA rotor 67 2D cascade (b) agrees with 3D mid-span (a) to >99.9%

Prior to the validation of the blockage model on the 2D cascade, the geometry was validated by comparing the computed performance of the 3D rotor with the experimental data. Simulations are also compared to previous computational works (reported by [104], [105], [106], [107] and [108]). The results are shown in Figure 26 for both the 3D geometry, and the 2D cascade. The boundary conditions were set to total pressure at the inlet and mass flow at the outlet, with the latter being changed to static pressure close to choke condition in order to achieve better convergence. The results of the simulation are indicated with the marker: ■ in Figure 26. The total pressure ratio (TPR) of the computation is captured within 0.1% error of the measured data along the entire operating envelope. The choke condition is captured within 0.9% error. The maximum deviation from other computed data is 0.6%.

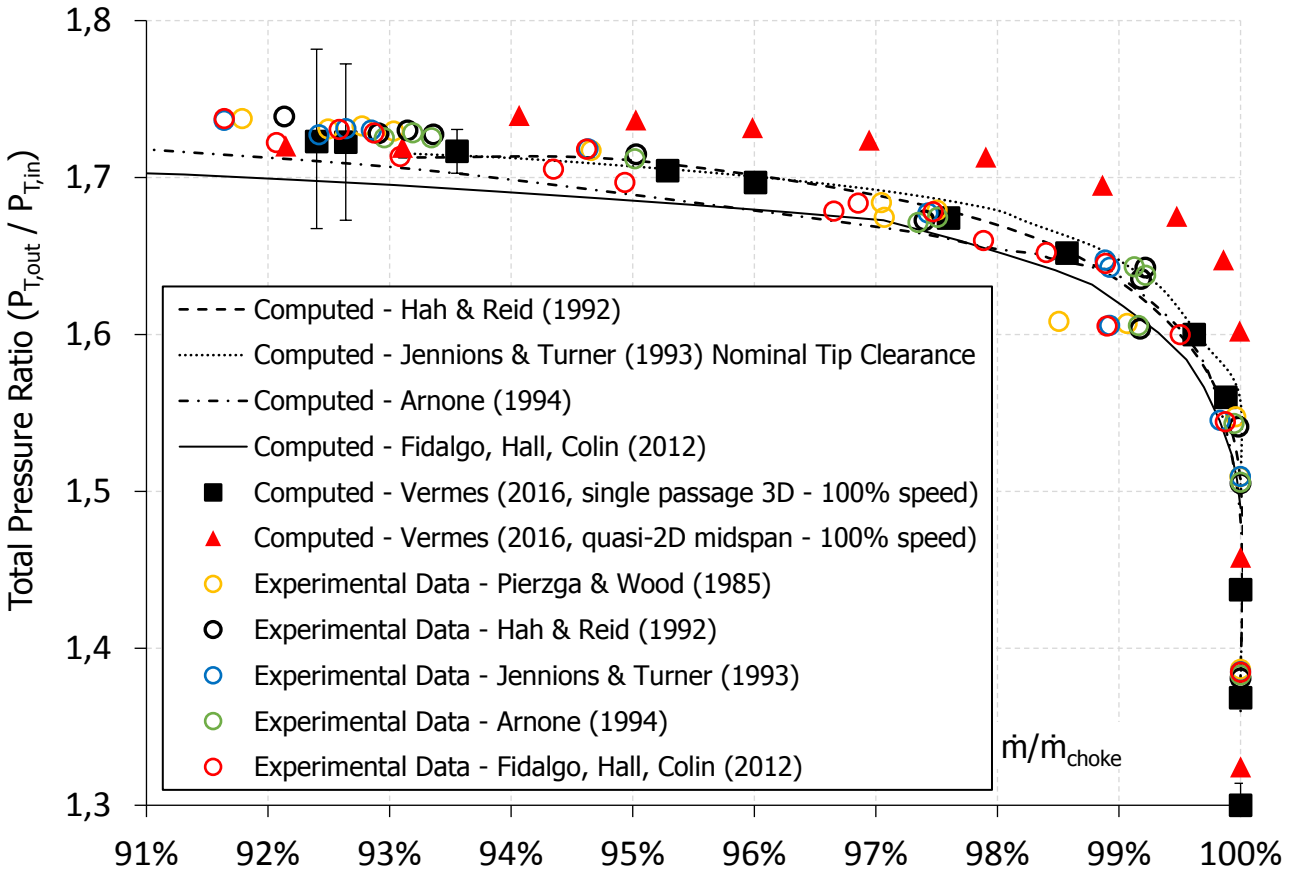

Figure 26 – 3D Ansys CFX results capture performance of the NASA rotor 67 within 0.1% error

The results of the transonic simulations of the 2D cascade are indicated with the marker: ▲. The 2D geometry yields the choking mass flow with 1% error compared to experiments, the maximum TPR (above stall condition) with 0.5% error, and the TPR at peak efficiency with 3% error. These differences are a natural result of the 2D cascade approximation, which assumes identical flow along the entire radius, and eliminates 3D effects.

5.1.2. Validation Results of the Viscous Blockage Model

The viscous model validity was assessed based on its capacity to capture the viscous pressure characteristics of the 2D cascade. Since the Ansys CFX solver uses the viscous *Navier-Stokes* (N-S) momentum equations with a turbulence closure model on discretized 3D domains, it is not directly possible to solve inviscid 2D flows. The workaround is to set a 'laminar' turbulence scheme, inviscid wall conditions (free-slip), very low dynamic viscosity (order < 10^{-12}), and a one-cell wide prismatic geometry with symmetry boundary condition. Because of the non-zero viscosity, the solution supports vortex formation. Consequently, vortices shed from the blade leading edge at high flow angles, limiting the validity of pseudo-inviscid results to a range of flow coefficients around design condition. This range is indicated in Figure 27 between ϕ=0.44 and ϕ=0.55, which might be enough to capture *Rotating Cavitation* (RC) in later simulations.

According to Figure 27, the viscous losses reach a minimum at $\phi \sim 0.39$. Viscous losses in isothermal fluids can be divided into two categories: mechanical losses due to viscous shear forces in the boundary layer and vortex cores, and stream displacement due to reduced flow turning caused by the boundary layer. Capturing the slope of the viscous pressure characteristics is crucial in order to maintain pump stability. To this end, the two main loss mechanisms were accounted for by separate loss models, which are derived from first principles in Sections 4.2.1 and 4.2.2. The resulting pump pressure characteristics are shown in Figure 27. The curves indicate the *Kinetic Energy Dissipation Model* in blue, the *Inviscid Stream Displacement Model* in green, and the combined models in red. The relative slope errors of the predicted viscous characteristics are discussed next.

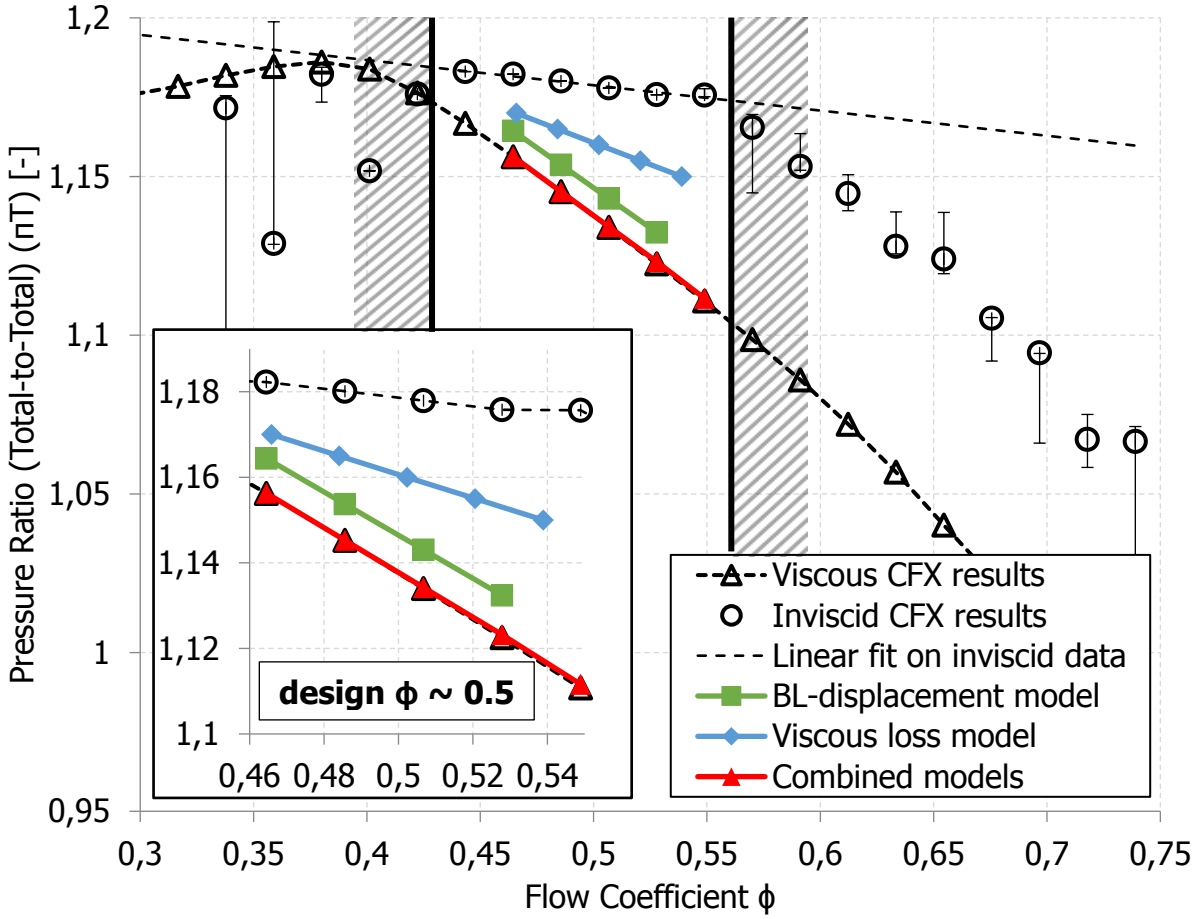

Figure 27 – Individual & combined *Viscous Blockage Model* assessment on the NASA rotor 67 2D cascade show that combined models capture pressure slope of within 0.26% error

The relative slope errors are reported in Table 2 (calculated with Eq. 39), showing that the combined *Viscous Blockage Models* capture the pressure characteristics of pumps with only 0.26% relative slope error and 0.03% average absolute error. The data also suggests that no separate model can capture viscous blockage and flow turning at the same time. This can be explained by the different physical loss mechanisms that the viscous model components represent. The *Kinetic Energy Dissipation Model* captures the momentum loss due to viscous friction, which corresponds more to blockage, while the *Inviscid Stream Displacement Model* captures performance loss due to flow turning. Both mechanisms contribute to the viscous performance loss.

$$\text{Relative Error of Slope} = \frac{\text{slope}_{\text{viscous}} - \text{slope}_{\text{model}}}{\text{slope}_{\text{viscous}}} \qquad \text{Eq. 39}$$

Table 2 – Relative slope error of 2D cascade characteristics with different viscous models

Viscous CFX [%]	0.00 (by definition)
Inviscid CFX [%]	87.71
Kinetic Energy Dissipation Model (Peters & Sorensen) [%]	28.72
Inviscid Stream Displacement Model (Lighthill & Drela) [%]	4.80
Combined models [%]	0.26

During model implementation it was observed that the accurate division of pressure- and suction sides at the leading edge is critical to capturing viscous flow turning. This is because the thickness of the flow displacement domain is sensitive to the initial mass-flux assignment, which may differ significantly between the sides. Since the leading edge stagnation point shifts with flow rate, an appropriate adjustment in the definition of sides is crucial, as shown in Figure 28. Approximating the stagnation point based on the inlet flow angle (and assuming circular leading edge cross-section) was found sufficient to capture the slope of pressure characteristics.

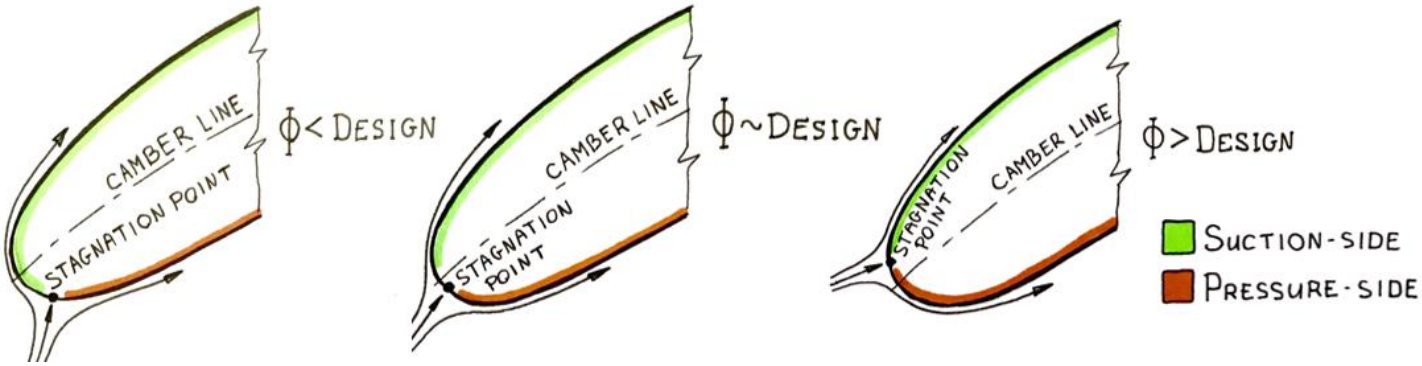

Figure 28 – Flow-angle-accurate division of blade 'sides' is critical to capturing flow displacement

5.2. Validation of the Cavity Blockage Model

The *Cavity Blockage Model* was validated in two steps. First, the cavity displacement capacity of the steady model formulation was assessed on a canonical symmetric hydrofoil, the NACA-0015. Second, the model was applied to transient flow simulations to assess its RC prognostic capability on 2D cascades, which is documented in Section 5.3.2.

Figure 29 illustrates the typical topology of cavity volumes over hydrofoils. The pressure coefficient (c_p) distribution displays key features of cavitating hydrofoils. The most salient effect of cavitation on the pressure field is the characteristic constant pressure plateau under the cavity volume. The plateau is due to the constant pressure inside the cavity, which corresponds to the saturated vapor pressure. Hoekstra [109] demonstrated, that partial cavitation invokes flow separation soon after the inception phase, which results in rapid pressure recovery under recirculating flow. A liquid stream penetrating under sheet cavities (re-entrant jet) is responsible for the dynamic shedding of vapor clouds by impinging on the forward end of the cavity volume. Eventually, the pressure is slowly recovered towards the trailing edge, under reattached flow. The chord-wise pressure coefficient distribution around the NACA-0015 hydrofoil is shown schematically in Figure 29, and it is further discussed in Section 5.2.1.

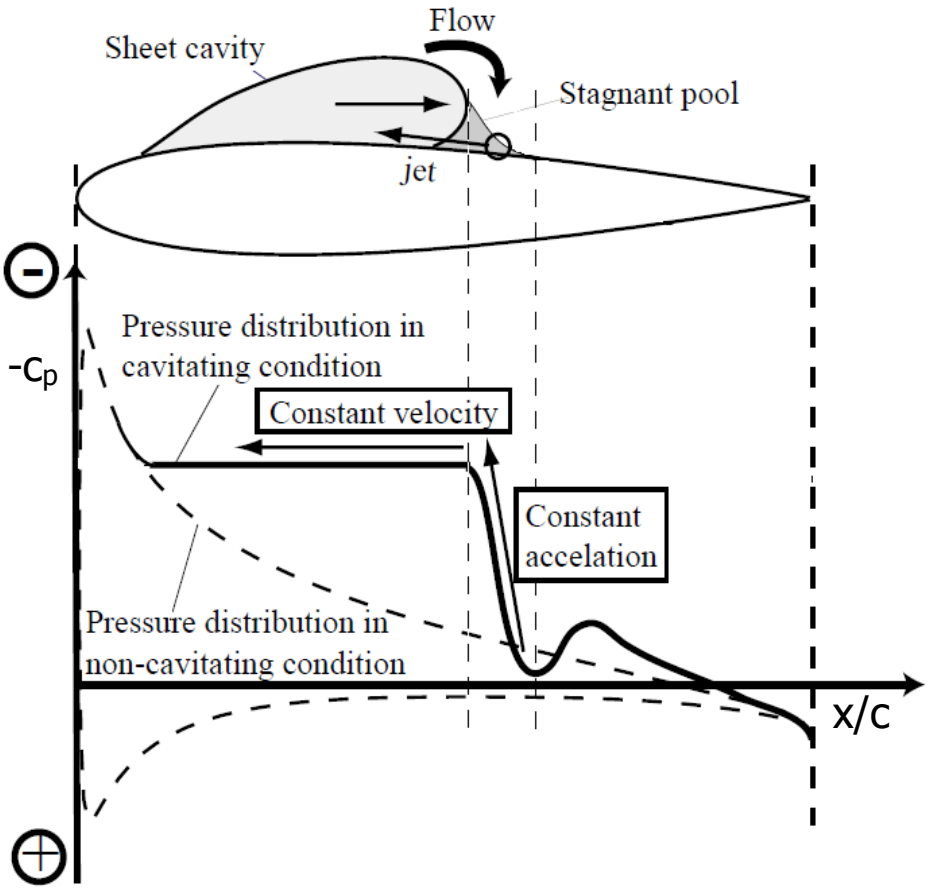

Figure 29 – Typical pressure distribution of cavitating hydrofoils consists of a constant pressure plateau under the cavity, and rapid pressure recovery under the recirculating flow [110]

5.2.1. Test Geometry (NACA 0015)

The steady response of the *Cavity Blockage Model* was validated against two setups of the NACA-0015 hydrofoil, shown in Figure 30. The setup above (Figure 30a) corresponds to a free-mounted case, which is verified against experimental data by Kawanami [111] and simulations by Štigler et al. [112]. The geometry on the bottom (Figure 30b) mimics wind tunnel experiments by Cervone et al. [113], and helps assessing both the σ of unstable cavity inception, and the mean cavity length.

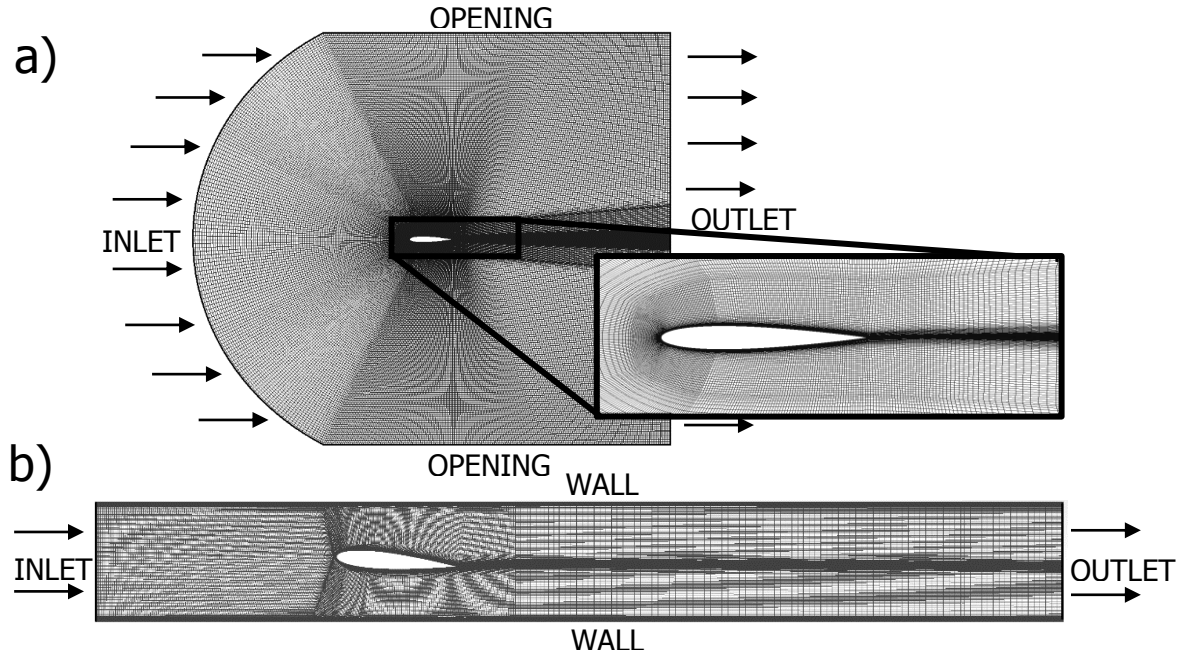

Figure 30 – NACA-0015 validation geometries: free-mounted (a) and wind tunnel (b)

In Figure 31, Ansys CFX results of the free-mounted case are compared to experimental results by Kawanami [111]. Inlet conditions were flow angle of 8 [deg], velocity 8 [m/s], Re 1.3e6 [-], and the outlet pressure was determined from σ. The chord-wise pressure coefficient (c_p) distribution of the non-cavitating setup (Figure 31a) shows over 95% agreement between the simulation and experiment. Under cavitating condition (Figure 31b), the value of the c_p plateau and the position at x/c=0.35 match with experiment, indicating that the cavity extent is well captured.

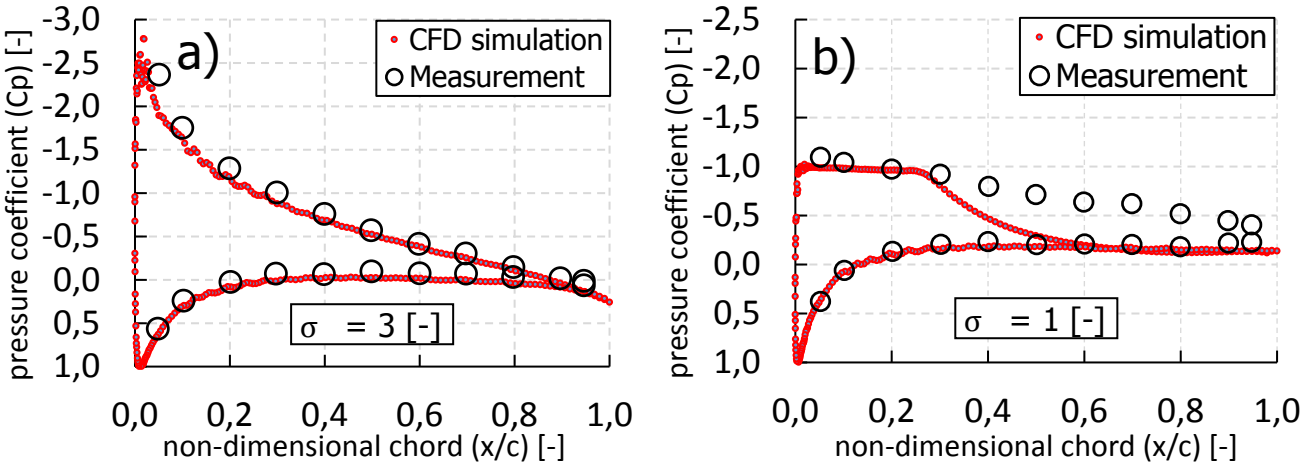

Figure 31 – Non-cavitating(a) and cavitating(b) c_p over NACA-0015 match measurements [111]

The $\Delta c_p \sim 0.5$ difference in the suction-side pressure recovery characteristics in Figure 31b could be explained by the limitation of the numerical method in capturing separated flow. The SST model predicts a steeper pressure rise over the recirculating domain and a later reattachment point than what measurements indicate.

The verification of the Ansys CFX two-phase solver against another commercial solver (Fluent), its different software versions, and two types of cavitation models is illustrated in Figure 32. The reported cavitation models are two-phase (TP) and multi-phase (MP, only available in Fluent). The figure indicates agreement between the capacities of the TP cavitation models of the two CFD solvers for both 6 (a) and 8 (b) degrees inlet flow angle. The difference in cavity lengths predicted by the MP, and the TP models could be explained by the ambiguity of cavity length assessment resulting from the presence of multiple gas phases in MP simulations.

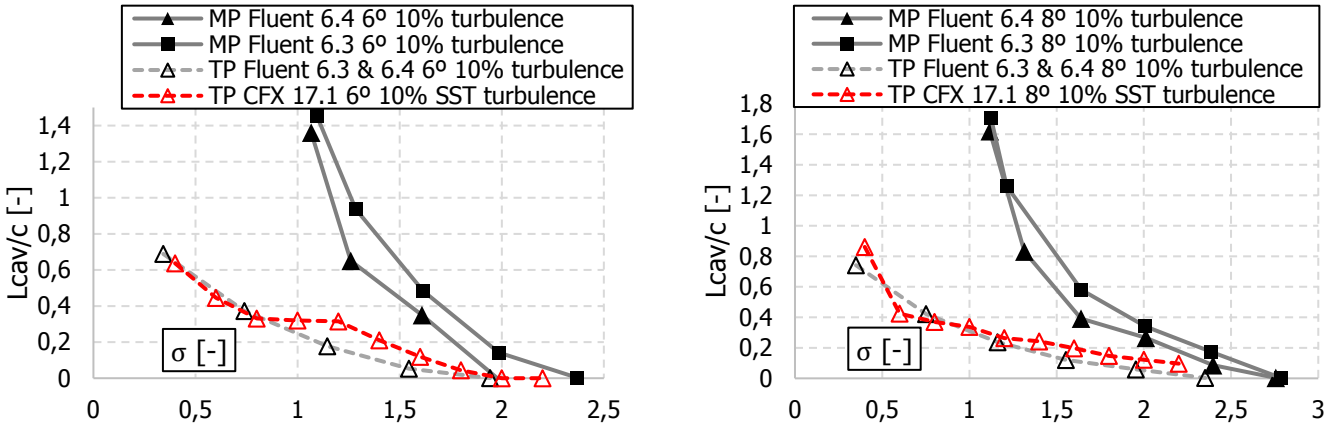

Figure 32 – Ansys CFX two-phase (TP) solver is verified against Ansys Fluent [112]

The validation of the two-phase solver is given in Figure 33. The figure compares simulation results to experimental data of a constrained hydrofoil case by Cervone et al. [113], (Figure 30b). Figure 33 displays the minimum, maximum, and mean values of oscillating cavity volumes over the NACA-0015 hydrofoil. Both the mean cavity length and the inception σ of unsteady cavitation was captured within 5% error in the calculations with respect to experiments.

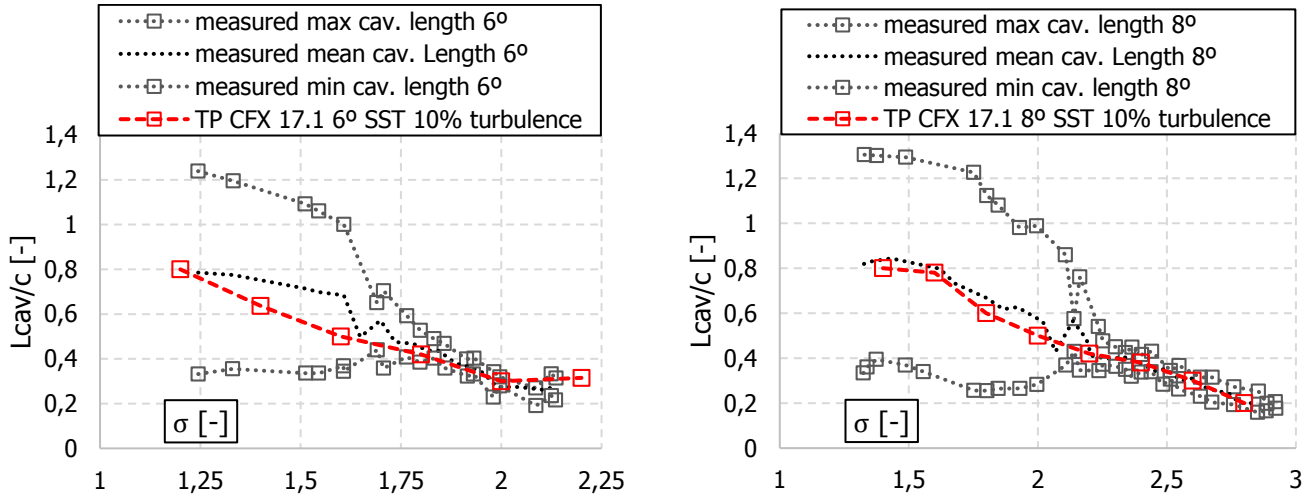

Figure 33 – Mean unstable cavity length validated against wind tunnel experiments [111]

5.2.2. Validation Results of the Cavity Blockage Model

Following the derivation in Sections 4.2.2 and implementation guidelines in 4.3, the *Inviscid Stream Displacement Model* was applied to model cavity displacement in steady-state one-phase CFD simulations. Model parameters were extracted from two-phase calculations. Figure 34 compares the flow field and cavity displacement of two-phase and one-phase simulations. The velocity plots are normalized with the inlet value, and the edge of the cavity volume is indicated in red in Figure 34a.

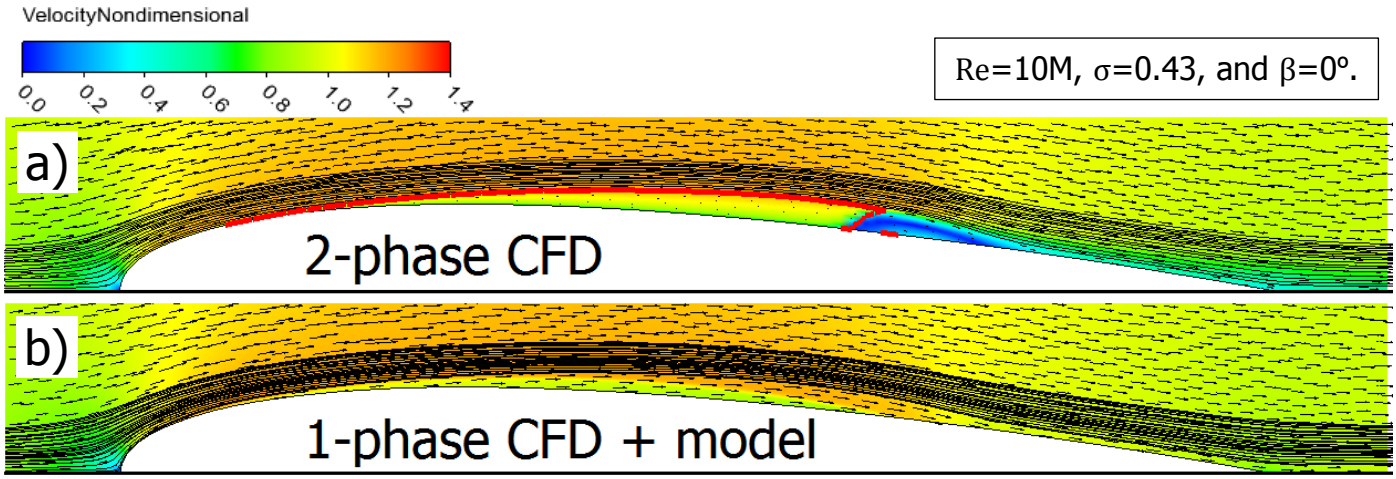

Figure 34 – Qualitative comparison based on Figure 24 indicates good agreement of the cavity displacement and velocity field between two-phase and one-phase simulations

The chord-wise streamline displacement due to cavity formation is depicted in Figure 35 at a wide range of σ, spanning from cavity inception to extensive sheet cavitation. The selected perspective aids the visual assessment of the linear relationship between cavitation number, cavity thickness and the point of cavity collapse, which is further shown in Figure 36.

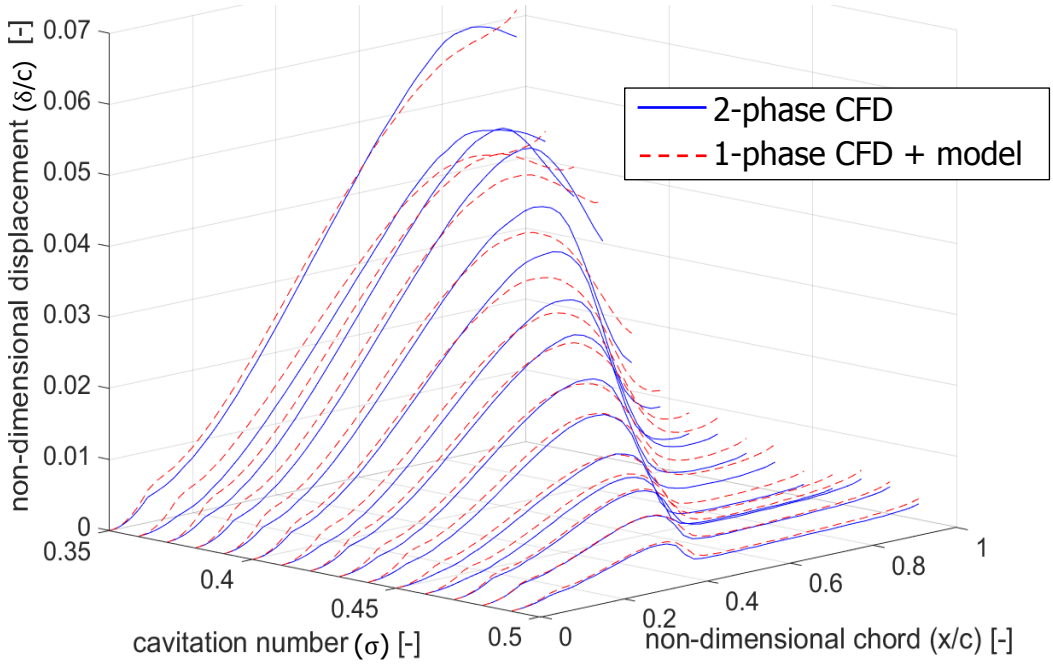

Figure 35 – Quantitative comparison of two-phase and one-phase simulations show 95% agreement of cavity displacement at whole range of σ, sufficient for proof of concept

Figure 36 plots the thickness of maximum cavity displacement and the chord-wise location of cavity collapse against σ, extracted from the two-phase solutions. The relationships are linear, except for values of cavity displacement at high σ, which correspond to cavity inception and initial growth.

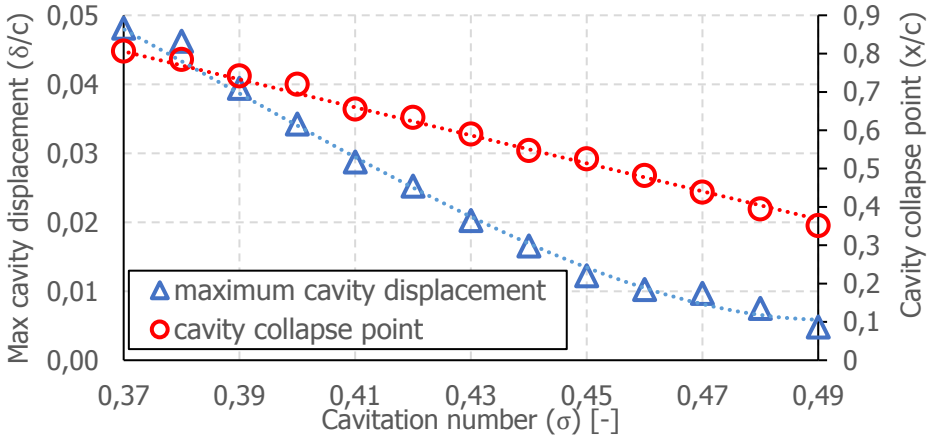

Figure 36 – Two-phase simulations of the NACA-0015 hydrofoil capture linear relation between the maximum cavity displacement, axial cavity extent and cavitation number (σ)

The relative errors between the two-phase results in Figure 36 and the corresponding one-phase results with the *Cavity Displacement Model* are shown in Figure 37. Both cavity length and maximum displacement are 5% under-predicted by the model, which yields sufficient accuracy for a proof of concept. The discrepancy is due to two decisions during the implementation. First, the tangential velocity component of the displacement flow was approximated from the freestream. The link between tangential velocities across the displacement domain weakens as the surface curvature grows, which led to the under-prediction of cavity thickness around hydrofoils. Second, the cavity displacement was extracted from the trajectory of the streamline adjacent to the cavity volume in two-phase simulations. This approximation conveniently captures the displacement profiles of cavities and the recirculating flow behind them, but it does not correct for flow turning around the stagnation point, which affects the initial 10% of the chord of blunt-edge hydrofoils. As a result, the initial displacement profile of hydrofoil cavities needs to be calibrated, or accounted for analytically. In summary, the errors in Figure 37 are due to approximations in the implementation, which are limited by the profile curvature and blunt leading edge of hydrofoils. Inducer blades are typically flat and feature sharp leading edges, which are expected to mitigate the errors in Figure 37.

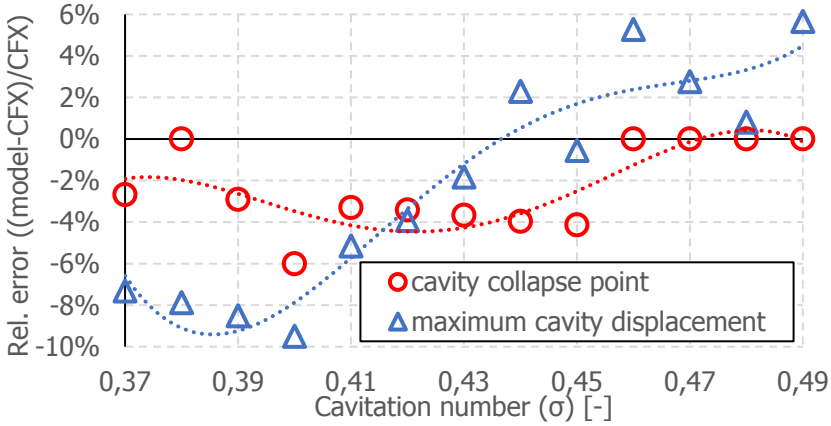

Figure 37 – *Cavity Blockage Model* captures flow displacement by 10% & axial extent by 5% error

5.3. Rotating Cavitation in 2D Canonical Cascade

5.3.1. Iga's Flat Plate 2D Inducer Cascade

In order to assess the capability of the *Cavity Blockage Model* to model instabilities, it was implemented on a canonical 2D cascade reported by Iga et al. [100]. Because of the odd number of blades, *Alternate Blade Cavitation* (ABC) is not possible on the test cascade, and RC develops directly from steady cavities. The geometrical details of the cascade are given in Table 3. The velocity field is displayed in the relative frame of reference in Figure 38, together with the cascade geometry. The simulation setup is explained next.

Table 3 – Main parameters of the 2D cascade adapted from Iga et al. [100]

# of blades	[-]	3
Blade chord (c)	[m]	0.1
Stagger angle (90-γ)	[º]	75
Normalized blade pitch (h/c)	[-]	0.5
Inlet flow velocity (U_{IN})	[m/s]	12
Upstream domain extension (X_{US}/c)	[-]	2
Downstream domain extension (X_{DS}/c)	[-]	3
Monitor plane displacement (X_f/c)	[-]	0, 0.1, 0.15

The inlet boundary condition was defined in terms of the relative flow angle (β) and velocity magnitude (U). The standard static pressure was prescribed at the outlet. The simulation control parameters were flow rate (ϕ, controlled by β) and cavitation number (σ), corresponding to the dynamic transfer functions M (Eq. 14) and K (Eq. 13). Iga et al. [100] controlled σ with the outlet static pressure, but this choice is unpractical, because it necessitates the solver to compute the entire flow field anew for each value of σ. In this work, control over σ was achieved by varying the saturated vapor pressure, which in turn significantly shortened wall clock time. The geometry was constructed and meshed in Ansys ICEM, using 90 x 300 prismatic hexahedral cells for each blade channel. The thin cascade blades were modeled by assigning a different fluid domain to each channel. The geometrical information and flow parameters given in Table 3 are visualized in Figure 38, where blades are numbered B1, B2 and B3. The upstream monitor planes are indicated with dotted lines.

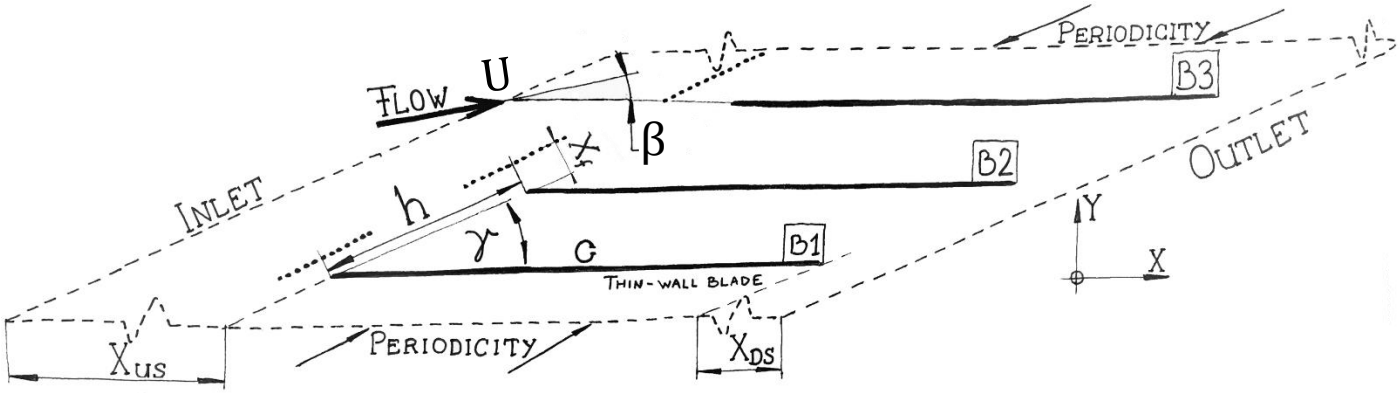

Figure 38 – Geometry and relative frame velocities of 2D cascade adapted from Iga et al. [100]

RC was assessed at discrete values of cavitation number (σ), where its onset was expected based on Iga et al. [100]. The propagation mechanism of RC is hypothesized to be sustained by channel blockage, which alters the local flow field at neighboring blades. The *Cavity Blockage Model* links the stream displacement effect of blade cavities to the upstream flow rate (ϕ), which in turn determines the blockage of each channel. The blade-specific flow rate (ϕ) is a function of the relative flow angle (β), which can be assessed at monitor objects upstream of each blade. To find the link between flow angle and cavity volumes, both monitor points and planes were considered, which is shown in Figure 39. The monitor objects need to be defined upstream in the absolute frame of reference, to minimize the influence of flow turning in front of the neighboring blades.

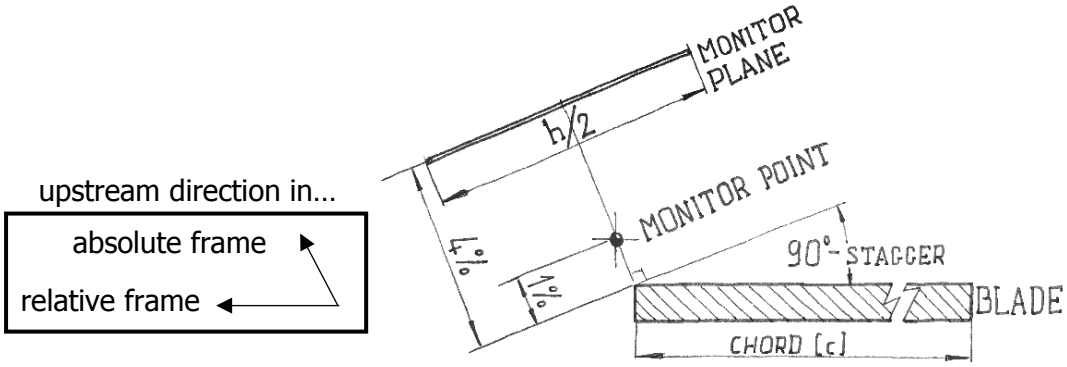

Figure 39 – Model is driven by flow angle (β) at upstream monitor locations (points or planes)

The locations of monitor planes were chosen to minimize interference from neighboring blades, and obtain discrete values of cavity thickness for each flow angle. The latter requirement eliminated monitor point and planes too close to the blade's leading edge, which yielded non-discrete values, as illustrated in Figure 40. The solid lines in the figure indicate transient results from a two-phase RC solution. These results show the hysteresis set by the different time rates of cavity growth and collapse. The path that cavities follow is indicated with arrows. The discrete data points correspond to steady state two-phase solutions, from which model parameters are extracted to drive the *Cavity Blockage Model*. There is no salient difference between the quality of planes positioned sufficiently far upstream (4% to 6% of the chord length) in the absolute frame.

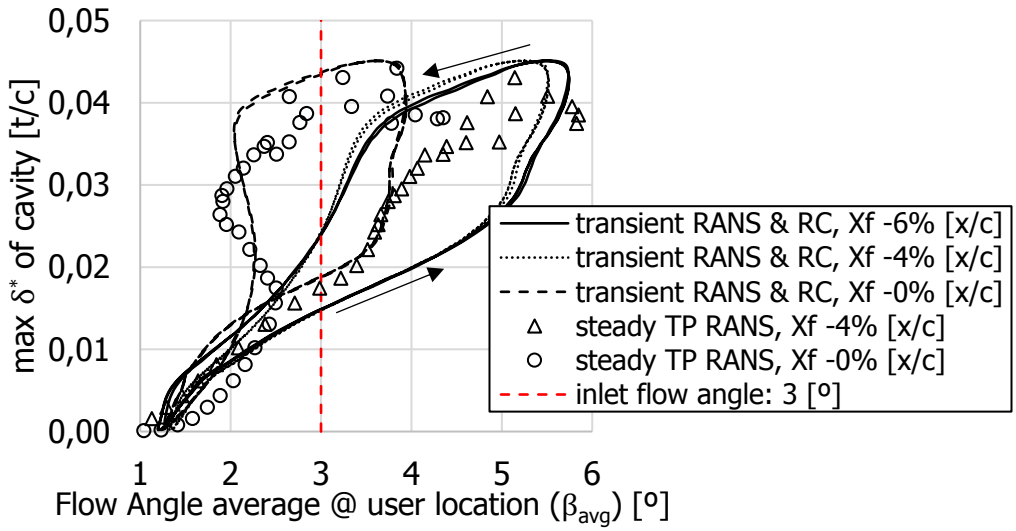

Figure 40 – Monitor planes too close to the leading edge yield non-discrete model parameters

The final simulations were executed using both monitor planes positioned 4% upstream, and monitor points 1% upstream of the blades. When set up correctly in the absolute frame, these monitor objects yielded little difference in model performance, which is discussed in Figure 47 of the following section.

The computed inviscid and viscous pressure characteristics of the cascade are reported in Figure 41, where they are compared with non-cavitating data reported by Iga et al. [100]. The figure shows the Static Pressure Coefficient ($SPC = 0.5\psi$) against ϕ, where the originally reported values of ϕ correspond to 3, 5, 7, 9, 9.5 and 11 degrees relative inlet flow angle. A 20% discrepancy in the viscous data at lower-than-design ϕ could be attributed to the differences between the turbulence model used by the current work and the one used by Iga. The nature of this difference is unknown, and it does not influence model validity. Steady inviscid solution over β=3.5 degrees (ϕ<0.2) showed convergence issues due to leading edge vortex shedding, as reported in Section 5.1.2. The flow coefficient chosen for the transient model validation is indicated by the red dashed line.

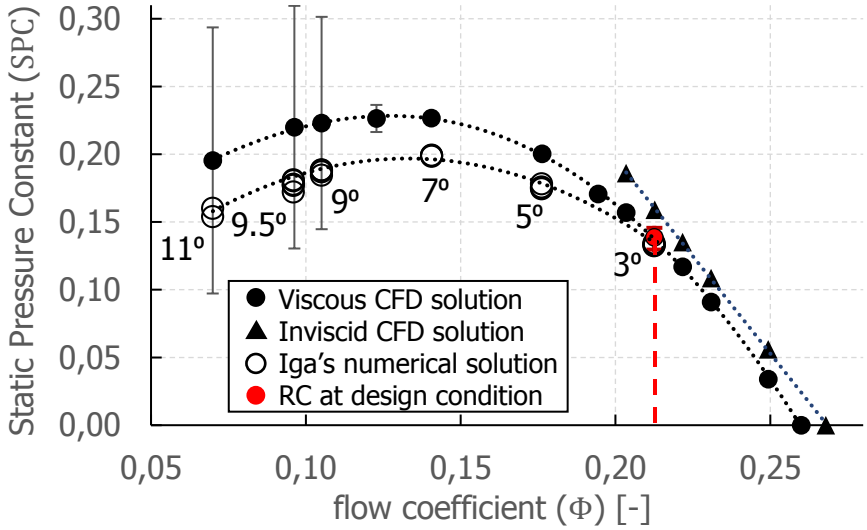

Figure 41 – Viscous pressure characteristics of 2D cascade are up to 20% higher than by Iga, inviscid characteristics limited by vortex shedding, RC reported at design condition

The cavitation performance at the selected upstream flow angle (β=3^0 or ϕ=0.213) is illustrated in Figure 42. The cavitation number at which performance breakdown occurs was captured within 0.1% of the experiment, indicated by the black dashed line. Iga et al. reported RC at a wide range of flow coefficients (0.07-0.21), which is due to the 2D cascade being a crude representation of inducer geometries. In 3D inducers, RC develops near design condition, which is indicated with red markers in Figure 42. To validate the *Cavity Blockage Model*, ϕ and σ were selected, so that:

1. RC is observable within a range of ϕ and σ (± 10%), and the conditions are representative to RC in 3D inducers (near-design flow coefficients)

2. There should be a sufficient range of ϕ around the mean value (± 10%) at which converged steady-state 2-phase simulation data is achievable to drive the cavity displacement model

The condition of ϕ=0.213 (β=3^0) and σ=0.114 was selected for further model validation.

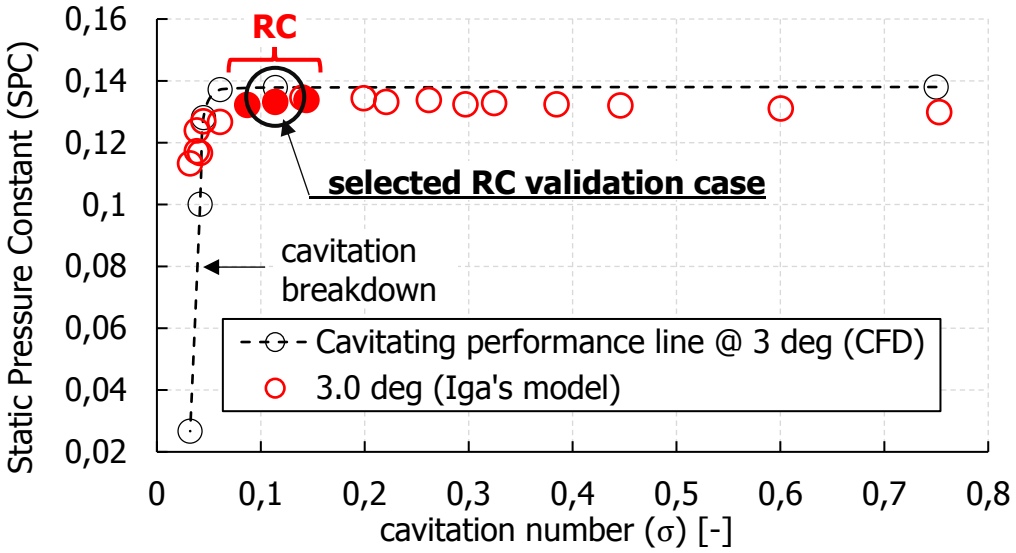

Figure 42 – Selected condition for model validation is σ=0.114 and ϕ=0.213 (β=3^0), the σ of cavitation breakdown is captured within 0.1% error in two-phase simulation

Two-phase calculations need to be initialized from a fully converged one-phase flow field. Because this solution needs to contain vapor-specific variables, the first simulations are set up as two-phase, with only the liquid phase solved. This is achieved by prescribing zero vapor volume fraction (φ_v=0) and disabling the mass transfer model. After convergence, the final simulation can be initiated with mass transfer, which is shown in Figure 43. The figure reports the oscillating lift coefficient on each blade, which is attributed to changes in the extent of blade cavities. Cavities limit the achievable lowest pressure around the blades, by which the pressure distribution and so the blade loading is altered (Figure 29). In general, extensive blade cavities yield reduced lift coefficients, which propagate around the cascade with super-synchronous speeds. Iga et al. assessed the frequency ratio of RC and the rotor via the *Propagation Velocity Ratio* (PVR, Eq. 40). Based on experiments, RC yields a PVR between 1.1 and 1.5. The PVR of the RC detected in viscous 2-phase calculation is 1.24, which is 3% higher than reported by Iga et al. [100].

$$\mathrm{PVR} = \frac{\Omega_{\mathrm{rotor}} + \Omega_{\mathrm{RC(rel.frame)}}}{\Omega_{\mathrm{rotor}}} \qquad \text{Eq. 40}$$

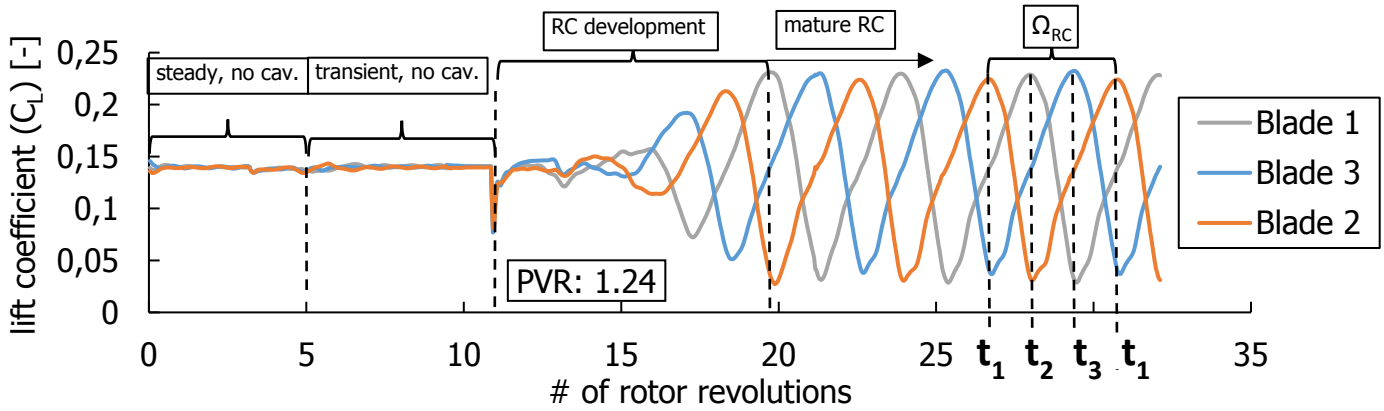

Figure 43 – Oscillating blade loadings indicate RC with PVR: 1.24 in 2-phase viscous calculation

RC was also captured in a pseudo-inviscid case with PVR 1.21 (within 0.1% of the reported value by Iga et al. [100]), which is shown in Figure 44.

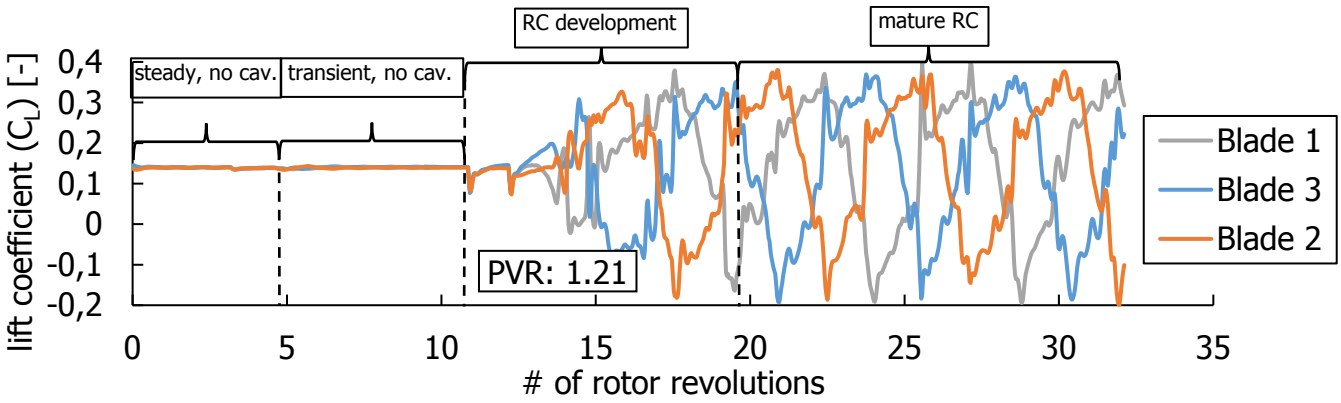

Figure 44 – Oscillating blade loadings indicate RC with PVR: 1.21 in 2-phase inviscid calculation

The positive value of PVR can be visually assessed from Figure 45, where t_1, t_2 and t_3 correspond to a sequence of time steps, where the cavities of different blades reach their maximum extent. The blade order of cavity growth and collapse (3, 2, 1) shows that the detected cavitation instability rotates forward, which is a strong indicator of RC. The depicted blade conditions agree with the propagation mechanism of RC, depicted in Figure 6.

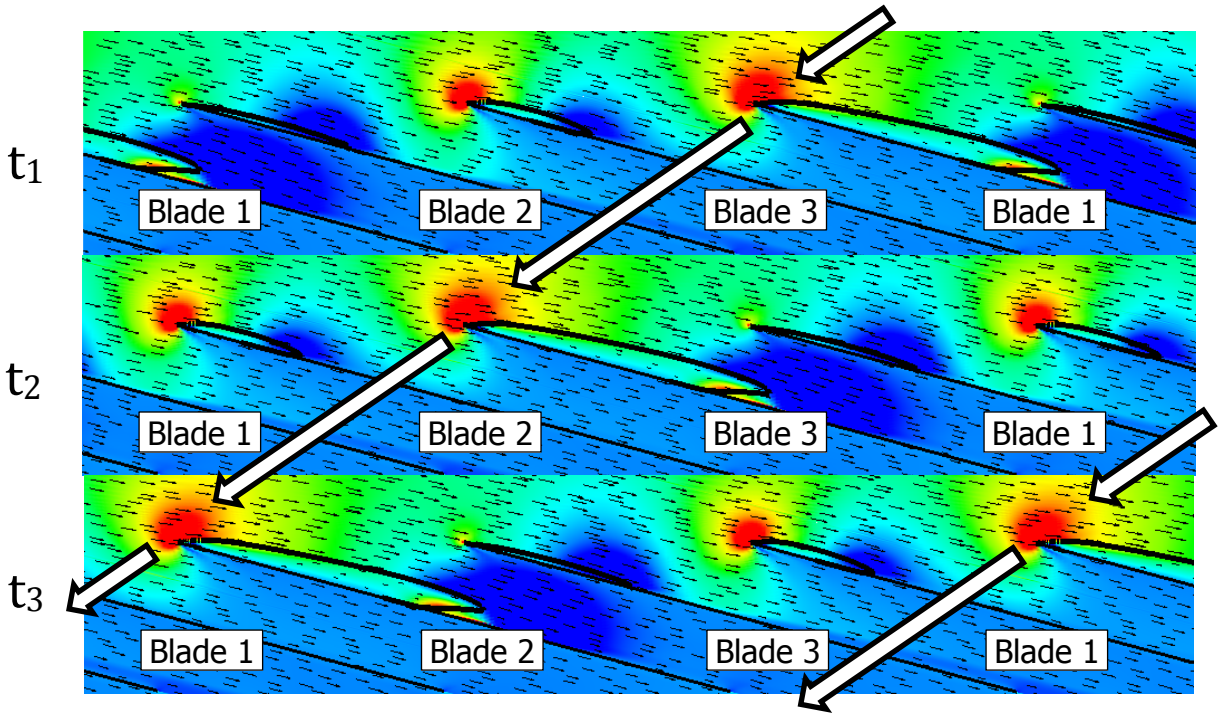

Figure 45 – Two-phase flow field of the 2D cascade of Iga et al. [100] reveals forward propagating mechanism of RC in agreement with Figure 6

5.3.2. Rotating Cavitation Prediction with Cavity Model

In 2D blade channels, the viscous flow blockage is negligible compared to cavity blockage, which alone characterizes the interaction mechanism of RC. The above statement is supported by a marginal PVR difference (3%) between the RC captured in viscous and inviscid simulations. Based on the above, the *Cavity Blockage Model* is assumed to be sufficient to capture RC in 2D inducer cascades, which is demonstrated next.

Corresponding to the selected RC validation case in Figure 42, the following simulations were executed at constant cavitation number (σ=0.114). The *Cavity Blockage Model* needs to be populated with chord-wise transpiration velocity distributions ($U_n(x)$) at various ϕ around the mean value (ϕ=0.213 → β=3 deg). $U_n(x)$ is derived from the displacement thickness (δ^*) and velocity (U_t) of the cavity volumes, which can either be generated via a simplified analysis, or be extracted from measurements. In the present thesis, model parameters were extracted from steady state two-phase CFD simulations, which represents a semi-empirical approach to populating the model. Figure 46 provides a tangible link between the inputs (δ^* & U_t), and the output (U_n) of the *Cavity Blockage Model*. Data labels determine the inlet relative flow angle through n in Eq. 41, with label '17' corresponding to the mean inlet β_i. The LHS plot gives the trajectory of the streamline closest to the fluid boundary of 1% vapor volume fraction, which also captures the profile of reattaching flow. The central plot reports the velocity component tangential to this streamline. Finally, the RHS plot displays the transpiration velocity distribution based on Eq. 33. In a passively balanced model, the integrals of positive and negative function values must equal out (Section 4.3), which is achieved via the <1% corrections shown in red.

$$\beta_i = 0.125 * (n + 7) \text{ [degree]} \qquad \text{Eq. 41}$$

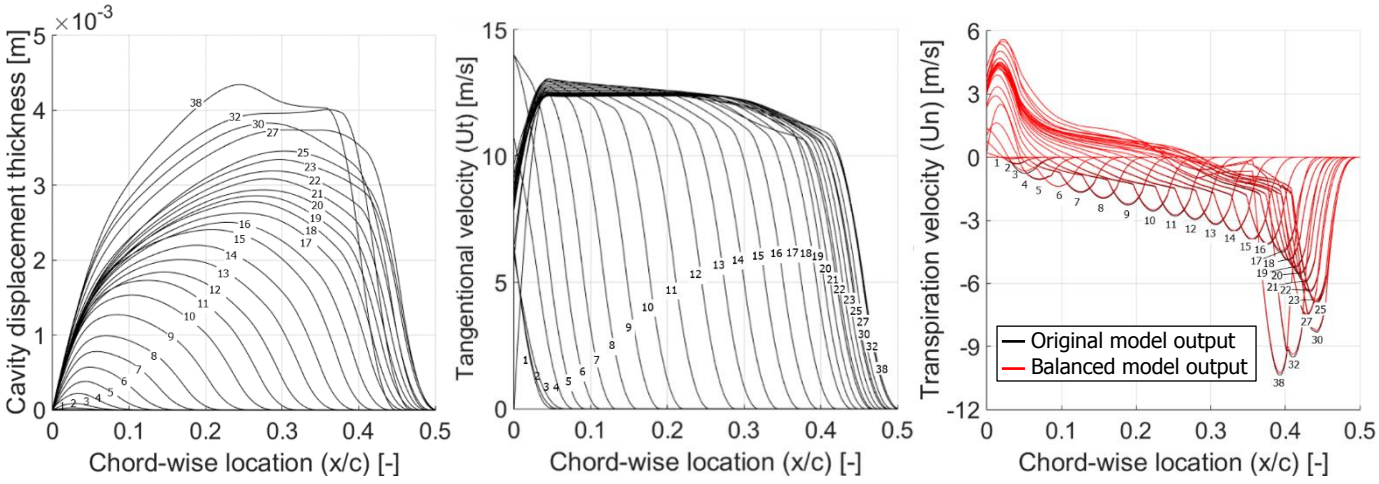

Figure 46 – Transpiration velocities need to be calibrated to *balance* the mass in- and outputs

The most RC-critical property of the cavity volume is its maximum thickness, which is plotted against the average upstream β in the LHS image of Figure 47. The image displays the δ^*_{max} of both transient and steady two-phase RANS results, at two monitor objects: a monitor plane 4% upstream of the blade in the absolute frame (blue, adapted from Figure 39), and a monitor point 1% upstream (red).

RC was successfully captured in one-phase inviscid simulations, both by using monitor planes and points to drive the *Cavity Blockage Model*. In Figure 47, the RHS image shows the oscillating flow angle (β) on the monitor point (top) and plane (bottom) in one-phase simulations. In the case of the monitor point (red, LHS), the non-discrete flow angle data was corrected manually, by mapping it onto the transient line of growing cavities (black, LHS). Because of this non-discreteness, only the RC results driven by the monitor plane are discussed below.

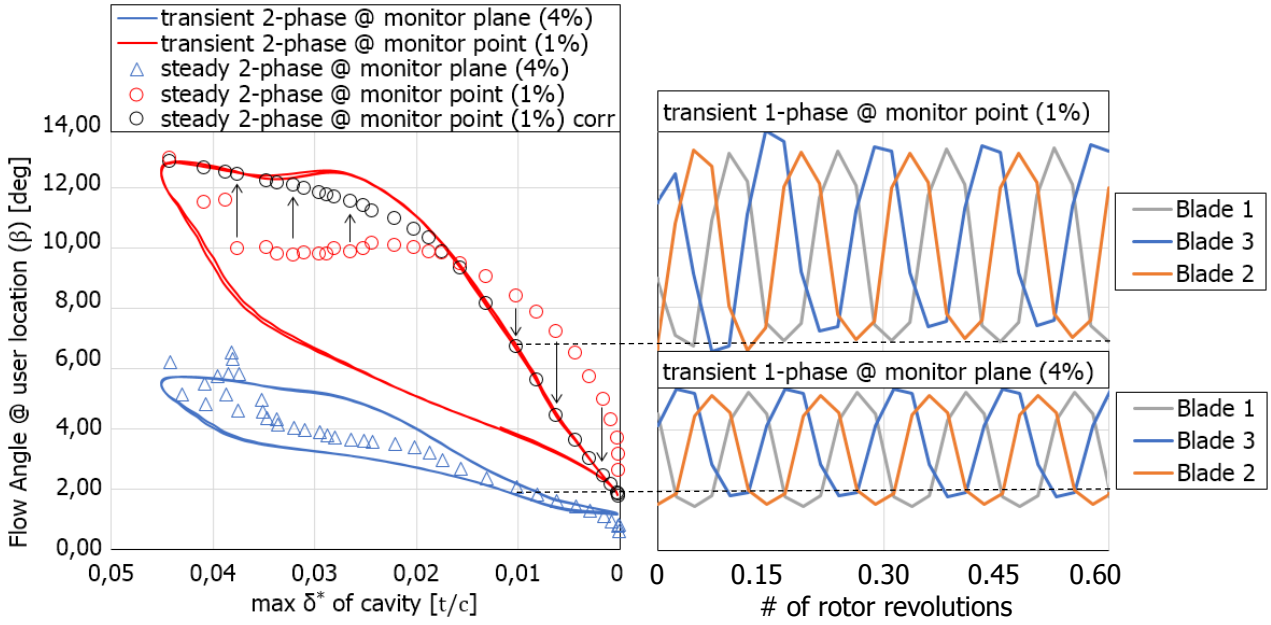

Figure 47 – RC is captured in one-phase simulations of the 2D cascade using the *Cavity Blockage Model*, which is driven by upstream flow angles at both monitor points and planes

The oscillatory blade loadings of the one-phase RC assessment are given in Figure 48, with amplitudes comparable to the two-phase solution shown in Figure 44. As the time-rates of cavity growth and collapse are not modeled, the blade cavity volumes respond to the upstream β instantaneously. Consequently, the PVR is governed by the time rates of fluid dynamics, which are much faster than the time rates of cavity growth and collapse. This results in a PVR of 6.32, considerably higher than the expected value of 1.21. Despite the limited model capacity to indicate PVR, RC is clearly identifiable in Figure 48, from the order of lift variation on the blades.

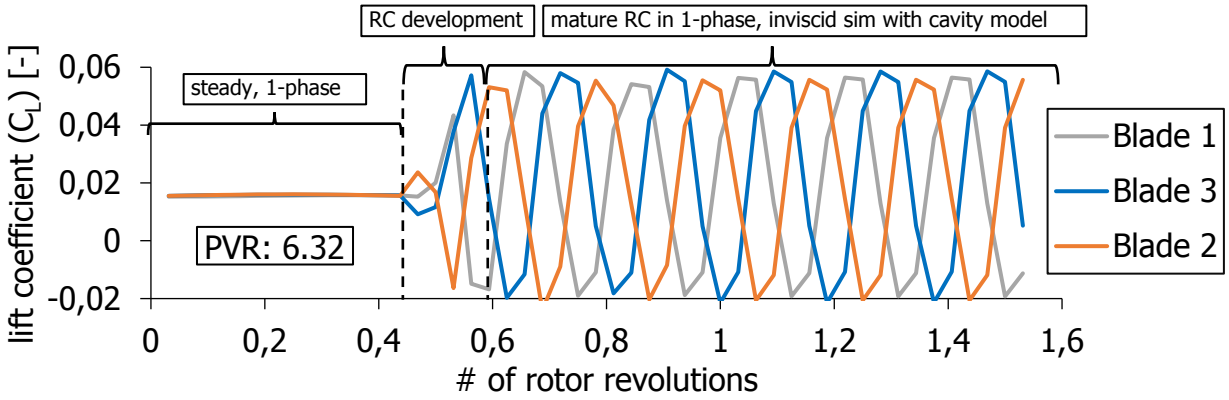

Figure 48 – RC propagation mechanism captured with *Cavity Blockage Model*, but PVR too high

In Figure 49, the flow field of the captured RC (bottom) is compared to the corresponding time step in a two-phase simulation (top). The two model setups yield almost identical flow fields, with slightly larger flow angles in the one-phase results due to the insufficient modeling of cavity dynamics. This shift in β is most evident in Figure 47, where the one-phase transient flow angles (right) only yield blade cavity volumes whose normalized thicknesses are higher than 0.1 (left). In Figure 49, the cavity domain is visualized by the fluid boundary of 1% vapor volume fraction in the top, and with streamlines initiated on the blade surface in the bottom.

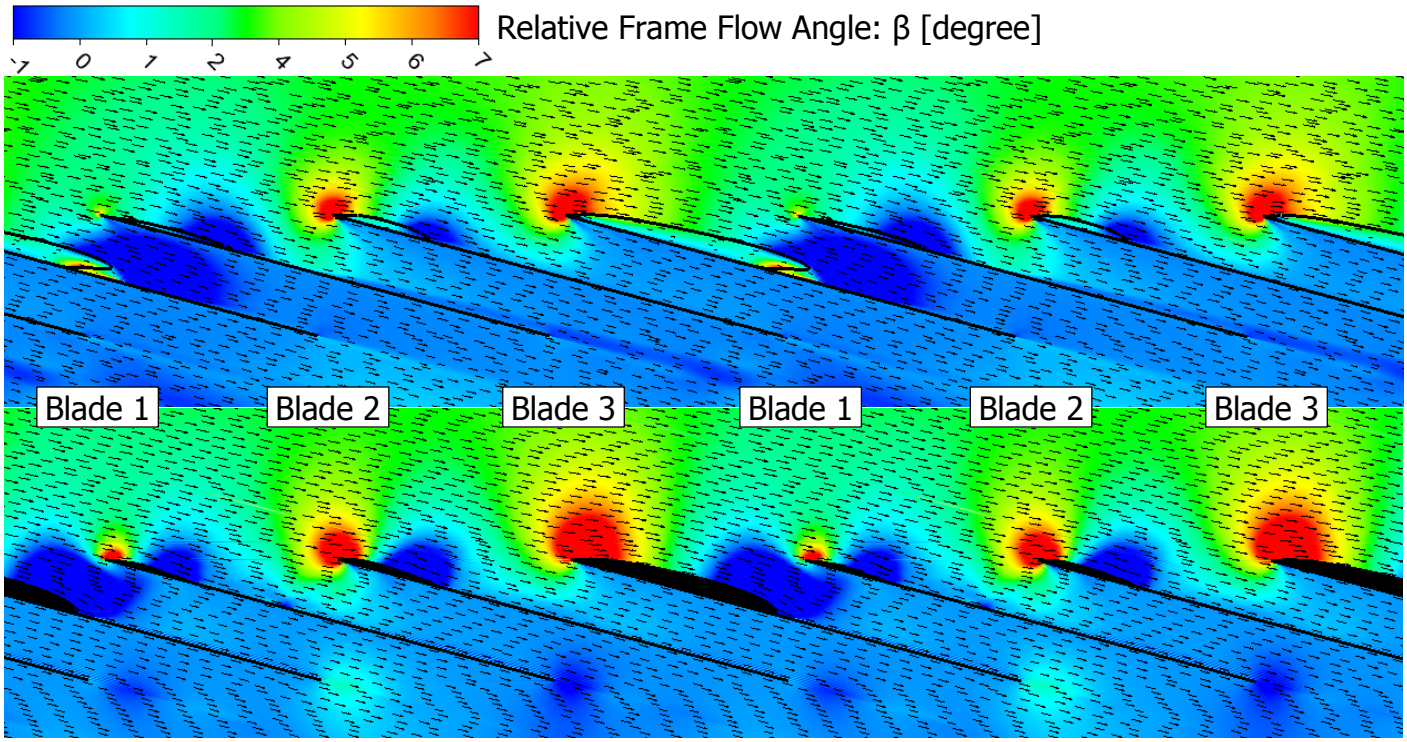

Figure 49 – Flow field of RC captured with satisfactory accuracy using *Cavity Blockage Model*

The discrepancy in PVR (and the inherent overshoot of flow angles) could be corrected by modeling the time-rates of cavity growth and collapse, and accounting for the time which information takes to propagate from the monitor object to the blade. These effects of time can be modeled individually:

1. The β hysteresis in Figure 47 is a result of the different time rates that characterize vaporization and condensation. These time rates are accounted for by the coefficients F_{vap} and F_{cond} in the Zwart formulation of the R-P equations, which drives the 2-phase model of CFX (Eq. 15 & Eq. 16). In theory, the dynamic behavior of cavities is characterized by their response to changes in the cavitation number (σ) and flow rate (ϕ), given by the *Cavitation Compliance* (K) and the *Mass Flow Gain Factor* (M). The fundamental difference between the *Cavity Blockage Model* and M, is that M prescribes cavity growth with respect to a change in ϕ, whereas the cavity model assigns cavity volumes to the absolute values of β.

By limiting the maximum rate of cavity growth per time step, the effect of M could be mimicked, and the interaction mechanism of RC slowed down, which is shown in Figure 50. In the LHS of the figure (based on Figure 47), a time step from t_1 to t_2 would result in a $\Delta\beta$ change in the upstream flow angle with instantaneous model response. By limiting the maximum physical growth rate of cavity volumes, as shown in the RHS of the figure (based on Figure 46), the $\partial\beta/\partial t$ decreases, and so the PVR drops. Unfortunately, the implementation of reduced order cavity dynamics is not possible in the standard Ansys CFX, because the bookkeeping of the source strength history requires access to previous time-steps. A work-around user routine could be written in FORTRAN, which would have exceeded the scope and time constraints of the present thesis, and has therefore not yet been implemented.

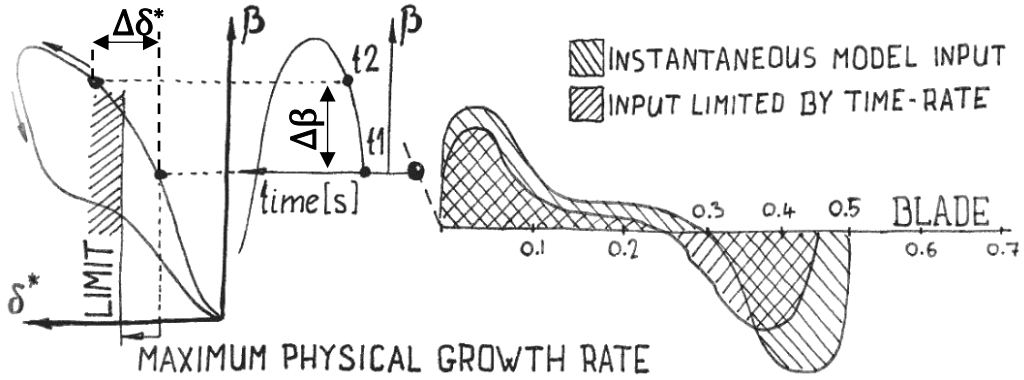

Figure 50 – *Mass Flow Gain Factor* (M) can be implemented to limit cavity growth rate

2. Another contributor to PVR is the time that the upstream $\Delta\beta$ information takes to reach the blade. This can be implemented in CFX via monitor statistics, which store the time history of β, shown in Figure 51. Solving 30 time steps per rotation ($dt = 0.0004\ s$), and assuming that the information propagates with the fluid velocity ($U_t = 12.5\ m/s$ based on Figure 46), the cavity chord can be divided into 10 different sections, all influenced by a different state of the upstream β. After implementation in CFX, this model yielded a PVR of 2.7, which is a 76% improvement to the instantaneous model response. Consequently, the mass flow discrepancy of the balanced cavity model increased to 3%.

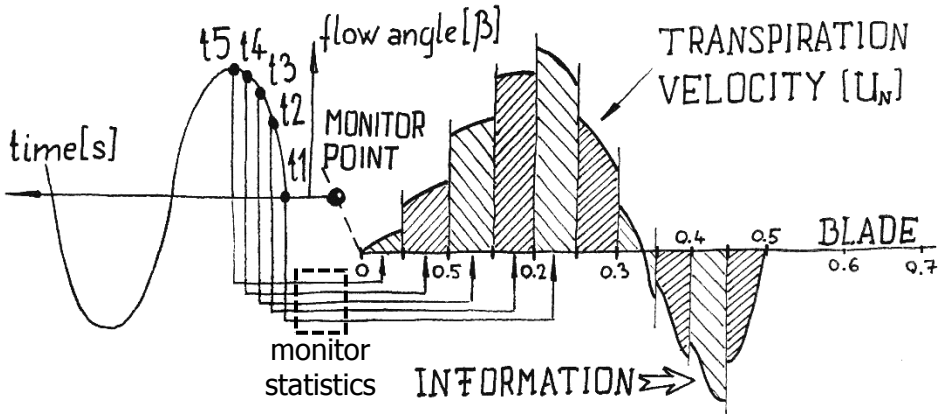

Figure 51 – Modeling Information Propagation Velocity (IPV) along the cavity saves 76% on PVR

It is possible to achieve the expected PVR by calibrating the Information Propagation Model, for demonstrative purposes. The calibration produces distorted blade cavity profiles at extreme low information propagation velocities (IPVs), which are not physically valid. Also, the assumption that the PVR is set only by the IPV is flawed, as the time-rates of cavity dynamics are arguably more important. Calibration results are shown in the LHS of Figure 52, where the target PVR is reached assuming an IPV of 0.8 m/s within the fluid, which is unphysical. The RHS image of the figure gives the relationship between the PVR and the time steps per RC period, which is defined by Eq. 40.

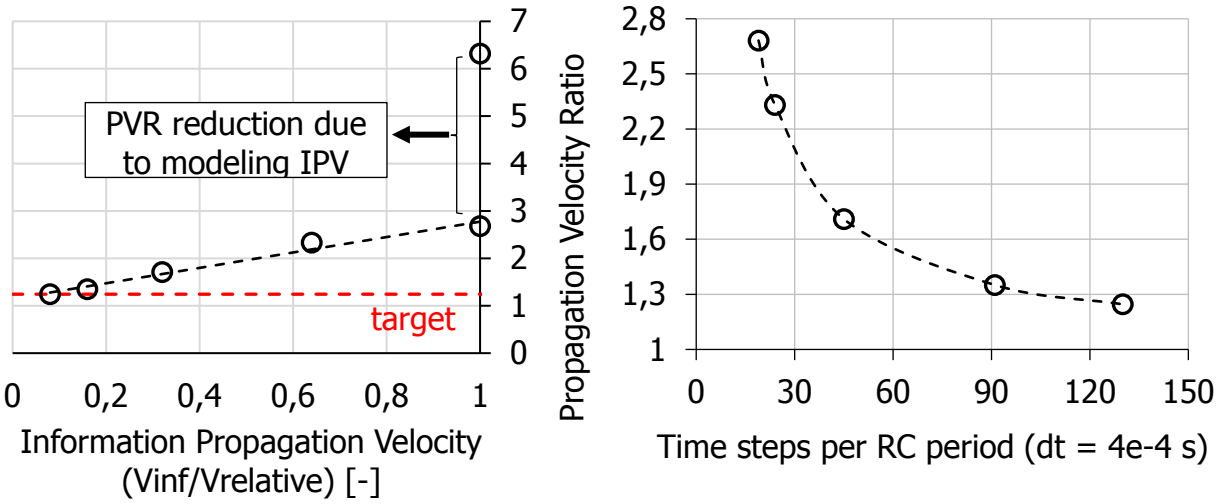

Figure 52 – IPV can be calibrated to capture the exact PVR, but the basic assumption is invalid

5.4. Model Implementation on 3D Geometries

Following the successful model validation for 2D cases, the blockage models were applied to 3D geometries. Strong secondary flow features of the publicly available PWA inducer made the extraction of the viscous model parameters challenging within the time frame given for the present thesis. Further 3D model validation is suggested for follow-up research. The challenges met during viscous parameter extraction are discussed in this Section.

5.4.1. Test Setup: The PWA (Rockwell) Inducer

The 3-bladed test inducer of the Pratt & Whitney Aircraft (PWA) Company was selected [114] because of its simple blade geometry. This is also referred to as the Rockwell inducer. The geometry features flat blades with a straight leading edge and circular leading edge profile. The blade angle and tip radius are constant along the chord, which is shown in Figure 53. The simple geometry yields strong secondary flow features that dominate the blade passage. Main parameters of the Rockwell inducer are highlighted in Table 4.

Table 4 – PWA inducer main technical parameters [114]

Design Rotational Speed	[RPM]	4900
Number of Blades	[#]	3
Tip Diameter	[m]	0.178
Tip-to-Root ratio	[-]	1.87-2.51
Blade Root Angle	[deg]	8(inlet)-10(exit)
Blade Tip Angle	[deg]	19.35-18.25
Blade Thickness to Tip ratio	[%]	1.85
Tip gap to Tip ratio	[%]	1.74
Design flow coefficient	[-]	0.073

The geometry of the PWA (Rockwell) inducer is given in the front and side views in Figure 53. The inducer domain in which momentum sources are applied is indicated with dashed lines. Flow displacement sources are applied on the blade surface.

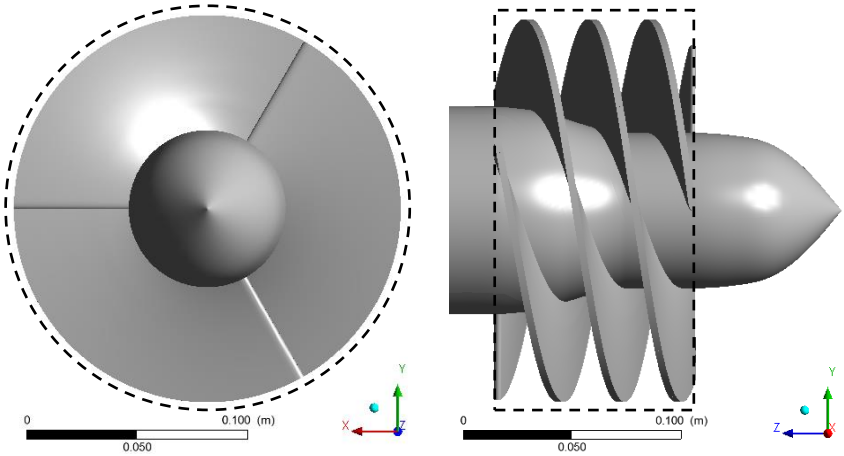

Figure 53 – PWA Inducer impeller geometry and the impeller fluid domain (dashed lines)

The computed viscous pressure characteristics (total-to-total pressure rise coefficient: ψ_{TT}) were validated against the original experimental data [114] with 1.74% (radius percentage) tip gap in Figure 54. Both the slope and values of the measured data were captured within 0.1% error over a wide range of flow coefficients using one-phase CFD (RANS with SST). Sorensen [98] reported simulation results of similar accuracy, using identical simulation setup for the 0.6% tip gap geometry.

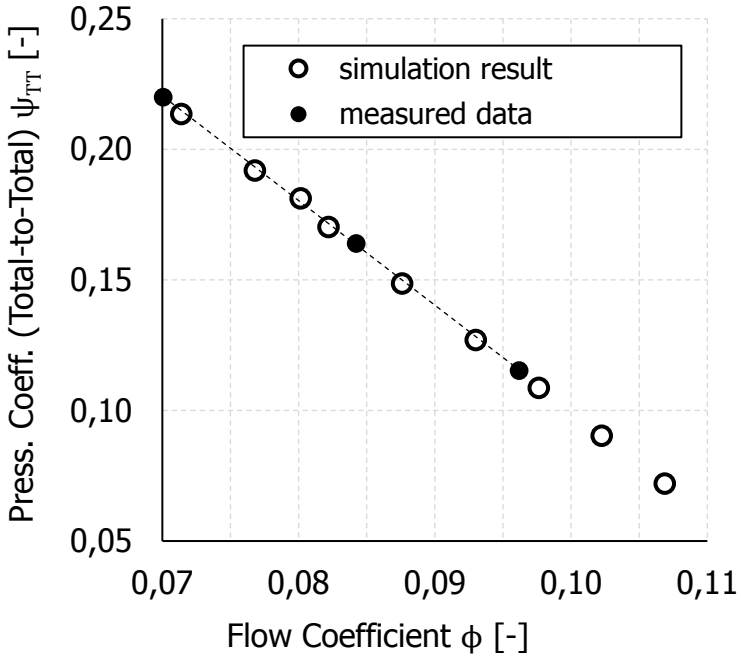

Figure 54 – PWA inducer viscous performance captured by 0.1% error in one-phase CFD [114]

The strong interference between the viscous blade and the secondary flow in the blade passage posed a challenge to the 3D implementation of the *Viscous Blockage Model*. This challenge originates from the pseudo-inviscid approximation of the inviscid flow, which is introduced in Section 5.1.2. Eventually, the selection of the flow solver (Ansys CFX) limited the ability of the current implementation to assess viscous blockage, which may be resolved by switching to an inviscid solver, or by creating an in-house code that solves the Euler equations.

The objective of one-phase viscous simulations of the PWA inducer, was to assess the viscous flow blockage at several flow coefficients (ϕ), to populate the *Viscous Blockage Model*. In 2D cases, this was done by assessing the change of momentum loss and flow displacement between viscous and inviscid results. For this, the inviscid pump characteristics need to be assessed, which can involve the inviscid assumption of the blade, the hub and shroud, or both in 3D inducers. Various pseudo-inviscid simulation setups are shown in Figure 55 (a, b and c), with their pressure characteristics reported in Figure 56. Figure 56 also reports the viscous characteristics from Figure 54 (data points e), and the blockage-based assessment of the inducer performance (data points d), which is currently limited by the challenges of 3D model implementation. The causes of the different pressure characteristics of the inviscid setups, and the 20% error of the blockage-based performance assessment are discussed next.

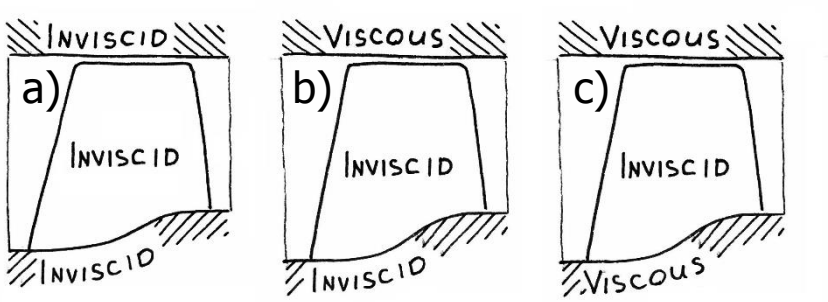

Figure 55 – Inviscid performance of the PWA inducer assessed by assuming inviscid condition on all walls (a), or viscous condition on the shroud (b), or on the hub as well (c)

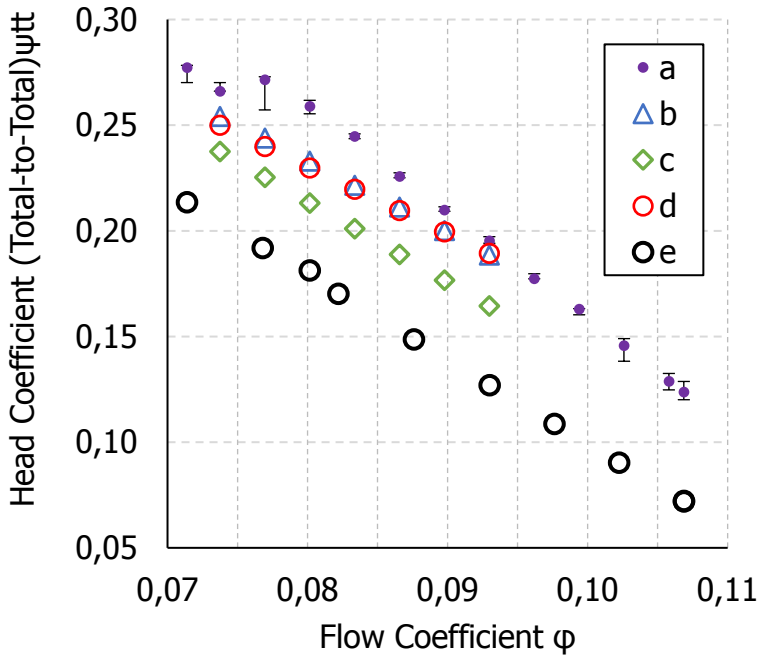

Figure 56 – Performance assessment of the PWA inducer illustrates losses due to secondary flow, and shows 20% error of the *Viscous Blockage Model* (d) under current implementation

When all solid surfaces are set up as free-slip walls (Figure 55a), and the fluid is treated as pseudo-inviscid continuum (due to the limitation of the Ansys CFX solver), the slope of the inviscid pressure characteristics is higher than that of the viscous pressure characteristics, which is in contrast with Greitzer [24]. The confusion is caused by the deterioration of key secondary flow features (backflow and horse-shoe vortices), which may be modeled by setting up the shroud (Figure 55b) and the hub (Figure 55c) as viscous walls. The corresponding pressure characteristics are reported with the markers Δ and ◊ in Figure 56, and the effects of these changes are discussed next.

First, the no-slip wall condition on the shroud dissipates the kinetic energy in the backflow, which acts as blockage and accelerates the freestream. This is shown in Figure 57, where the circumferentially averaged velocity field of Figure 55b is normalized with that of Figure 55a, at ϕ=0.93. The increased effective ϕ reduces the blade loading and contributes to pressure loss, which becomes more pronounced at low ϕ, where the backflow is at its strongest. This loss is visible in Figure 56, from the slope difference between the data with inviscid (a,●) and viscous (b,Δ) shrouds.

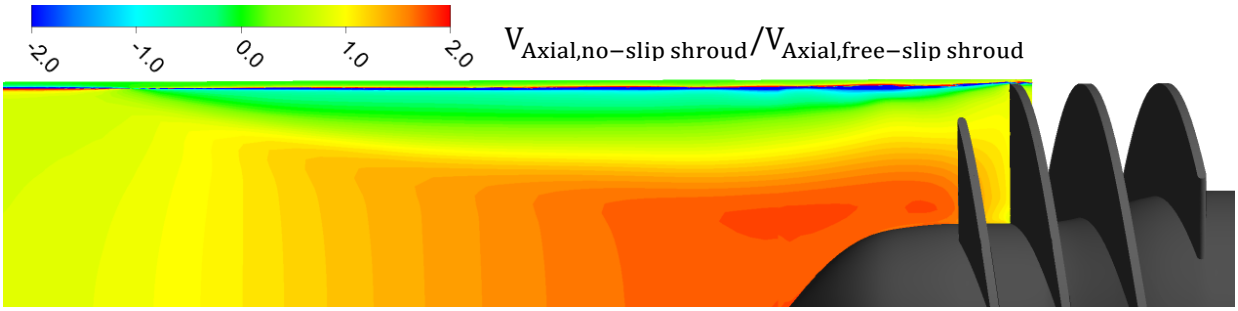

Figure 57 – Viscous shroud dissipates backflow momentum, its blockage accelerates freestream

Second, the viscous boundary layer at the hub contributes to the growth of horse-shoe vortices, which are shown in Figure 58. The figure displays the PWA inducer blade in axonometric views from the front (a) and back (b), which supports the visual assessment of vortices. The blade is colored by the normalized viscous losses at the surface, expressed in the parallel force (f_p), based on Eq. 31. Vortices are indicated in grey, as fluid surfaces of constant vorticity. The viscous dissipation of the rotational energy of these vortices contribute to mixing losses. The relative strength of root vortices is determined by the flow rate (ϕ). At high ϕ, the pressure-side vortex dominates the losses in the blade passage, which is visible in Figure 60, and is responsible for the slope difference between data b (Δ) and c (◊) in Figure 56.

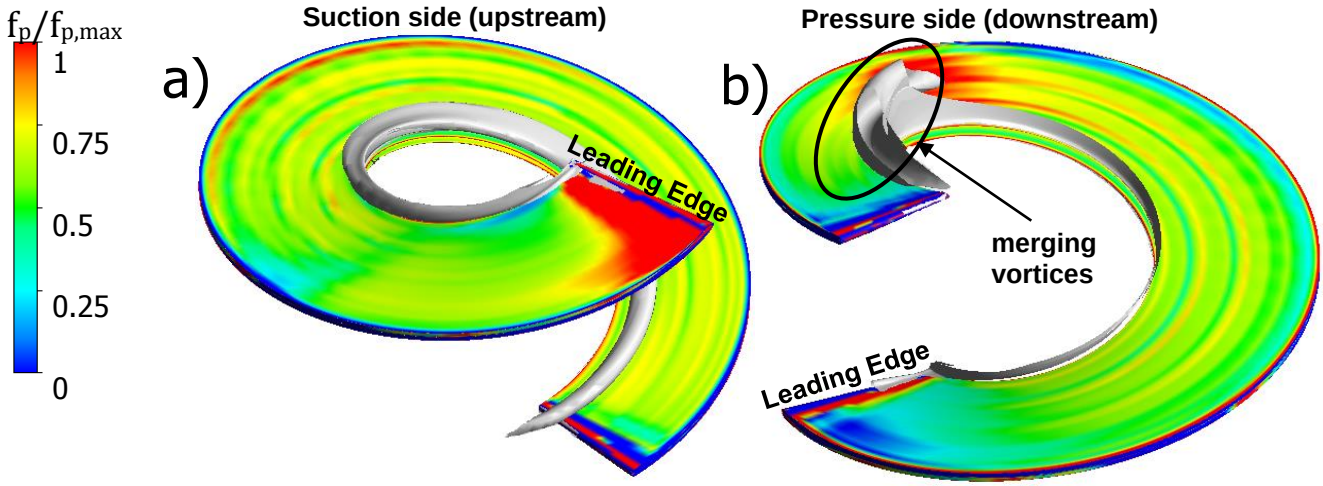

Figure 58 – Root vortices appear in the 3D inducer passage, vortex strength determined by ϕ

The plan-of-attack to extract viscous blockage due to the blades alone is shown in Figure 59. The underlying assumption is that the blade boundary layer has little effect on the strength of the secondary flows within the blade passage. This assumption allows for the indirect assessment of the viscous blockage, by using the difference of viscous losses between the setups depicted in Figure 59e and Figure 59c. The pressure characteristics of these setups are indicated with the markers **O** and ◊ in Figure 56. The analysis of the simulations indicated that the viscous loss due to the boundary layer is exceeded by the viscous losses caused by its amplifying effect on the secondary flows. This made the underlying assumption of Figure 59 invalid, and posed a challenge to the assessment of viscous blockage due to the blades. Because of this challenge, and the time constraint of the present thesis, full 3D validation of the *Viscous Blockage Model* was not achieved.

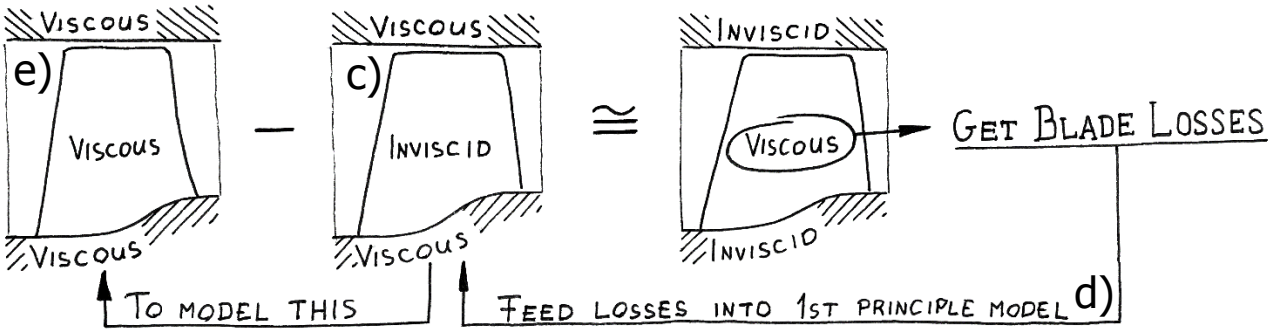

Figure 59 – Viscous blockage due to the blade boundary layer may be assessed indirectly from the difference of losses in the viscous (e) and inviscid (c) simulations

Despite the limitations of the low-interference assumption detailed above, the viscous blade losses were assessed based on the logic of Figure 59, with a solely demonstrative motive. When implemented in inviscid 3D simulations, the *Viscous Blockage Model* yielded 20-50% discrepancy in the pressure characteristics, which are shown with red markers (**o**) in Figure 56. These results highlight the need for better model implementation, which is possible through an inviscid fluid solver.

In the followings, the viscous losses, and the boundary layer thickness on the blades of the PWA inducer are discussed, which are the flow properties most critical to viscous blockage. For this demonstration, the simulation at $\Phi=0.093$ was selected, for its articulate secondary flow features.

5.4.2. Losses in the Rockwell Inducer Passage

The *Viscous Kinetic Energy Dissipation Model* is driven by viscous losses in the blade passage, which can be assessed through the parallel force (f_p, introduced in Eq. 31). The pitch-wise average of the parallel force is shown in the meridional view of the inducer blade passage in Figure 60. In the absence of thermal losses, because of the isothermal fluid assumption, the parallel force captures friction losses in the boundary layer, and mixing losses in the free shear layers. Based on the figure, the major contributors to viscous losses are identified, which is discussed next.

The adverse pressure gradient at the inducer inlet leads to the early turbulent transition of the boundary layer, which dominates the viscous losses in the initial 25% of the chord. At low flow coefficients, where the tip leakage flow develops into extensive backflow, the initial viscous losses are dramatically increased. This is due to the acceleration of the freestream (based on Figure 57), and its mixing with the backflow, which results in increased blade loading and consequent losses along the entire span. In the hub region, losses are dominated by turbulent mixing in the core of the vortices, which are shed from the leading edges of blades. These vortices are shown in Figure 58. The pressure-side vortex becomes considerably stronger than its suction-side counterpart at higher-than-design flow coefficients. At the tip at the mid-chord of the blade, the pressure difference between the two sides of the blade pivots, which results in reverse tip leakage flow, and the local acceleration of the fluid. Acceleration is captured by the negative values of the parallel force. The moderate viscous losses due to the boundary layer are only identifiable in the middle of the passage.

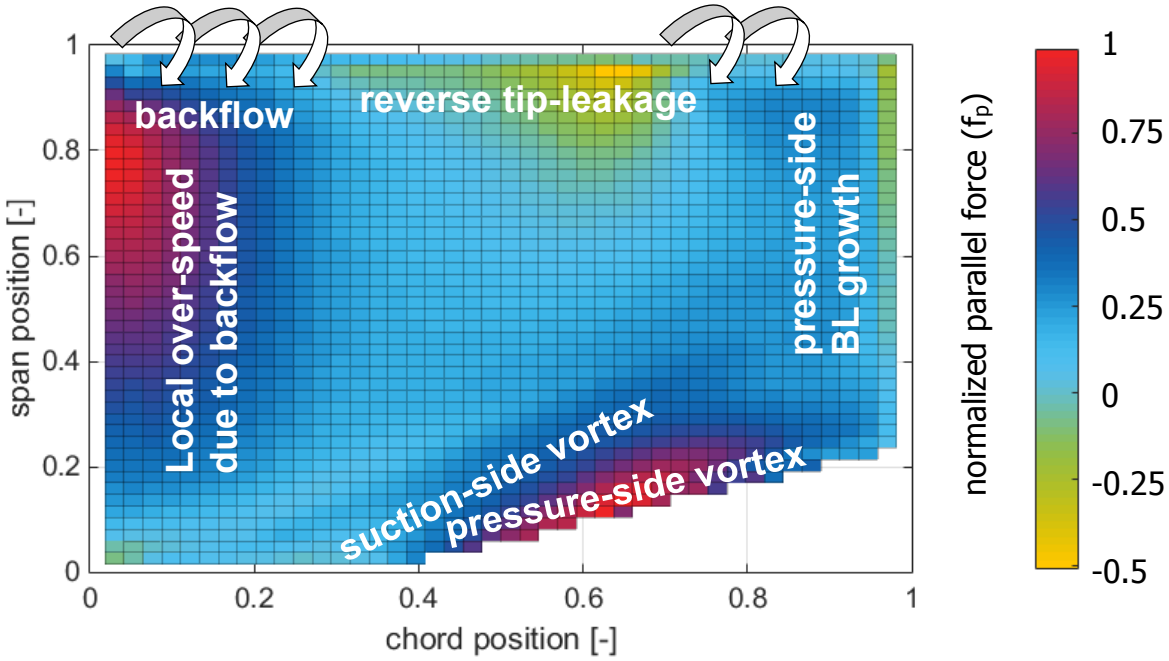

Figure 60 – Kinetic energy loss assessment on the PWA inducer shows dominant secondary losses near the hub, shroud, and the leading edge of the blade (ϕ = 0.093)

5.4.3. Boundary Layer Thickness in the Rockwell Inducer Passage

In the current implementation, the *Inviscid Stream Displacement Model* is driven by the semi-empirical boundary layer displacement data extracted from viscous simulations. The boundary layer thickness is also heavily affected by secondary flows, which is assessed in Figure 61, individually on the suction side (Figure 61a) and pressure side (Figure 61b) of the blade.

The suction-side boundary layer undergoes rapid growth in the first 25% of the chord, and continues to grow at a reduced pace as it enters the blade passage. The pressure-side boundary layer shows a steady initial growth. Secondary flow affects the boundary layer thickness through the horseshoe vortices at the hub, which wedge into the surrounding flow. The reinforced tip leakage flow due to the aft-loading of blades extracts flow from the pressure side, which is shown in Figure 61b. The resulting fresh suction-side boundary layer bulks up the boundary layer in the middle of the blade passage, which is shown in Figure 61a.

In conclusion, both the secondary flow losses, end wall losses and the friction losses in the blade boundary layer are coupled in the PWA (Rockwell) inducer, which presented challenges that were beyond the scope of the present work. To overcome these challenges, the use of both a different test geometry and fluid solver is recommended. The four-bladed MIT inducer is designed based on the SSME LPOP inducer [34], and has a better behaving flow field, with less dominant secondary flow, than the PWA inducer. The utilization of an inviscid flow solver (commercial, or in-house) may further reduce the computational cost, facilitate convergence of inviscid results at a wide range of flow coefficients, and ease the assessment of viscous blockage. Further recommendations are listed in Section 6.3.

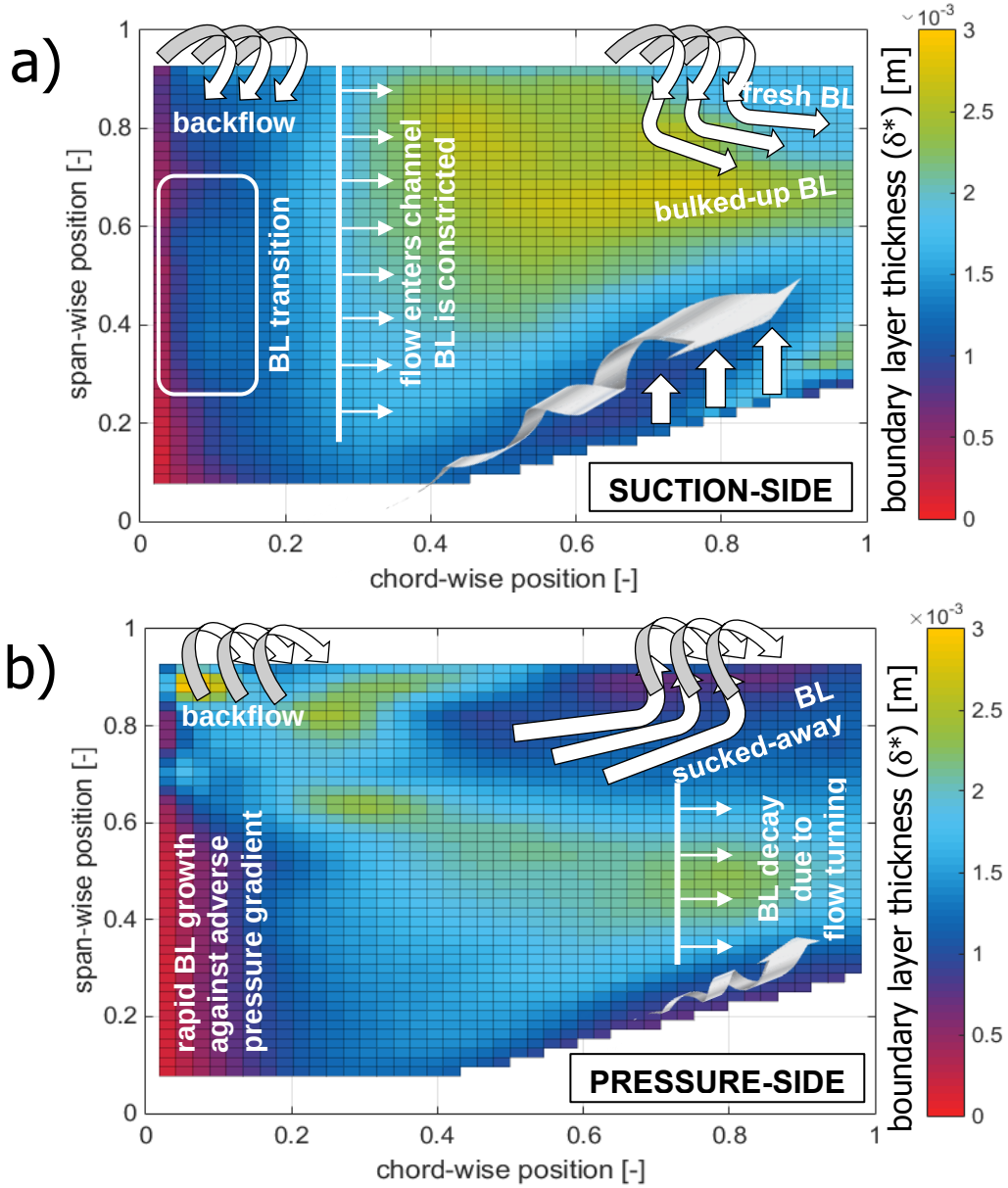

Figure 61 – Boundary layer thickness of the blade of the PWA inducer is affected by vortex formation at the root, and leakage flow at the tip (ϕ = 0.093)

6

Conclusions

6.1. Major Findings

In the present thesis we have devised and validated a source-term-based 2D numerical model to investigate *Rotating Cavitation* (RC) in rocket inducers. The devised method reduces the computational cost of calculations by an order of magnitude compared to high fidelity RC assessment methods. This is achieved by one-phase inviscid simulations on a coarse mesh, which eliminates the turbulence model, the energy equation, the equations of two-phase mass transfer and the volume fraction equation of previous computational RC assessment methods. The viscous blockage is captured by two models, one accounting for viscous friction and one for flow displacement. The models are linked to the local flow field via the local flow coefficient (ϕ). The viscous body force formulation is coupled with a *Cavity Blockage Model*, which mimics the cavity displacement of the blade passage flow with surface sources. The *Cavity Blockage Model* is derived from the response of cavity volumes to changes in flow rate (ϕ), which is expressed in the dynamic transfer function called *Mass Flow Gain Factor* (M). The model may be extended to capture cavity response to changes in cavitation number (σ), expressed in the *Cavitation Compliance* (K). In the current model, which is a proof of concept, the dynamic modeling of cavities is not implemented. The proposed method facilitates computationally affordable research of non-axisymmetric, viscous, two-phase flow instabilities of several types.

The combined *Viscous Blockage Models* capture the slope of viscous total-to-total pressure characteristics within 0.26% error in the NASA rotor 67 2D mid-span cascade. The *Cavity Blockage Model* consistently under-predicts the cavity extent around hydrofoils by 5%, which is especially notable at low σ. The discrepancy is due to the CFD implementation of the transpiration concept, which is limited by the surface curvature and blunt leading edge profile of hydrofoils, such as the NACA-0015. This limitation is alleviated in inducers, which feature flat blades and sharp leading edges. Even with the current implementation around hydrofoils, the model yields satisfactory accuracy for a proof of concept.

RC was captured in both viscous and inviscid two-phase simulations, matching the flow rate (ϕ) and cavitation number (σ) at which its onset was anticipated, based on experimental data. The viscous two-phase assessment indicated 14% higher frequency of RC than reported in the reference [100]. The forward-rotating self-sustained interaction cycle of RC was successfully captured in one-phase inviscid simulations, using only the steady *Cavity Blockage Model*. This corroborates the hypothesis that the contribution of viscous blockage to RC is marginal compared to that of cavity blockage. This observation cannot be generalized to 3D. The dynamic assessment of RC via the dynamic transfer functions K and M is beyond the reach of the present thesis, in which RC is captured through the instantaneous cavity response model. Without the dynamic modeling of the cavity displacement domain, the propagation velocity of RC is governed by the information propagation velocity in the liquid phase, and not the natural time rates of cavity dynamics. This results in an order of magnitude larger RC propagation velocities indicated by the *Cavity Blockage Model*, than what experiments suggest. Even though the propagation velocity is not controlled by the proposed cavity model, the identified forward propagating instability mechanism unmistakably corresponds to RC. This supports the hypothesis, that RC is a purely blockage-driven phenomenon.

Finally, the viscous models were scaled to 3D, and applied to a test inducer of simple geometry. The flow field of the selected inducer (PWA or Rockwell) is heavily affected by secondary flow features, which made the assessment of viscous friction losses and streamline displacement challenging. The key features of the flow field, and the components of the *Viscous Blockage Model* were nevertheless assessed. Blade losses were found to be marginal compared to secondary and end wall losses in the 3D inducer. The slope of viscous total-to-total pressure characteristics was captured within 1% error by setting up the hub and shroud as viscous walls, even without any viscous model implementation. A constant 20% error along the pump characteristics is likely attributed to the excess flow turning due to the lack of the boundary layer displacement, which has little dependency on the flow coefficient (ϕ).

6.2. Model Limitations

6.2.1. Assumptions of the Source-Term Based Models

The viscous *Kinetic Energy Dissipation Model* is derived for incompressible, isothermal fluids and adiabatic systems. Viscous heating and compressibility effects may be included in the parallel force model by using the formulation given by Peters (Eq. 27), instead of the one by Sorensen (Eq. 31). The streamline displacement models are applied to incompressible 2D fluid, but are not limited by these assumptions. The compressibility correction of the transpiration concept was included in the model derivation (together with its scaling to 3D), however, neither the compressible, nor the 3D capability was validated. Furthermore, transonic compressible application is not recommended, as no boundary-layer – shock-wave interaction was considered in the model derivation.

6.2.2. Limitations due to Current Implementation

At this early phase of model validation, loss and displacement data was extracted from two-phase and viscous simulations to populate the blockage model parameters. The generation of this semi-empirical dataset requires the capability to simulate steady state viscous and two-phase cavitating flows. The devised blockage models might be driven by analytical correlations in the future, which would result in the substantial decrease of the wall time of numerical RC assessment.

The current implementation of the cavity displacement extraction is based on streamline trajectories, which does not account for the initial flow turning around blunt leading edges. This leads to the necessary calibration of the cavity displacement model near the leading edge of hydrofoils. Furthermore, the tangential velocities of the displacement flow were approximated from free-stream values. This approximation loses validity near walls with substantial curvature, causing 5-10% relative error in the hydrofoil validation case. This discrepancy is acceptable in a proof of concept. The error is mitigated by the low curvature and sharp edge of inducer blades.

In the present thesis, the Ansys CFX 17.1 fluid solver was used for all CFD simulations. CFX solves the Navier-Stokes equations of momentum conservation, which is not practical for inviscid assessment, because the viscosity cannot be set to zero. This means, that the mathematical formulation supports the formation and shedding of leading-edge vortices. This unsteadiness limits the validity of inviscid model assessment to a narrow range of flow coefficients around the pump design condition, and poses a challenge to the assessment of viscous blockage in 3D inducers.

6.2.3. Limitations due to Time Constraint

So far, the blockage models have been validated for 2D cases. In the current implementation, the propagation velocity of RC is affected by the information propagation velocity in the liquid phase, because the time rates of cavity growth and collapse are not controlled by the model. The *Viscous Blockage Models* were applied to a 3D test inducer, but full model validity was not achieved, due to challenges posed by the complex internal flow and the inviscid implementation of the fluid solver.

6.3. Further Research

Future research should address the model limitations due to implementation choices, and further elaborate on concepts that for the time being could not be implemented. These are discussed first:

The level of empiricism of the *Cavity Blockage Model* shall be reduced by defining the cavity volume (V_c) analytically, as a function of the relative flow angle (β) and the flow coefficient (ϕ). A comprehensive study to define M and K in terms of non-dimensional pump parameters would ensure model applicability to several impeller geometries, without necessitating an empirical cavity database for every inducer setup. The time-accurate modeling of cavity volumes based on the dynamic transfer functions M and K would add control over the propagation velocity of RC to the cavity model, by which the RC assessment capability of the method would be whole. The dynamic transfer functions of the *Cavity Blockage Model* might be implemented in CFX using FORTRAN routines. User routines can assess time-step data otherwise not supported by the graphical user interface, which will help realize the computational advantage yielded by the blockage-based assessment of RC.

Regarding model limitations due to implementation choices, the *Cavity Blockage Model* and the numerical modeling of inviscid flow can be identified as directions for follow-up work. The error in the predicted cavity extent around hydrofoils might be improved by prescribing purely normal direction for mass output through the wall, when the walls act as sinks at the back-side of cavities. This would reduce the delay in capturing flow reattachment at the backside of the cavity, which becomes noticeable as the cavity extends over 60% of the chord in the hydrofoil validation case. Finally, in order to mitigate the leading edge vortex shedding in inviscid solutions and further reduce the computational cost, the use of a 2D Eulerian solver is recommended instead of the pseudo-inviscid approximation of CFX. Ansys Fluent can be set to solve the Euler equations on a 2D domain for instance. For further model validation on 3D inducers, the four-bladed MIT inducer developed by Lettieri et al. [51] is recommended over the PWA inducer (which was used in this study), for its better internal flow behavior and availability of abundant experimental and simulated data.

7

Appendix

A 1 Mesh sensitivity analyses

Mesh sensitivity analyses were conducted for each geometry and mesh configuration (Eulerian or with wall-refinement). In each cases, a mesh density at which relative error dropped below 0.1% was selected, which is indicated with a solid black marker in the following figures. Below are results of mesh sensitivity analysis for the NASA rotor 67 single-blade geometry (Figure A1), its 2D mid-span cascade (Figure A2) and the 2D cascade of Iga et al. (Figure A3).

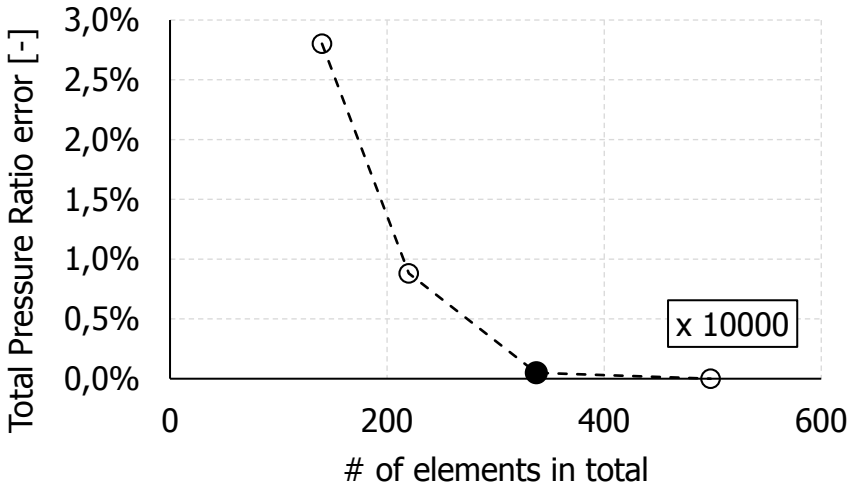

Figure A1– Total Pressure Ratio of the NASA rotor 67 3D single blade geometry

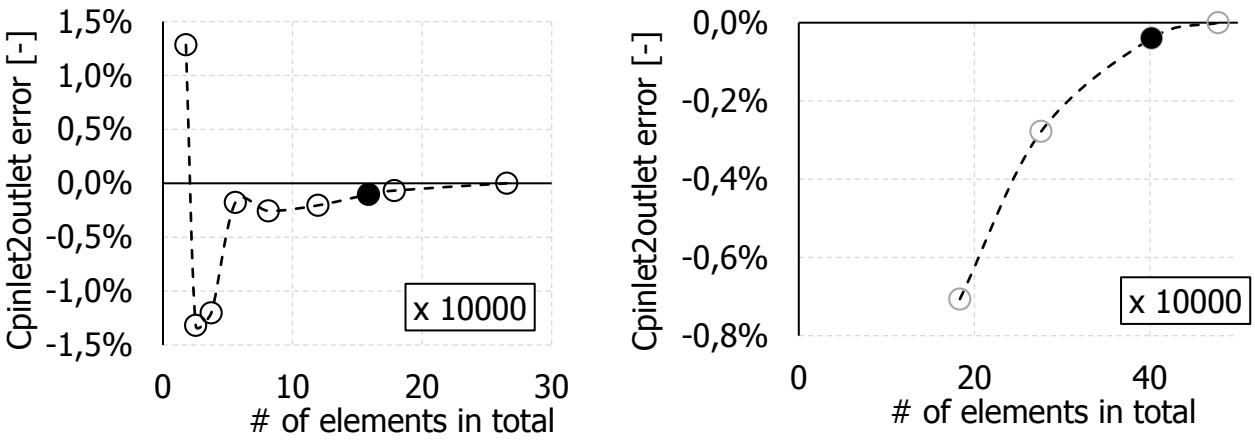

Figure A2- Pressure Coefficient of the NASA rotor 67 2D cascade, viscous & inviscid mesh

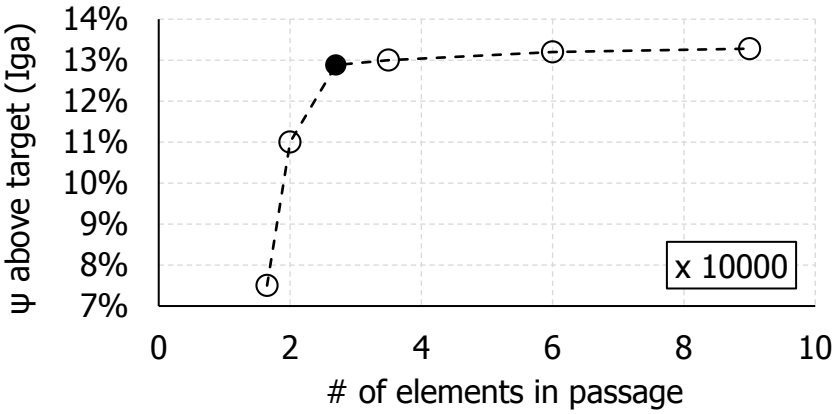

Figure A3 – Total Pressure Ratio of the 2D cascade of Iga et al. for β=5º (ϕ=.176)

A 2 Summary of Calculation Setup

The followings are general guidelines for simulation setup, which aim at facilitating further research in the field. The fellow researcher who will continue the project is encouraged to read through the following considerations and advices.

Pre-Processor

The physics of a CFD simulation is set up in the pre-processor. The User needs to define a discretized (meshed) geometry that represents the flow domain of the experimental setup, set the physics of the solver and the boundary conditions, and in some cases provide the initial flow conditions of the simulation. These steps should fully characterize a mesh-independent solution, and are further explored below.

The fluid domain of complex numerical problems (for which analytical solution is unattainable) must be split into smaller subdomains, which are more approachable by the partial differential equations that govern fluid flow and heat transfer. The *Geometry* of turbomachines can be designed in the parametric blade modeler of Ansys, called BladeGen. BladeGen cannot model 2D geometries, but they can be approximated by setting the impeller radius to large values, thus reducing the domain curvature. Subsequently, the number of blades need to be increased to preserve blade pitch. Note, that BladeGen requires at least three span-wise profiles to create the blade geometry. In case of a one-cell-wide quasi-prismatic domain, the center profile can be manually deleted in the geometry output file, to reduce the computational overhead by 50%. Alternatively for simple geometries, such as the NACA-0015 hydrofoil test cases presented in this thesis, Ansys ICEM might be used to generate structured hexahedral mesh. This environment requires a substantial amount of manual labor to set up the fluid domain and mesh at once, but the GUI actions can be recorded into scripted sessions from which iterations on the geometry can be generated with relative ease. Flat blade cascades might be generated in ICEM by assigning different materials to neighboring blade channels before blocking.

The process of geometrical discretization is called *Mesh Generation* (or Grid Generation), and it requires some expertise. Automatic mesh generators, such as TurboGrid may help provide high-quality structured mesh for turbomachinery applications. TurboGrid is compatible with BladeGen. In general, the mesh needs to be as coarse as possible, while conforming to general quality standards, to ensure optimal performance of the solver. The independence of the solution on the mesh quality should always be checked by reaching convergence on different discretization sizes and comparing the results. In general, a deviation of 0.1% from the asymptotic value is accepted. If the condition is not fulfilled, the mesh size must be increased by 50%, and checked again. This is done in Appendix

A1 in the present thesis. The most important quality checks of a mesh are aspect ratio, skewness, expansion ratio and the size of the first cell near viscous walls, expressed in the non-dimensional wall distance: y+. This value is critical to solving the viscous boundary layer, and it should be kept around 1 for SST applications. As a rule of thumb, expansion ratio in the wall refinement domain should be kept at a maximum of 1.2, which results in a minimum of 35 cells across the boundary layer domain.

Boundary Conditions (BC) refer to the prescribed properties of fluids on the inlet, outlet or opening interfaces, the expected behavior of fluids next to walls, and across fluid interfaces. BCs should always be chosen to provide acceptable control over the critical simulation parameters, and fully characterize the solution. For instance, prescribing mass flow at the outlet of a nearly choked transonic fan might result in wildly different pressure fields within the numerical uncertainty of the BC, providing little control over the results, and bad convergence. These cases can be set up with total pressure at the inlet and static pressure at the outlet, which is a robust combination of BCs. As a rule of thumb, BCs should provide enough information for the solver to calculate the internal energy, velocity- and pressure fields of the domain. Total pressure & mass flow or total pressure & static pressure are robust combinations to be defined at the inlet and outlet. BCs should always be defined with an understanding of the physics of the setup, possibly with the feasibility concerns of a wind-tunnel experiment in mind. Walls might be set to no-slip for solving the boundary layer or free-slip for assuming inviscid walls, which do not require mesh refinement. Additional BCs are those of internal fluid interfaces, which might be symmetry, cyclic, rotating or general connection. The latter two may connect adjacent fluid domains defined in separate geometries. Cyclic wall conditions allow the user to simulate only one blade channel of axisymmetric cases, by linking the flow at the two cyclic sides of the domain. Symmetry condition is generally useful to define parallel flow on a surface without defining it as wall. This BC might be defined on the top and bottom of 2D domains.

Finally, *Initial Conditions* are necessary to initiate the two-phase solver. First, the initial volume fractions need to be prescribed at the entire fluid domain, which is usually $\varphi_v=0$ & $\varphi_l=1$ uniformly. Second, the two-phase solver must be initiated from a fully converged one-phase pressure field for the solver to converge. This is because the Rayleigh-Plesset equations (and its formulation by Zwart, used by CFX [90]) treat the fluid as an interpenetrating continua of two phases. During the initial convergence of the flow field, local pressure minimums may induce non-physical cavitation in the free-stream, and around velocity boundaries, which the solver cannot find its way back from. Therefore, an initial solution needs to be attained in all cases, with both fluid phases present in the solution, but with the cavitation model switched off, and φ_v set to a uniform 0.

Solver

The *Solver* may be initiated from Ansys Workbench, from the pre-processor, or from the command window through the cfd5 command. Matlab may also communicate with the pre-processor, solver and post-processor through the cfd5 environment. Matlab macros around CFX may be used to set up several cases in succession, process simulation results, and even externalize the optimization engine. In some cases, when the solver or interpolator faces memory shortage, increased memory allocation (by 20%) might solve the problem.

The Solver might solve the fully inviscid Euler equations, or the Navier-Stokes (N-S) equations of momentum conservation. Accompanying the momentum equation, the continuity equation, and in some cases the energy equation (1 eq.), the equations of two-phase mass transfer (2 eq.) and volume fractions (1 eq.), and the equations of a turbulence model (2 eq.) might be required. CFX solves the N-S equations, which poses a challenge to assessing inviscid flows. Namely, the non-zero viscosity supports velocity curl and hence vortex formation in the domain, which will subsequently shed from the leading edges of blades even at relatively small flow angles, preventing the solution from reaching convergence. Inviscid solutions of small flow angles may be approximated by setting low viscosity, inviscid wall conditions, and selecting the laminar turbulence model. The turbulence model encompasses the set of equations that solve the Reynolds stresses in a Reynold Averaged Navier-Stokes (RANS) simulation. In general, the SST model is recommended for turbomachinery applications, which provides a combination of the k-ω and k-ε models, detailed in Section 3.1.2 of the present thesis. The energy equation is needed when heat transfer is modeled either by external heat sources, or by internal heating due to viscous friction in high-velocity compressible fluids. In case of liquid fluid simulations, and what concerns *Rotating Cavitation* (RC), an incompressible, isothermal fluid approximation yields valid results. Such simulations require uniform fluid temperature to interpolate constant fluid properties from, and no energy equation.

Modeling RC requires transient simulations. In the present thesis, setting 10 time steps per blade passing was found to yield time-step independent results, which on the 2D cascade of Iga [100] means a time step of 0.0004 s. Time step data may be saved at every step for demonstrative purposes, such as video compiling, for creating time plots, or for assessing the propagation velocity of traveling instabilities, but it dramatically increases the required memory and wall time of the simulations. Time-plots are also available in the solver manager, provided that the user defined the appropriate monitor objects in the pre-processor. Time-step independence should also be checked.

It is advisable to use custom monitor points to monitor solution convergence, as equation residuals are not always the best indicators of convergence. For example, at turbulent cases, or where separation is present in the solution, the residuals flatten out, while the solution still converges. Monitor statistics may also be used to assess simple time-step data. Monitor statistics can access the minimum value of an arbitrary set of time step data at monitor objects. This data needs to be made monotone through the monitored expression, to make sure that the minimum value corresponds to the minimum time step. This can be achieved by multiplying the monitored

expression with timeStep*10^x, where x may be selected to yield monotone data. This allows the user to circumvent the necessity of using user FORTRAN in simple cases, which require access to data from previous time steps. In more complex cases, the monitor approach may induce cyclic dependence of variables, and the use of FORTRAN is unavoidable.

Post-Processor

The use of macros written in Matlab proved to be especially useful during post-procession. Both states and post-processing sessions can be saved into easily intelligible text files. These can be modified either manually, or by an appropriately written code in a loop to assess several cases with minimum repetitive manual labor. Boundary layer thickness cannot be directly extracted from CFX. The velocity profiles may be extracted from lines normal to the blade surface at several locations along the chord. Automation of the line assignment and data extraction might significantly reduce the overhead of post-procession. Boundary layer thickness was taken at locations, where the tangential velocity approached 99% of the free-stream value. Assessing the extent of the cavity domain is considerably easier. It was found, that the fluid surface of 25% vapor volume fraction ($\varphi_v=0.25$) best coalesced with the cavity-induced discontinuities in the velocity field. In the present thesis, the trajectory of the first streamline adjacent to the cavity volume was used to drive the *Cavity Blockage Model*. The streamline trajectory captures the profile of the cavity displacement, the recirculating domain behind it, and the viscous displacement of the reattached flow. On the flip side, streamline data does not correct for the initial flow turning at the leading edge of blunt-edge blades, which may necessitate model calibration in the initial 10% of the chord.

Bibliography

[1] NASA, "Prevention of Coupled Structure Propulsion Instability (POGO)," NASA SP-8055, 1970.

[2] Kamijo, K., Yoshida, M. and Tsujimoto, Y., "Hydraulic and mechanical performance of LE-7 LOX pump inducer," *Journal of Propulsion and Power,* vol. 9(6), pp. 819-826, 1993.

[3] Zoladz, T., "Overview of Rotating Cavitation and Cavitation Surge in the Fastrac Engine LOX Turbopump," NASA Marshall Space, Huntsville, Alabama, 2001.

[4] Ryan, R., "The Space Shuttle Main Engine Liquid Oxygen Pump High-Synchronous Vibration Issue: The Problem, The Resolution Approach, The Solution," in *In Proceedings of the 30th AIAA Joint Propulsion Conference*, 1994.

[5] A. Arnone, P. Boncinelli, A. Capuani, E. Spano and C. Rebattet, ""Ariane 5" TPLOX Inducer Design Strategies to Enhance Cavitating Performance," in *Caltech Conference Repository*, http://caltechconf.library.caltech.edu/127/1/cav2001_b7.004_n.pdf (accessed: 14/03/2017), 2001.

[6] Kamijo, K., Tamada, H. and Sakazume, N., "Development History of Liquid Oxygen Turbopump for the LE-7 Engine," in *36th AIAA Joint Propulsion Conference*, 2000.

[7] Reynolds, O., "The causes of the racing of the engines of screw steamers investigated theoretically and by experiment," *Trans. Inst. Naval Arch.,* vol. 14, pp. 56-67, 1873.

[8] Parsons (Sir), A. P., Writer, *The steam turbine on land and at sea.* [Performance]. Lecture to the Royal Institution, London, 1906.

[9] Rayleigh, L., "VIII. On the pressure developed in a liquid during the collapse of a spherical cavity," *Philosophical Magazine Series,* Vols. 6, 34(200), pp. 94-98, 1917.

[10] T. G. Leighton, "Derivation of the Rayleigh-Plesset Eguation in Terms of Volume," ISVR Technical Report No 308, January 2007.

[11] Guinard, P., Fuller, T. and Acosta, A. J., "An experimental study of axial flow pump cavitation," Hydrodynamics Laboratory California Institute of Technology, Pasadena, California, Report No. E-19.3, 1953.

[12] Acosta, A. J., "An experimental study on cavitating inducers," in *Second Symposium on Naval Hydrodynamics, Hydrodynamic Noise, Cavity Flow*, August 25-29, Washington, D.C., 1958.

[13] Acosta, A. J. and Hollander, A., "Remarks on cavitation in turbomachines," Engineering Division, California Institute of Technology, Pasadena, California, Report No. 79.3, 1959.

[14] Stripling, L. and Acosta, A., "Cavitation in Turbopumps - Part 1," *Journal Of Basic Engineering,* vol. 84(3), p. 326, 1962.

[15] Knapp, R. T. and Hollander, A., "Laboratory Investigations of the Mechanism of Cavitation," in *Transactions of the ASME for July, 1948*, Pasadena, California, 1948.

[16] Ruggeri, R., S. and Moore, R., D., "Method for Prediction of Pump Cavitation Performance for Various Liquids, Liquid Temperatures, and Rotative Speeds," Lewis Research Center, NASA, Cleveland, Ohio, 1969.

[17] Plesset, M. S., "Bubble Dynamics and Cavitation," *Annual Review of Fluid Mechanics,* vol. 9, pp. 145-185, 1977.

[18] Plesset, M. S., "The dynamics of cavitation bubbles," *Journal of Applied Mechanics,* 1949.

[19] Brennen, C., Cavitation and bubble dynamics, New York: Oxford University Press, 1995.

[20] Brennen, C., Fundamentals of multiphase flow, Cambridge [England]: Cambridge University Press, 2005.

[21] Dixon, S., L., Fluid Mechanics and Thermodynamics of Turbomachinery, Oxford, UK: Elsevier Butterworth–Heinemann, Fifth Edition, in SI/Metric units, 1998.

[22] Horiguchi, H., Watanabe, S. and Tsujimoto, Y., "Theoretical Analysis of Cavitation in Inducers With Unequal Blades With Alternate Leading Edge Cutback: Part I—Analytical Methods and the Results for Smaller Amount of Cutback," *Journal Of Fluids Engineering,* vol. 122(2), p. 412, 2000.

[23] Brennen, C., Hydrodynamics of pumps, Cambridge: Cambridge University Press, 2011.

[24] Greitzer, E., "The Stability of Pumping Systems - The 1980 Freeman Scholar Lecture," *Journal Of Fluids Engineering,* vol. 103(2), p. 193, 1981.

[25] Betchov, R. and Criminale, W. O., Stability of Parallel Flows, 1967.

[26] Tsujimoto, Y., Kamijo, K. and Brennen, C., "Unified Treatment of Flow Instabilities of Turbomachines," *Journal Of Propulsion And Power,* vol. 17(3), pp. 636-643, 2001.

[27] Wade, R. and Acosta, A., "Experimental Observations on the Flow Past a Plano-Convex Hydrofoil," *Journal Of Basic Engineering,* vol. 88(1), p. 273, 1966.

[28] Wade, R. and Acosta, A., "Investigation of Cavitating Cascades," *Journal Of Basic Engineering,* vol. 89(4), p. 693, 1967.

[29] Brennen, C. and Acosta, J., "A Note on Turbopump Blade Cavitation Compliance for the POGO Instability," 1973.

[30] Brennen, C. and Acosta, A., "Theoretical, quasi-static analysis of cavitation compliance in turbopumps," *Journal Of Spacecraft And Rockets,* vol. 10(3), pp. 175-180, 1973.

[31] Brennen, C. and Acosta, A., "The Dynamic Transfer Function for a Cavitating Inducer," *Journal Of Fluids Engineering,* vol. 98(2), p. 182, 1976.

[32] NASA, "Liquid Rocket Engine Turbopump Inducers," NASA SP-8052, 1971.

[33] Sutton, G. P. and Biblarz, O., Rocket Propulsion Elements, Seventh Edition, Wiey-Interscience, ISBN 0-471-32642-9, 2001.

[34] Tsujimoto, Y., Yoshida, Y., Maekawa, Y., Watanabe, S. and Hashimoto, T., "Observations of Oscillating Cavitation of an Inducer," *Journal Of Fluids Engineering,* vol. 119(4), p. 775, 1997.

[35] Rubin, S., "Longitudinal instability of liquid rockets due to propulsion feedback /POGO/," *Journal Of Spacecraft And Rockets,* vol. 3(8), pp. 1188-1195, 1966.

[36] Kamijo, K., Shimura, T. and Watanabe, M., "An Experimental investigation of Cavitating Inducer Instability," *ASME,* pp. Paper 77-WA/FW-14, 1977.

[37] Tsujimoto, Y., Kamijo, K. and Yoshida, Y., "A Theoretical Analysis of Rotating Cavitation in Inducers," *Journal Of Fluids Engineering,* vol. 115(1), p. 135, 1993.

[38] Tsujimoto, Y. and Murata, S., "Three Dimensional Unsteady Actuator Disk Theory for Subsonic Viscous Flow," *ZAMM - Zeitschrift Für Angewandte Mathematik Und Mechanik,* vol. 58(12), pp. 561-569, 1978.

[39] C. E. Brennen, C. Meissner, E. Y. Lo and G. S. Hoffman, "Scale Effects in the Dynamic Transfer Functions for Cavitating Inducers," *Journal of Fluids Engineering,* vol. Vol. 104, pp. 428-433, 1982.

[40] Watanabe, S., Tsujimoto, Y., Kamijo, K. and Furuya, O., "An analysis of unsteady cavitation characteristics by a singularity method," *Transactions Of The Japan Society Of Mechanical Engineers Series B,* vol. 64(621), pp. 1285-1292, 1998.

[41] Otsuka, S., Tsujimoto, Y., Kamijo, K. and Furuya, O., "Frequency Dependence of Mass Flow Gain Factor and Cavitation Compliance of Cavitating Inducers," *Journal Of Fluids Engineering,* vol. 118(2), p. 400, 1996.

[42] Wade, R., "Linearized theory of a partially cavitating cascade of flat plate hydrofoils," *Appl. Sci. Res.,* vol. 17(3), pp. 169-188, 1967.

[43] Furuya, O., "Dynamic Characteristics of Cavitating Pumps and Inducers," *ASME paper,* pp. 147-155, 1982.

[44] Watanabe, S., Sato, K., Tsujimoto, Y. and Kamijo, K, "Analysis of Rotating Cavitation in a Finite Pitch Cascade Using a Closed Cavity Model and a Singularity Method," *Journal Of Fluids Engineering,* vol. 121(4), p. 834, 1999.

[45] Horiguchi, H., Watanabe, S. and Tsujimoto, Y., "A Theoretical Analysis of Alternate Blade Cavitation in Inducers," *ASME,* vol. 122, pp. 156-163, 2000.

[46] Horiguchi, H., Watanabe, S. and Tsujimoto, Y., "A Linear Stability Analysis of Cavitation in a Finite Blade Count Impeller," *Journal Of Fluids Engineering,* vol. 122(4), p. 798, 2000.

[47] Hosangadi, A., Ahuja, V. and Ungewitter, R. J., "Simulations of Rotational Cavitation Instabilities in the SSME LPFP Inducer," in *43rd AIAA/ASME/SAE/ASEE Joint Propulsion Conference & Exhibit 8-11 July 2007*, Cincinnati, OH, 2007.

[48] Tani, N., Yamanishi, N. and Tsujimoto, Y., "Influence of Flow Coefficient and Flow Structure on Rotational Cavitation in Inducer," *Journal Of Fluids Engineering,* vol. 134(2), p. 021302, 2012.

[49] Kimura, T., Yoshida, Y., Hashimoto, T. and Shimagaki, M., "Numerical Simulation for Vortex Structure in a Turbopump Inducer: Close Relationship With Appearance of Cavitation Instabilities," *Journal Of Fluids Engineering,* vol. 130(5), p. 051104, 2008.

[50] Kang, D., Yonezawa, K., Horiguchi, H., Kawata, Y. and Tsujimoto, Y., "Cause of cavitation instabilities in three-dimensional inducer," *International Journal Of Fluid Machinery And Systems,* vol. 2(3), pp. 206-214, 2009.

[51] Lettieri, C. and Spakovszky, Z., "Mechanism of Rotating Cavitation in Four Bladed Rocket Turbopump Inducers (under revision)," 2016.

[52] Hashimoto, T., Yoshida, M. and Watanabe, M., "Experimental Study on Rotating Cavitation of Rocket Propellant Pump Inducers," *Journal Of Propulsion And Power,* vol. 13(4), pp. 488-494, 1997.

[53] Torre, L., Pasini, A., Cervone, A., Pace, G., Miloro, P. and D'Agostino, L., "Effect of Tip Clearance on the Performance of a Three-Bladed Axial Inducer," *Journal Of Propulsion And Power,* vol. 27(4), pp. 890-898, 2011.

[54] Greitzer, E., Tan, C. and Graf, M., Internal flow, Cambridge, U.K.: Cambridge University Press, 2004.

[55] Yokota, K., Mitsuda, K., Tsujimoto, Y. and Kato, C., "A Study of Vortex Structure in the Shear Layer between Main Flow and Swirling Backflow," *JSME International Journal Series B,* vol. 47(3), pp. 541-548, 2004.

[56] Yokota, K., Kurahara, K., Kataoka, D., Tsujimoto, Y. and J.Acosta, A., "A Study of Swirling Backflow and Vortex Structure at the Inlet of an Inducer," *JSME International Journal Series B,* vol. 42(3), pp. 451-459, 1999.

[57] Kang, D., Watanabe, T., Yonezawa, K., Horiguchi, H., Kawata, Y. and Tsujimoto, Y., "Inducer Design to avoid cavitation instabilities," *International Journal Of Fluid Machinery And Systems,* vol. 2(4), pp. 439-448, 2009.

[58] Yamanishi, N., Fukao, S., Qiao, X., Kato, C. and Tsujimoto, Y., "LES Simulation of Backflow Vortex Structure at the Inlet of an Inducer," *Journal Of Fluids Engineering,* vol. 129(5), p. 587, 2007.

[59] Yamamoto, K. and Tsujimoto, Y., "Backflow vortex cavitation and its effects on cavitation instabilities," *International Journal Of Fluid Machinery And Systems,* vol. 2(1), pp. 40-54, 2009.

[60] Qiao, X., Horiguchi, H. and Tsujimoto, Y., "Response of Backflow to Flow Rate Fluctuations," *Journal Of Fluids Engineering,* vol. 129(3), p. 350, 2007.

[61] Higashi, S., Yoshida, Y. and Tsujimoto, Y., "Tip Leakage Vortex Cavitation from the Tip Clearance of a Single Hydrofoil," *JSME International Journal Series B,* vol. 45(3), pp. 662-671, 2002.

[62] Torre, L., Pasini, A., Cervone, A. and d'Agostino, L., "Experimental performance of a tapered axial inducer: comparison with analytcal predictions," ALTA S.p.A., Via Gherardesca, 5 - 56121 Ospedaletto, Pisa, Italy, 2009.

[63] Cervone, A., Torre, L., Pasini, A. and d'Agostino, L., "Cavitation and Flow Instabilities in a 3-Bladed Axial Inducer Designed by Means of a Reduced Order Analytical Model," in *Proceedings of the 7th International Symposium on Cavitation, August 17-22, 2009*, Ann Harbor, Michigan, USA, 2009.

[64] d'Agostino, L., Torre, L., Pasini, A., Baccarella, D., Cervone, A. and Milani, A., "A Reduced Order Model for Preliminary Design and Performance Prediction of Tapered Inducers," in *44th AIAA/ASME/SAE/ASEE Joint Propulsion Conference & Exhibit, 21-23 July 2008*, Hartford, CT, 2008.

[65] Torre, L., Pasini, A., Cervone, A. and d'Agostino, L., "Experimental Characterization of the Rotordynamic Forces on Space Rocket Axial Inducers," *Journal Of Fluids Engineering,* vol. 133(10), p. 101102, 2011.

[66] Torre, L., Cervone, A., Pasini, A. and d'Agostino, L., "Experimental Characterization of Thermal Cavitation Effects on Space Rocket Axial Inducers," *Journal Of Fluids Engineering,* vol. 133(11), p. 111303, 2011.

[67] Pasini, A., Torre, L., Cervone, A. and d'Agostino, L., "Continuous Spectrum of the Rotordynamic Forces on a Four Bladed Inducer," *Journal Of Fluids Engineering,* vol. 133(12), p. 121101, 2011.

[68] Murayama, M., Yoshida, Y. and Tsujimoto, Y., "Unsteady Tip Leakage Vortex Cavitation Originating From the Tip Clearance of an Oscillating Hydrofoil," *Journal Of Fluids Engineering,* vol. 128(3), p. 421, 2006.

[69] Acosta, A., Tsujimoto, Y., Yoshida, Y., Azuma, S. and Cooper, P., "Effects of Leading Edge Sweep on the Cavitating Characteristics of Inducer Pumps," *International Journal Of Rotating Machinery,* vol. 7(6), pp. 397-404, 2001.

[70] Kang, D., Cervone, A., Yonezawa, K., Horiguchi, H., Kawata, Y. and Tsujimoto, Y., "Effect of blade geometry on tip leakage vortex of inducer," in *The 9th Asian International Conference on Fluid Machinery October 16-19, 2007*, Jeju, Korea, 2007.

[71] Horiguchi, H., Semenov, Y., Nakano, M. and Tsujimoto, Y., "Linear Stability Analysis of the Effects of Camber and Blade Thickness on Cavitation Instabilities in Inducers," *Journal Of Fluids Engineering,* vol. 128(3), p. 430, 2006.

[72] Furuya, O. and Acosta, A., "A Note on the Calculation of Supercavitating Hydrofoils With Rounded Noses," *Journal Of Fluids Engineering,* vol. 95(2), p. 221, 1973.

[73] Horiguchi, H., Watanabe, S. and Tsujimoto, Y., "Theoretical Analysis of Cavitation in Inducers With Unequal Blades With Alternate Leading Edge Cutback: Part II—Effects of the Amount of Cutback," *Journal Of Fluids Engineering,* vol. 122(2), p. 419, 2000.

[74] Yoshida, Y., Tsujimoto, Y., Kataoka, D., Horiguchi, H. and Wahl, F., "Effects of Alternate Leading Edge Cutback on Unsteady Cavitation in 4-Bladed Inducers," *Journal Of Fluids Engineering,* vol. 123(4), p. 762, 2001.

[75] Yang, W., Xiao, R., Wang, F. and Wu, Y., "Influence of Splitter Blades on the Cavitation Performance of a Double Suction Centrifugal Pump," *Advances In Mechanical Engineering,* vol. 6(0), pp. 963197-963197, 2015.

[76] Onoue, J., Okamoto, A., Hayakawa, M. and Kawata, Y., "Improvement of suction performance of general industrial centrifugal pump," *The 13th Asian International Conference on Fluid Machinery,* 2015.

[77] Shimiya, N., Fujii, A., Horiguchi, H., Uchiumi, M., Kurokawa, J. and Tsujimoto, Y., "Suppression of Cavitation Instabilities in an Inducer by J Groove," *Journal Of Fluids Engineering,* vol. 130(2), p. 021302, 2008.

[78] Fujii, A., Mizuno, S., Horiguchi, H. and Tsujimoto, Y., "Suppression of Cavitation Instabilities by Jet Injection at Inducer Inlet," in *ASME Fluids Engineering Division Summer Meeting and Exhibition June 19-23, 2005*, Houston, TX, USA, 2005.

[79] Tan, L., Zhu, B., Cao, S., Wang, Y. and Wang, B., "Influence of Prewhirl Regulation by Inlet Guide Vanes on Cavitation Performance of a Centrifugal Pump," *Energies,* vol. 7(2), pp. 1050-1065, 2014.

[80] Xu, L., "Assessing Viscous Body Forces for Unsteady Calculations," *Journual of Turbomachinery,* vol. 125(3), pp. 425-432, 2003.

[81] Brennen, C., "A Review of the Dynamics of Cavitating Pumps," *Journal Of Fluids Engineering,* vol. 135(6), p. 061301, 2013.

[82] Hori, S. and Brennen, C., "Dynamic Response to Global Oscillation of Propulsion Systems with Cavitating Pumps," *Journal Of Spacecraft And Rockets,* vol. 48(4), pp. 599-608, 2011.

[83] Smagorinsky, J., "General circulation experiments with the primitive equations," *Mon. Wea. Rev.,* vol. 91(3), pp. 99-164, 1963.

[84] Deardorff, J., "A numerical study of three-dimensional turbulent channel flow at large Reynolds numbers," *1970,* vol. 41(02), p. 453, J. Fluid Mech..

[85] Jones, W. and Launder, B., "The prediction of laminarization with a two-equation model of turbulence," *International Journal Of Heat And Mass Transfer,* vol. 15(2), pp. 301-314, 1972.

[86] Wilcox, D., C., Turbulence Modeling for CFD (Second Edition), California, USA: La Canada: DCW Industries, 1993.

[87] D. Liuzzi, "Two-Phase Cavitation Modelling: Fully Compressible Formulation," Ph. D Dissertation at the University of Rome, Faculty of Civil and Industrial Engineering, June 2012.

[88] A. Kubota, H. Kato and H. Yamaguchi, "A new modelling of cavitating flows: A numerical study of unsteady cavitation on a hydrofoil section," *Journal of Fluid Mechanics,* vol. 240, pp. 59-96, 1992.

[89] G. H. Schnerr and J. Sauer, "Physical and Numerical Modeling of Unsteady Cavitation Dynamics," in *Fourth International Conference on Multiphase Flow*, New Orleans, USA, 2001.

[90] P. J. Zwart, A. G. Gerber and T. Belamri, "A Two-Phase Flow Model for Predicting Cavitation Dynamics," in *Fifth International Conference on Multiphase Flow*, Yokohama, Japan, 2004.

[91] A. K. Singhal, H. Y. Li, M. M. Athavale and Y. Jiang, "Mathematical Basis and Validation of the Full Cavitation Model," in *ASME FEDSM'01*, New Orleans, Louisiana, 2001.

[92] Ji, B.,, Luo, X., Arndt, R. and Wu, Y., "Numerical simulation of three dimensional cavitation shedding dynamics with special emphasis on cavitation–vortex interaction," *Ocean Engineering,* vol. 87, pp. 64-77, 2014.

[93] Foeth, A.-J., *The structure of three-dimensional sheet cavitation,* PhD Thesis, Delft University of Technology, 2008.

[94] Hosangadi, A., Ahuja, V. and Ungewitter, R., "Simulations of Cavitating Flows in Turbopumps," *Journal Of Propulsion And Power,* vol. 20(4), pp. 604-611, 2004.

[95] Hosangadi, A., Ahuja, V. and Ungewitter, R., "Simulations of Rotational Cavitation Instabilities in the SSME LPFP Inducer," *43rd AIAA Joint Propulsion Conference, (July),* 2007.

[96] Hosangadi, A., Ahuja, V. and Ungewitter, R., "Simulation of Cavitation Instabilities in Inducers," *In Proceedings of the Seventh International Conference on Cavitation,* 2009.

[97] Peters, A., *Ultra-Short Nacelles for Low Fan Pressure Ratio Propulsors,* PhD Thesis, Massachusetts Institute of Technology, 2014.

[98] Sorensen, W. A., *A Body Force Model for Cavitation Inducer in Rocket Engine Turbopumps,* MSc Thesis, Massachusetts Institute of Technology, 2014.

[99] Lighthill, M. J., "On displacement thickness," *Journal of Fluid Mechanics,* vol. 4(4), pp. 383-392, 1958.

[100] Y. Iga and Y. Yoshida, "Mechanism of Propagation Direction of Rotating Cavitation in a Cascade," *Journal of Propulsion and Power,* vol. vol. 27, no. no. 3, pp. 675-683, May-June 2011.

[101] F. Marble, "Three-Dimensional Flow in Turbomachines," *volume X of High Speed Aerodynamics and Jet Propulsion, Hawthorne, W. R., ed. Princeton University Press, Princeton, NJ,* pp. 83-166, 1964.

[102] M. Drela, "Xfoil: An Analysis and Design System for Low Reynolds Number Airfoils," MIT Department of Aeronautics and Astronautics, [Online]. Available: http://web.mit.edu/drela/Public/papers/xfoil_sv.pdf. [Accessed 10 02 2017].

[103] W. S. Cunnan, W. Stevans and D. C. Urasek, "Design and Performance of a 427-Meter-Per_Second-Tip-Speed Two-Stage Fan Having a 2.40 Pressure Ratio," NASA Technical Paper 1314, October, 1978.

[104] A. Arnone, "Viscous Analysis of Three-Dimensional Rotor Flow Using a Multigrid Method," *Journal of Turbomachinery,* vol. vol. 116, pp. 435-445, July, 1994.

[105] V. J. Fidalgo, C. A. Hall and Y. Colin, "A Study of Fan-Distortion Interaction within the NASA-67 Transonic Stage," *Journal of Turbomachinery,* vol. vol 134, pp. 051011-1 - 051011-12, September, 2012.

[106] C. Hah and L. Reid, "A Viscous Flow Study of Shock-Boundary Layer Interaction, Radial Transport, and Wake Development in a Transonic Compressor," *Journal of Turbomachinery,* vol. vol 114, pp. 538-547, July, 1992.

[107] I. K. Jennions and M. G. Turner, "Three-Dimensional Navier-Stokes Computations of Transonic Fan Flow Using an Explicit Flow Solver and an Implicit a - e Solver," *Journal of Turbomachinery,* vol. vol 115, pp. 261-272, April, 1993.

[108] M. J. Pierzga and J. R. Wood, "Investigation of the Three-Dimensional Flow Field Within a Transonic Fan Rotor Experiment and Analysis," *Journal of Turbomachinery,* vol. vol 107, pp. 436-448, April 1985.

[109] M. Hoekstra, "The Myth of the Re-entrant Jet," in *WIMRC 3rd International Cavitation Forum*, UK, July 2011.

[110] M. Sakoda, R. Yakushiji, M. Maeda and H. Yamaguchi, "Mechanism of Cloud Cavitation Generation on a 2-D Hydrofoil," in *CAV 2001: Fourth International Symposium on Cavitation*, (Unpublished), June 20-23, 2001.

[111] Y. Kawanami, *Estimation of Cavitation Structure on a Hydrofoil and Impulsive Pressure of the Bubble Collapse,* Ph.D. Thesis, University of Tokyo, Tokyo, 1999 (in Japanese).

[112] J. Štigler and J. Svozil, "Modeling of Cavitation Flow on a NACA 0015 Hydrofoil," *Engineering Mechanics,* vol. vol. 16, no. no. 6, pp. 447-455, 2009.

[113] A. Cervone, C. Bramanti, E. Rapposelli and L. d'Agostino, "Thermal Cavitation Experiments on a NACA 0015 Hydrofoil," *Journal of Fluids Engineering,* vol. vol. 128, pp. 326-331, March, 2006.

[114] L. L. Coons, J. M. Reddecliff, A. E. Wemmell and W. E. Young, "Study of Inducer Load and Stress," Pratt & Whitney Aircraft, Florida Research and Development Center, NASA report CR 72712 Vol. 3, November, 1972.

2017